



National Library
of Canada

Acquisitions and
Bibliographic Services Branch

395 Wellington Street
Ottawa, Ontario
K1A 0N4

Bibliothèque nationale
du Canada

Direction des acquisitions et
des services bibliographiques

395, rue Wellington
Ottawa (Ontario)
K1A 0N4

Notice - Notice

Notice - Notice

NOTICE

The quality of this microform is heavily dependent upon the quality of the original thesis submitted for microfilming. Every effort has been made to ensure the highest quality of reproduction possible.

If pages are missing, contact the university which granted the degree.

Some pages may have indistinct print especially if the original pages were typed with a poor typewriter ribbon or if the university sent us an inferior photocopy.

Reproduction in full or in part of this microform is governed by the Canadian Copyright Act, R.S.C. 1970, c. C-30, and subsequent amendments.

AVIS

La qualité de cette microforme dépend grandement de la qualité de la thèse soumise au microfilmage. Nous avons tout fait pour assurer une qualité supérieure de reproduction.

S'il manque des pages, veuillez communiquer avec l'université qui a conféré le grade.

La qualité d'impression de certaines pages peut laisser à désirer, surtout si les pages originales ont été dactylographiées à l'aide d'un ruban usé ou si l'université nous a fait parvenir une photocopie de qualité inférieure.

La reproduction, même partielle, de cette microforme est soumise à la Loi canadienne sur le droit d'auteur, SRC 1970, c. C-30, et ses amendements subséquents.

Canada

**AN EXPERIMENTAL INVESTIGATION AND DIMENSIONAL
ANALYSIS OF CONFINED VORTEX FLOWS**

Hing Chum Lam

**A Thesis
in
The Department
of
Mechanical Engineering**

**Presented in Partial Fulfilment of the Requirements
for the degree of Doctor of Philosophy at
Concordia University
Montréal, Québec, Canada**

1993

© Hing Chum Lam, 1993



National Library
of Canada

Acquisitions and
Bibliographic Services Branch

395 Wellington Street
Ottawa, Ontario
K1A 0N4

Bibliothèque nationale
du Canada

Direction des acquisitions et
des services bibliographiques

395, rue Wellington
Ottawa (Ontario)
K1A 0N4

Your file / Votre référence

Our file / Notre référence

The author has granted an irrevocable non-exclusive licence allowing the National Library of Canada to reproduce, loan, distribute or sell copies of his/her thesis by any means and in any form or format, making this thesis available to interested persons.

L'auteur a accordé une licence irrévocable et non exclusive permettant à la Bibliothèque nationale du Canada de reproduire, prêter, distribuer ou vendre des copies de sa thèse de quelque manière et sous quelque forme que ce soit pour mettre des exemplaires de cette thèse à la disposition des personnes intéressées.

The author retains ownership of the copyright in his/her thesis. Neither the thesis nor substantial extracts from it may be printed or otherwise reproduced without his/her permission.

L'auteur conserve la propriété du droit d'auteur qui protège sa thèse. Ni la thèse ni des extraits substantiels de celle-ci ne doivent être imprimés ou autrement reproduits sans son autorisation.

ISBN 0-315-87271-3

Canada

**AN EXPERIMENTAL INVESTIGATION AND DIMENSIONAL
ANALYSIS OF CONFINED VORTEX FLOWS**

Hing Chum Lam

**A Thesis
in
The Department
of
Mechanical Engineering**

**Presented in Partial Fulfilment of the Requirements
for the degree of Doctor of Philosophy at
Concordia University
Montréal, Québec, Canada**

1993

© Hing Chum Lam, 1993

ABSTRACT

Hing Chum Lam, Ph.D. **An Experimental Investigation and Dimensional
Analysis Of Confined Vortex Flows**
Concordia University, 1993

Experimental and theoretical studies on the velocity and static pressure distributions, and pressure drop across vortex chambers are presented herein. The experimental studies include mapping of the flow parameters such as the three velocity components and the static pressure as a function of the axial location and the radius using a 5-hole pitot-probe. In addition, the pressure drop across the chamber for a variety of inlet and outlet conditions was obtained. Flow visualizations using a hydraulic vortex chamber to infer the behavior of the vortex core are also included. For the cases where vortex breakdown has taken place and a wake like core has been formed, visualization experiments have shown that the average core radius is almost invariant in the axial direction. This is also confirmed by radial distributions of the tangential velocity in different axial stations, obtained using the pitot-probe. A numerical method to filter the centrifugal effects of the pressure on the velocities has been developed. The inadequacy for any experimental method in defining the true value of the maximum tangential velocity is attributed to the presence of inertial waves in the vortex cores. Dimensional analysis provides the functional relationships among the main dimensionless groups. Energy balance and continuity over the control volume along with the minimum pressure drop principle furnish the formulae that relate the dominant non-dimensional parameters. For strongly swirling flows, the derived relationships for the tangential velocity and the pressure distribution are shown to correlate well with the present

problem. It has also been found that the obtained similarity relationships represent well for most concentrated vortices regardless of the method of their production. Hence, the main characteristics in vortices such as the trailing vortex, the tornado, the vortex produced in a cup by stirring the liquid, etc., are shown to be well characterized by the same functional relationships. Furthermore, with respect to the main vortex chamber parameters, the present study harmonizes the present with the previous experimental studies. The vortex core has been found to be located at approximately the mid static pressure value of its radial distribution. The internal flowfield alterations in caused by the incorporation of a conical plug at the exit of the chamber to decrease the pressure drop across the system has been experimentally investigated. The present study provides the vortex chamber designer a relatively simple method to calculate the magnitudes of the main flow parameters with a good accuracy.

ACKNOWLEDGMENTS

I am indebted to numerous advisers, associates and others, whose names are listed in this acknowledgments that follow the text. My special gratitude to Dr. G.H. Vatistas and Dr. S. Lin for their important advice and guidance. I cannot sufficiently express my obligation and thankfulness to Dr. C.K. Kwok for his financial support throughout the years.

All the technicians, lead by Mr. J. Elliott (Laboratory Coordinator), are greatly appreciated for their helpful assistance. Also, I relied on my wife, Anna, our child, Derek Wayne and my parents more than they realize. Their comments, patience and encouragement are deeply appreciated.

Also, the effort from J. Hulet and P. Lawn to proof read my thesis deserved a special mention. Lastly but not the least, I would like to thank Pratt and Whitney Canada Inc. for the lending of the Macintosh computer. Without this generosity, my thesis would not have been finished in this kind of pace.

TABLE OF CONTENTS

LIST OF FIGURES	ix
LIST OF PHOTOS	xii
LIST OF TABLES	xiii
NOMENCLATURE.	xiv

CHAPTER 1 INTRODUCTION1

1.1 General Introduction of Vortex Flows.	1
1.2 Applications of Confined Vortices.	5
1.3 The Problem of Confined Vortex Flows.	10
1.4 Previous Work on Confined Vortex Flow.	15
1.5 Outline of the Present Thesis.	16

CHAPTER 2 EXPERIMENTAL APPARATUS, PROCEDURE AND DATA DEDUCTION. 19

2.1 Experimental Facility.	19
2.2 Apparatus and Instrumentation of Confined Vortex Flow.	21
2.2.1 Apparatus.	21
2.2.2 Instrumentation.	22
2.3 Experimental Procedure.	23
2.4 Data Deduction.	27
2.5 Reliability of the Results due to Oscillation of the Vortex Core	34

CHAPTER 3	DIMENSIONAL ANALYSIS OF CONFINED	
	VORTEX FLOWS.	38
3.1	Dimensional Analysis on the Core Radius.	39
3.2	Dimensional Analysis on Velocities and Pressure.	42
3.3	Verification of the Analysis.	49
CHAPTER 4	CORE SIZE AND STATIC PRESSURE DROP.	67
4.1	Governing Equations for Pressure Drop and Core Size	67
4.2	The Least Squares Method for the Experimental Data	79
CHAPTER 5	EXPERIMENTAL RESULTS OF CONFINED	
	VORTEX FLOWS.	84
5.1	Results of the Visualization Experiment.	85
5.2	Velocity Profile And Static Pressure Profile	
	Inside the Vortex Chamber.	90
5.3	The Comparison Between the Measured and Corrected	
	Experimental Data.	108
5.4	The Reduction of Pressure Drop by	
	the Conical Plug Mechanism.	111
CHAPTER 6	CONCLUSION.	121
REFERENCES	124

APPENDIX I	FORTTRAN SOURCE CODE FOR THE DEDUCTION OF THE EXPERIMENTAL DATA.	136
------------	---	-----

APPENDIX II	CALIBRATION DATA FOR THE FIVE HOLE PITOT PROBE.	148
-------------	--	-----

LIST OF FIGURES

Figure:

- 1.1.1 Tangential Inlets to Generate a Confined Vortex. (Pg.3)
- 1.1.2a Radial Vanes to Generate a Confined Vortex. (Pg.4)
- 1.1.2b Axial Vanes to Generate a Confined Vortex. (Pg.4)
- 1.2.1 Sectional Views of a Rocket Propulsion Nozzle. (Pg.6)
- 1.2.2 Sectional Views of a Vortex Valve. (Pg.6)
- 1.2.3 A Vortex Combustor (Pg.7)
- 1.2.4 A Vortex Separator (Pg.7)
- 1.2.5 A Ranque-Hilsh Tube (Pg.8)
- 1.2.6 Sectional View of a Swirl Atomizer (Pg.8)
- 1.3.1 A Typical Flow Pattern of Confined Vortex Flow (Pg.12)
- 1.3.2 Vortex Core Flow Regimes (Pg.14)
- 2.1.1 A Schematic of the Experimental Facility (Pg.20)
- 2.2.1 The Vortex Generator Assembly and the Vortex Chamber (Pg.24)
- 2.2.2 The Five Hole Pitot Probe (Pg.25)
- 2.2.3 The 3-d Coordinate System with the Velocity Components (Pg.26)
- 2.4.1 Errors which Introduced to the Probe by the Radial Static Pressure Field (Pg.30)
- 2.5.1 Three Tangential Velocity Profile to Illustrate the Concept of Maximum (Pg.36)
- 2.5.2 Measured Maximum Tangential Velocity Component vs. Time (Pg.37)
- 3.3.1 Nondimensional Core Radius X_{CD} vs. β (Pg.50)
- 3.3.2 Nondimensional Exit Core Radius X_{CF} vs. β^2 (Pg.53)

- 3.3.3 $V_{\theta\max}/V_{\theta\text{in}}$ vs ξ (Pg.58)
- 3.3.4 Nondimensional Radial Pressure $\overline{\Delta P}$ vs \tilde{r} (Pg.63)
- 3.3.5 $\tilde{\Delta P}$ vs β (Pg.64)
- 3.3.6 \tilde{V}_θ vs \tilde{r} for Concentrated Vortices (Pg.65)
- 3.3.7 \tilde{V}_r vs \tilde{r} for Concentrated Vortices (Pg.66)
- 4.1.1 Schematic of the Physical Problem (Pg.69)
- 4.1.2 Nondimensional Core Size X_{CF} at the Exit vs β (Pg.72)
- 4.1.3 Variation of the Normalized Pressure vs Cr with Different Area Ratios (Pg.75)
- 4.1.4 The Normalized Pressure Difference as a Function of the Cr (Pg.77)
- 4.1.5 Nondimensional Pressure Difference as a Function of the Exit Core (Pg.78)
- 4.2.1 Nondimensional Pressure Difference vs β (Pg.80)
- 5.2.1 Measured Tangential Velocity, V_θ , for Three Different Cr (Pg.92)
- 5.2.2 Measured Tangential Velocity, V_θ , for Two Different Flow Rates (Pg.93)
- 5.2.3 Measured Tangential Velocity, V_θ , for Six Different Axial Locations (Pg.94)
- 5.2.4 Measured Axial Velocity, V_z , for Three Different Cr (Pg.96)
- 5.2.5 Measured Axial Velocity, V_z , for Two Different Flow Rates (Pg.97)
- 5.2.6 Measured Axial Velocity, V_z , for Six Different Axial Locations (Pg.98)
- 5.2.7 Measured Radial Velocity, V_r , for Three Different Cr (Pg.100)
- 5.2.8 Measured Radial Velocity, V_r , for Two Different Flow Rates (Pg.101)

- 5.2.9 Measured Radial Velocity, V_r , for Six Different Axial Locations (Pg.102)
- 5.2.10 Measured Radial Pressure for Three Different Cr (Pg.105)
- 5.2.11 Measured Radial Pressure for Two Different Flow Rates (Pg.106)
- 5.2.12 Measured Radial Pressure for Six Different Axial Locations (Pg.107)
- 5.3.1 The Comparison between two sets of Radial Velocity Data (Pg.109)
- 5.3.2 The Comparison between two sets of Radial Pressure Data (Pg.110)
- 5.4.1 The Physical Dimensions of the Conical Plug (Pg.114)
- 5.4.2 The Pressure Drop across the Chamber ($2\Delta P/\rho q_{in}^2$) vs. the Position of the Plug (z/H) at $Cr=0.5$ (Pg.115)
- 5.4.3 The Pressure Drop across the Chamber ($2\Delta P/\rho q_{in}^2$) vs. the Position of the Plug (z/H) $Cr=0.3$ (Pg.116)
- 5.4.4 The Comparison between the Tangential Velocity with and without Plug (Pg.117)
- 5.4.5 The Comparison between the Axial Velocity with and without Plug (Pg.118)
- 5.4.6 The Comparison between the Radial Pressure with and without Plug. (Pg.119)
- 5.4.7 The Comparison between the Radial Velocity with and without Plug (Pg.120)

LIST OF PHOTOS

Photo:

- 5.1.1 An Overall View of the Visualization Experimental Set-up (Pg.86)
- 5.1.2 Another View of the Visualization Experimental Set-up (Pg.86)
- 5.1.3 The Development of the Core Inside the Vortex for Low Flow Rate ($Re \sim 4.5 \times 10^4$) (Pg.87)
- 5.1.4 Vortex Breakdown in the Downstream for the Low Flow Rate ($Re \sim 4.5 \times 10^4$) (Pg.87)
- 5.1.5 The Development of the Core Inside the Vortex for a High Flow Rate. ($Re \sim 1.5 \times 10^5$) (Pg.88)
- 5.1.6 The Development of a Reverse Flow Downstream for a Higher Flow Rate ($Re \sim 3.0 \times 10^5$) (Pg.88)
- 5.1.7 Intense Oscillation along the Core for a Low Flow Rate ($Re \sim 4.5 \times 10^4$) (Pg.89)
- 5.1.8 Another View of the Core Oscillation (Pg.89)

LIST OF TABLES

- 3.3.1 Values of $\overline{\Delta P}$ as a function of radii \tilde{r} (Pg.60)
- 4.1.1 Core Size Equations (Pg.73)
- 4.1.2 Pressure Drop Equation (Pg.73)
- 4.2.1 Values of the Coefficients in Eqn. (4.2.4) (Pg.73)
- 4.2.2 Values of the Coefficients in Eqn. (4.2.5) (Pg.73)
- 5.2.1 Normalized Core Size for Respective Contraction Ratio (Pg.91)

NOMENCLATURE

A_{in}	inlet area for incoming fluid into the vortex chamber
A_O	cross section area of the vortex chamber
A_E	exit area (πR_E^2)
A_i, B_i, C_i, D_i	coefficients of a third degree polynomial
a	parameter in the tangential velocity equation for Burger's vortex
C_P	pressure coefficient ($2 (P_{wall} - P(\bar{r})/\rho q_{in}^2)$)
C_{P4}	C_P value of point 4 at the pitot probe
C_{P5}	C_P value of point 5 at the pitot probe
Cr	contraction ratio (R_E/R_O)
$f(X)$	a function of X
P_1, P_2, P_3, P_4, P_5	pressure measurement for the respective five hole of the pitot probe
P_{amb}	ambient pressure
ΔP	$P_{in} - P_{amb}$
$\Delta P'$	$2(P(r) - P_{amb})/\rho q_{in}^2$ (q_{in} @ 70 SCFM)
$\Delta P_{0.45}$	ΔP value at $Cr = 0.45$
P_t	total pressure
P_s	static pressure
P_{in}	inlet static pressure
P_{wall}	static pressure near the wall
$\overline{\Delta P}(\bar{r})$	$\frac{2(P(\bar{r}) - P_{wall})}{\rho q_{in}^2} \left[\frac{\xi}{\cos\varphi} \right]^2$

$\tilde{\Delta P}$	$\left[\frac{2(P_{in} - P_{amb})}{\rho q_{in}^2} + 1 \right] \left[\frac{R_E/R_O}{\cos\phi} \right]^2$
Q	Volumetric flow rate ($q_{in}A_{in}$)
q_{in}	average inlet velocity of the fluid entering the vortex chamber
R_O	radius of the vortex chamber
R_E	exit radius
R_{CD}	core radius inside the vortex chamber
R_{CF}	core radius at the exit
Re	Reynolds number ($Q/(R_O\nu)$)
\bar{r}	nondimensional radial coordinate (r/R_O)
δr	$(\bar{r}_i - 0.02) - \bar{r}_{i-1}$
\bar{r}	r/R_{CD}
r, θ, z	cylindrical coordinate system (radial, tangential, axial)
\vec{V}	total velocity vector
V_r	velocity component in the r direction
V_θ	velocity component in the θ direction
V_z	velocity component in the z direction
\tilde{V}_θ	$(V_\theta/V_{\theta in}) \xi$
$V_{\theta in}$	tangential velocity at the inlet ($q_{in}\cos\phi$)
$V_{\theta max}$	maximum tangential velocity
V_E	average axial velocity at the exit
X_{CD}	nondimensional core radius inside the vortex chamber (R_{CD}/R_E)
X_{CF}	nondimensional core radius at the exit (R_{CF}/R_E)
X	independent variable of a polynomial
X_i, X_{i+1}	two end X values of a section of a cubic spline polynomial
Y	dependent variable of a polynomial

\bar{z} nondimensional z coordinate (z/R_O)

Greek Symbols:

α yaw angle

ρ fluid density

ϕ pitch angle

Γ inlet vortex strength ($2\pi R_O q_{in} \cos\phi$ or $2\pi R_O V_{\theta in}$)

φ inlet flow angle measured from the tangent to the inlet velocity

β vortex geometric parameter $\left(\frac{A_{in}/A_O}{(R_E/R_O) \cos\phi} \right)$

ν kinematic viscosity of the fluid

ξ R_{CD}/R_O

CHAPTER 1

INTRODUCTION

1.1 GENERAL INTRODUCTION OF VORTEX FLOWS

Vortex flows can be categorized into confined and unconfined types. Unconfined vortices are those generated in a large fluid body. Geophysical vortices such as wind whirl, dust devils, fire whirls, tornadoes and Atlantic currents [1] as well as the mechanically produced aerodynamic vortices such as trailing vortices [2-4], and the tornado-like flow upstream of the intake of a gas turbine engine [5], all belong to this category.

A confined vortex is usually generated inside a cylindrical vortex chamber with a centrally located outlet placed at the downstream section of the flow. Fluid entering the chamber acquires swirl by:

- a) inlets which are arranged tangentially around the circumferential wall. (Figure 1.1.1)
- b) admission through radial or axial vanes. (Figure 1.1.2a and Figure 1.1.2b)

The inlets are often placed at the upstream or downstream sections or along the entire length of the chamber. Although experimental results obtained using any of the above mentioned methods to produce the vortex will be considered, the present thesis will focus primarily on the jet driven vortex chamber, i.e. case (b). Also, the developed confined vortex is considered as concentrated vortex. The special characteristic of concentrated vortices is that

their vorticity is concentrated in small tubular region near the center, decaying rapidly outward in the radial direction.

The behavior of concentrated vortices confined in cylindrical tubes, and their interaction with the host flowfield is important for mainly three reasons.

First, swirl can be found in many engineering applications. For instance, in vortex separators, cyclone combustors, vortex pumps, swirl atomizers, vortex valves, Ranque-Hilsh tubes, vortex whistles etc., the presence of a vortex is essential for the adequate operation of the equipment. In contrast, vortices generated in the intakes of liquid pumps [6], draft tubes of water turbines [7-9], weirs [10,11], draining of reservoirs [6,12] etc, swirl is an undesirable by-product of the fluid motion which severely interferes with the main function of the equipment, and thereby the designer strives to suppress it.

Second, important phenomena such as vortex breakdown in highly sweptback wings [13-16] and the main characteristics of high Rossby Number geophysical vortices (dust-devils, tornadoes, waterspouts) [17-20] can be reproduced in tubes and then analyzed under controlled laboratory conditions. The Rossby number is the ratio of relative inertial to Coriolis forces in a fluid body undergoing rotation as a whole; or equivalently, the ratio of relative velocity in a plane normal to the appropriate axis of rotation to a typical transverse or tangential velocity of background rotation in this plane. The Rossby number provides a measure of the constraint on an interior flow due to the rotation of its whole environment; thus a balanced

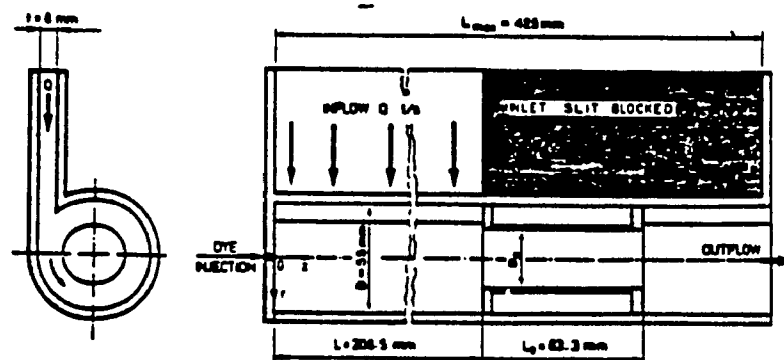


Figure 1.1.1 Tangential Inlets (Method (a)) to
Generate a confined Vortex. [24]

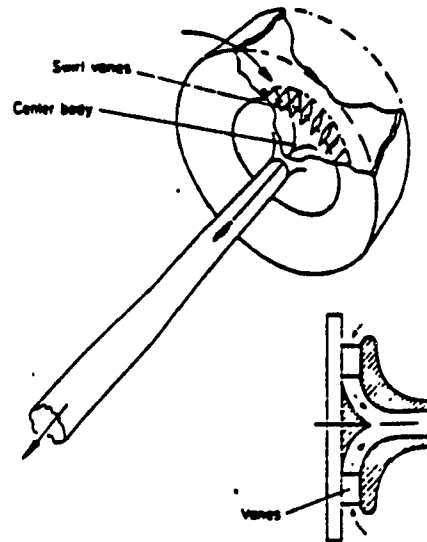


Figure 1.1.2a Radial Vanes (Method (b)) to Generate a Confined Vortex. [27]

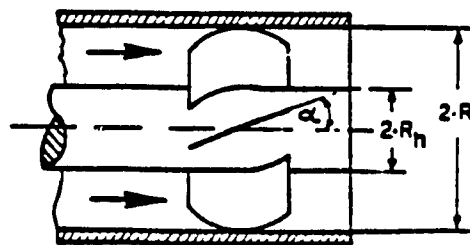


Figure 1.1.2b Axial Vanes (Method (b)) to Generate a Confined Vortex

geostrophic flow with velocity normal to the pressure gradient is a typical small Rossby number flow, and these flows have a general tendency to be two-dimensional. [1]

Third, this area is also of interest to ion flow dynamics, meteorology, biology, geophysics, low temperature physics, nuclear space propulsion and to several other classifications of scientific knowledge [21-23].

1.2 APPLICATIONS OF CONFINED VORTICES

There are many practical applications which utilize the beneficial effects of confined vortices. The following are some typical examples:

(1) Nuclear Rocket Propulsion (Figure 1.2.1)

Some researchers have proposed [33] the use of vortex flow in order to suspend an annulus of gaseous nuclear fuel inside a cylindrical chamber of a conceived rocket engine [34-41]. Due to flow characteristics of confined vortex flow, a higher combustion efficiency could be achieved and hence this may produce a stronger propulsion power for the rocket.

(2) Vortex Valve (Figure 1.2.2)

Many fluid devices utilize the vortex flow phenomenon to control the flow without using a mechanical component. The most common known device is the vortex valve component [42]. This device takes advantage of the negative gage pressure developed inside the vortex core to pump liquid [43,44].

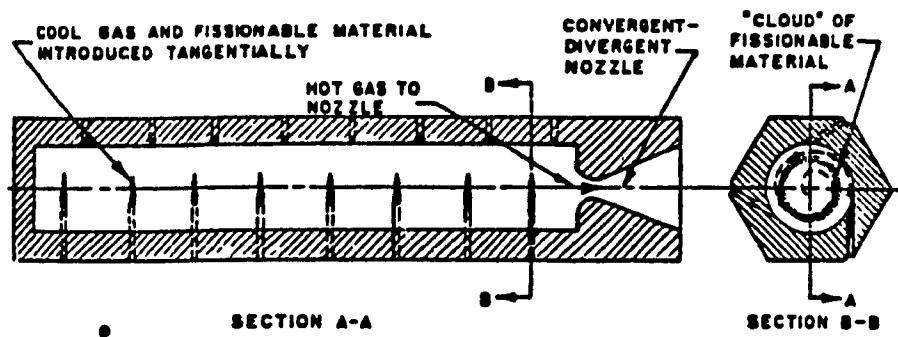


Figure 1.2.1 Sectional Views of a Rocket Propulsion
Nozzle [33]

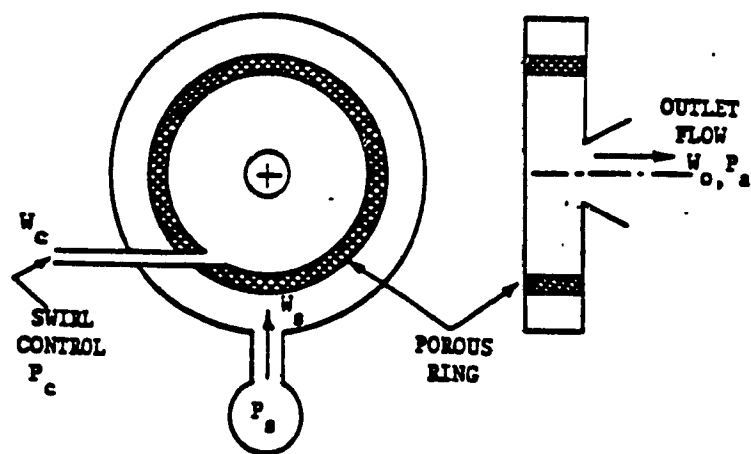


Figure 1.2.2 Sectional Views of a Vortex Valve [111]

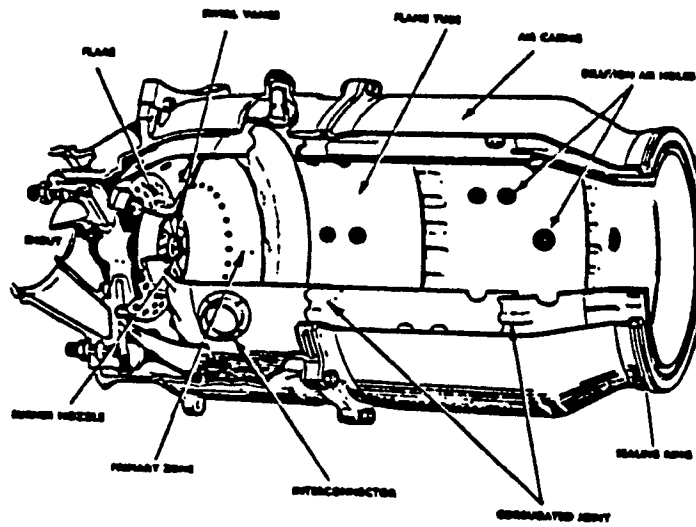


Figure 1.2.3 A Vortex Combustor [61]

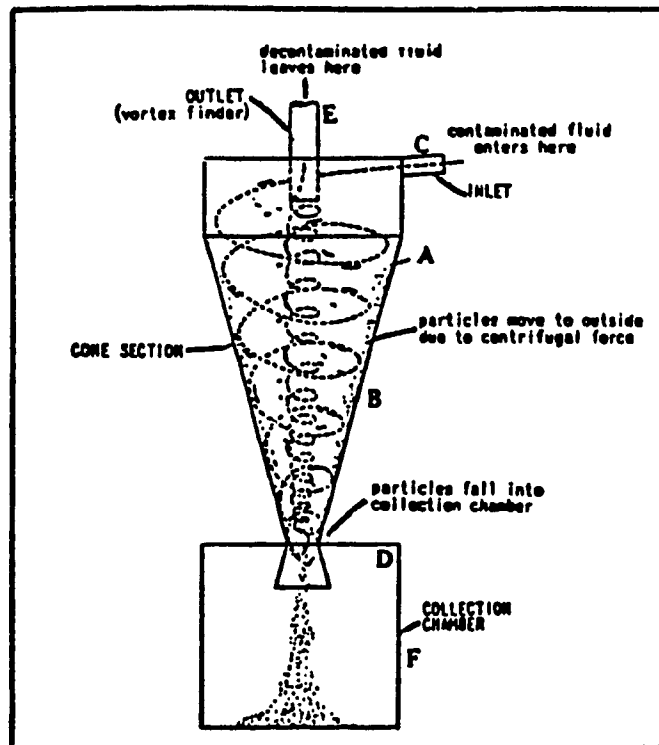


Figure 1.2.4 A Vortex Separator

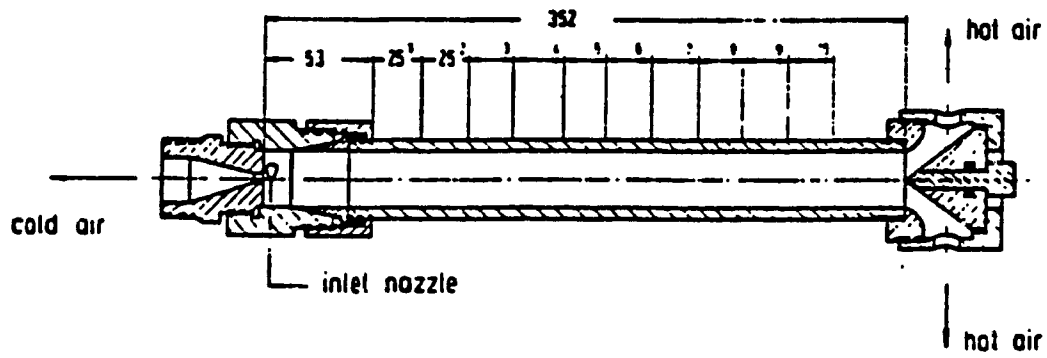


Figure 1.2.5 A Ranque-Hilsh Tube

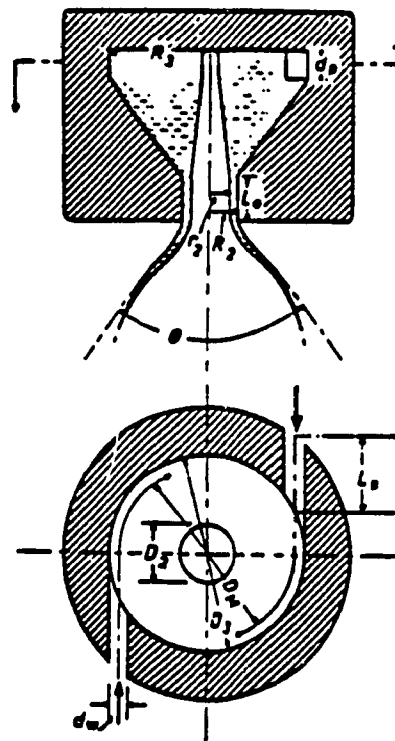


Figure 1.2.6 Sectional View of a Swirl Atomizer

(3) Vortex Combustor (Figure 1.2.3)

By using the vortex breakdown phenomenon, one can create a recirculation zone inside a combustion chamber which can stabilize the flame [45-47]. High swirl flows are frequently used in turbine combustors to prevent flow separation and enhance combustion stability by improving flow stability. Flow recirculation has been observed in high swirl flows in the absence of large area change or downstream fluid injection, a phenomenon known as vortex breakdown. In industrial furnaces [48-60], swirl keeps the solid fuel in suspension, increases the residence time and enables even the most difficult (low calorific value) fuel to be burned [59,60].

(4) Gas and Hydraulic Vortex Separator (Figure 1.2.4)

It is a device which is used for the removal of solid particulates from gases. This equipment is widely used to filter gasses in the chemical engineering industry. It can also be used to separate a solute from a solvent, a typical example is to produce cream from milk where water is the solvent [61-73].

(5) Ranque-Hilsh Tube (Figure 1.2.5)

The swirling action of a compressible gas is used for energy separation [74-87]. Ranque [75] first reported the phenomenon and Hilsh [76] first published the systematic experimental results. It has been used to cool drinking water in a locomotive [83], as a cooling system for electronic components [88] in supersonic aircraft and for liquefaction of natural gas.

(6) Vortex Whistle

The vortex whistle, in contrast to the "edge tone" contemporary kind whose frequency varies little with the applied pressure, produces notes having frequencies which vary continuously with the applied air pressure [89-91].

(7) Flood Protection Vortex Valves

Vortex valves have been used in fluidics [92-100] and the so called flood retention reservoir utilizes the operating principle of vortex valves which retain and store the extra water temporarily through swirling motion after a severe rain storm [101].

(8) Swirl Atomizers (Figure 1.2.6)

In this device, the vortex is utilized to atomize the fluid particle under control conditions. The swirl atomizer can transform the bulk liquid fuel into a thin conical liquid shell which in turn breaks into fine droplets. This way, the problems of overheating and/or shoot formation or carbon deposit build up are avoided [102-104].

1.3 THE PROBLEM OF CONFINED VORTEX FLOWS

Research over the years on vortex chamber flow has produced many controversies. However, there are many different aspects of confined vortex or which most of the investigators agree on. The most significant are [31,32]:

- (a) The tangential velocity component is dominant and the radial velocity component is relatively small.

- (b) Axial flow occurs in the annular region adjacent to the wall. Some researchers found a substantial axial flow in the maximum tangential velocity region.
- (c) The axial velocity may show a reversal near the axis of the vortex chamber.
- (d) The tangential velocity component profile is composed of two regions: a peripheral region of quasi-free vortex and a central region of quasi-forced vortex flow.
- (e) The static pressure is relatively high near the circumferential wall and decreases drastically near the axis, where it reaches its minimum.

A typical flow pattern of confined vortex flow in the r - θ plane is given in Figure 1.3.1. As the fluid enters the vortex chamber it immediately experiences a strong centrifugal force. In its attempt to find the exit with a minimum effort, it divides itself into two streams. Within the first one, label D in the figure, the fluid particles propagate along the circumferential wall where the centrifugal force is constant. They then flow downstream at a point near the exit plate and then travel into the exhaust manifold. Within the second one, label E in the figure, the fluid particles flow towards the center through the Ekman's boundary layer. They then flow to the downstream exit plate and their path is near the core where a pressure deficit exists.

In a small aspect ratio (length/diameter) vortex chamber, the entire flowfield is dominated by the end plate Ekman's boundary layer. Experiments performed by Kendall [120] have shown that the end wall boundary layer is still dominated the flowfield in larger aspect ratio vortex

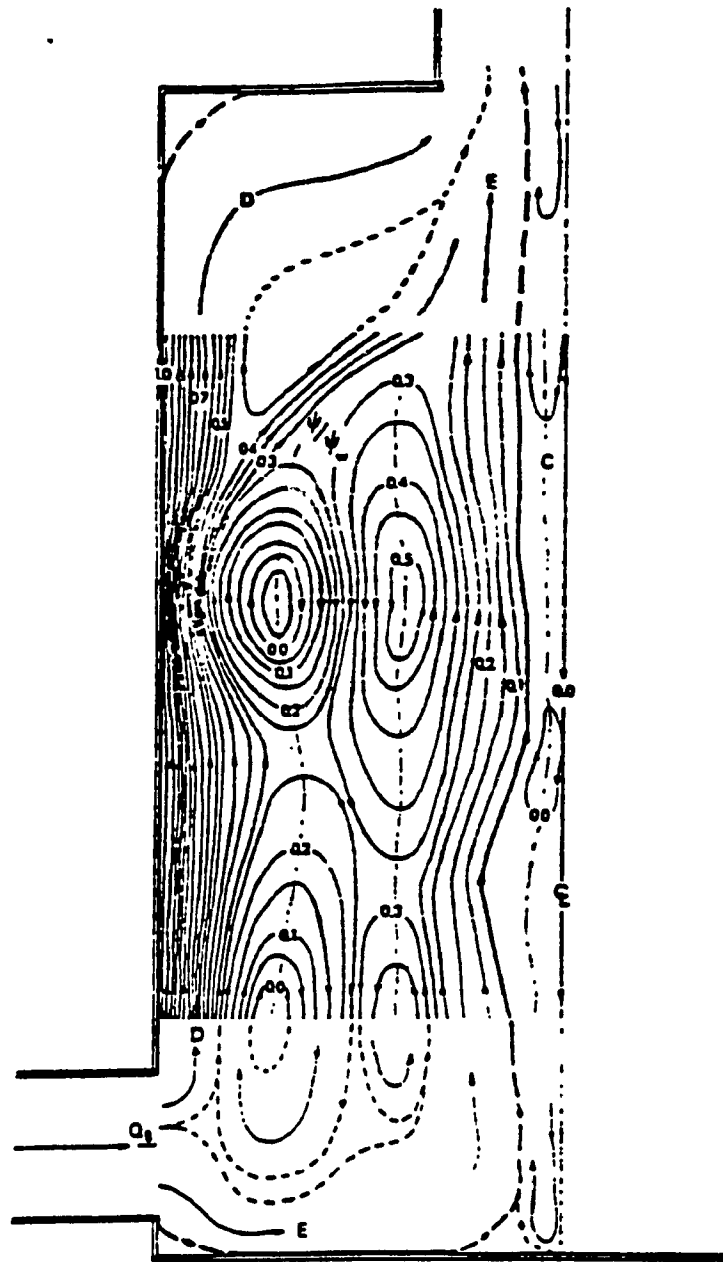


Figure 1.3.1 A Typical Flow Pattern of Confined Vortex Flow (Ref.118)

chambers. The tangential velocity peaks inside the boundary layer have been attributed to the relatively large radial velocity which assists the fluid particles to conserve their circulation better. This phenomenon is also present in the numerical results by Vatistas et al [107].

Many believe that a large recirculation zone exists between the cylindrical wall and the core. In Figure 1.3.1, it showed that a recirculation zone exists inside the chamber. Escudier attributes its origin to the unstable nature of the rotating flow which gives rise to Taylor-Goertier vortices. However, it can be shown that the Rayleigh's discriminant ($\Phi = dV_{\theta}r/dr$) becomes negative only near the circumferential wall where the V_{θ} drops monotonically to zero. Inside the core, the axial velocity will develop either a jet or a wake like profile. If one fixes the geometric parameter β and increases the Reynolds number ($Re = Q/(R_0 v)$), the axial velocity in the core may change from a jet-like or jet-like with a velocity deficit near the axis of the vortex to a wake-like (Figure 1.3.2). Figure 1.3.2 illustrates the different vortex flow regimes according to different combinations of Reynolds number and the geometric parameter β . Usually a jet-like core has a positive axial velocity profile. On the other hand, the wake-like core has a negative axial velocity profile. A similar transformation will take place if β is decreased while the Reynolds number is kept constant. The later flow state is characterized by the development of a strong entrained flow. Prevention of the reverse flow can be achieved with the incorporation of a conical plug at the downstream exit. This mechanism will also result in a considerable reduction of the pressure drop across the vortex chamber.

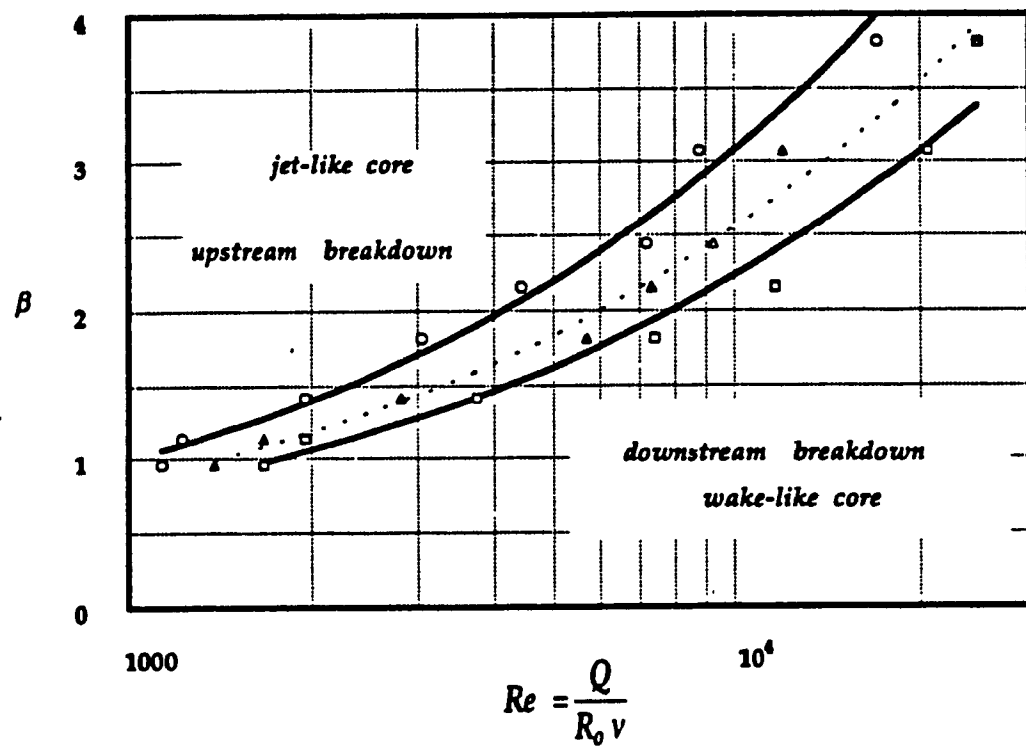


Figure 1.3.2 Vortex Core Flow Regimes
(Adapted from Escudier et al [30])

1.4 PREVIOUS WORK ON CONFINED VORTEX FLOW

In spite of the importance of the phenomenon in fundamental research and applications, our present understanding of concentrated vortices is confined to a large extent on either qualitative descriptions of the processes involved, or quantitative results for the flowfield applicable only to a particular geometry of the chamber or a specific set of operating conditions. The complexities presented by the governing equations and the boundary conditions have prevented analytical, or even numerical solutions capable to describe the physical process in every respect. Hence, most of the theoretical research has dealt with either particular solutions of the equations of motion, or numerical solutions with very approximate boundary conditions. The experimental work has been mainly focused on some specific applications, or the study of a particular phenomenon. The results are therefore restricted to the geometry and flow conditions of the individual study.

The main obstacle in the quantitative comparison between experimental studies lie mainly on the absence of clear rules with which flow similarity between chambers can be attained. These studies can be divided into two categories, those directed on the overall flow behavior, and the others to the internal flow structure.

In the first category, the pressure drop across the vortex chamber and the flow rate have been the subject of several researchers. The experimental studies on the internal flow structure include visualization, intrusive (direct and indirect) measurements as well as non-intrusive laser doppler anemometer measurements [24]. Visualizations were mainly directed to

secondary flow characterization. In many studies, water was used as the fluid medium with heavier-than-water dyes as tracers. Others used air with smoke, tufts or neutrally buoyant soap bubbles. Recently, the light slicing technique in water with a fluorescent dye was employed by Escudier et al [30]. Direct methods have been used to determine the flow properties by placing an object either inside the flowfield, i.e. pitot-probes and hot wires, or adjacent to it such as shear elements in a solid surface to measure the shear stress. Indirect procedures involved measurements of static pressure on one of the end walls followed by deduction of the other flow properties making simplifying assumptions about the flow field.

1.5 OUTLINE OF THE PRESENT THESIS

This thesis reports experimental and theoretical studies on the confined vortex flow problem. A total of six chapters have been written on this research subject.

Chapter 1 introduces the confined vortex flow phenomenon and the applications of concentrated vortices. It also describes some facts and problems which are associated with confined vortex flows.

Chapter 2 provides an overall picture on the experimental facility for this confined vortex flow project. The most important pieces of apparatus and instrumentation will be mentioned. The experimental procedure is given in a sequential order. The methodology of experimental data deduction will be explained. A numerical scheme to filter the centrifugal effects of the pressure on the velocities has been developed. The inadequacy

for any experimental method in defining the true value of the maximum tangential velocity due to the presence of inertial waves in the vortex cores will be discussed.

Chapter 3 presents the dimensional analysis on confined vortex flows. The analysis provides the functional relationships among the main dimensional groups. For strongly swirling flows, the derived relationships for the tangential velocity and the pressure distribution are shown to correlate well with the present problem. It has also been found that the obtained similarity relationships are representative of most concentrated vortices regardless of the method of their production. Furthermore, with respect to the main vortex chamber parameters, the present study harmonizes the present and the previous experimental studies. The vortex core has been found to be located at approximately the mid static pressure value of its radial distribution.

Chapter 4 focuses on the core size and pressure drop across the chamber. Energy balance and continuity over the control volume along with the minimum pressure drop principle furnish the formulas that relate the dominant non-dimensional parameters. The non-dimensional pressure drop has been found to depend solely on a single dimensionless parameters which involves only geometric quantities. This finding is supported by past and present experimental evidence. Based on the derived relationship and experimental data, an empirical formula capable of predicting the pressure drop over a wide range of design conditions has been obtained using the least squares method.

Chapter 5 summarizes the experimental results of confined vortex flows. The experimental studies include mapping of the flow parameters such as the three velocity components and the static pressure as a function of the axial location and the radius using a 5-hole pitot-probe. Flow visualizations using a hydraulic vortex chamber to infer the behavior of the vortex core are also included. For the cases where vortex breakdown has taken place and a wake like core has been formed, the visualization experiments have shown that the average core radius is almost invariant in the axial direction. This is also confirmed by the radial distributions of the tangential velocity in different axial stations, obtained by using the pitot-probe. The comparison of the measured and corrected experimental data are also discussed. The internal flowfield alterations caused by the incorporation of a conical plug at the exit of the chamber to decrease the pressure drop across the system has been experimentally examined.

Chapter 6 summarizes the results from this confined vortex flow project.

CHAPTER 2

EXPERIMENTAL APPARATUS, PROCEDURE AND DATA DEDUCTION

2.1 EXPERIMENTAL FACILITY

The current experiments were carried out in Concordia University at the Fluid Mechanics Research Laboratory. The vortex chamber research facility is schematically shown in Figure 2.1.1. Air passes through a rotameter from a main air supply source. As the air goes through a swirler, a vortex will be generated inside a vortex chamber. There are eight pressure taps located at the sides of the swirler for measuring the inlet static pressure of the vortex. The velocity and static pressure of the flowfield are deduced from the pressure data obtained from a five hole pitot probe. Two inclined manometers are used to measure all the experimental pressure data recorded by the probe.

Three types of experiments have been conducted, the first one deals with the effect on the vortex structure by changing the geometric parameters of the chamber. The second is an addition of a conical plug at the exit to reduce the pressure drop of the vortex chamber. The last experiment is a hydraulic visualization demonstration which shows the structure of a confined vortex qualitatively. The set-up of the visualization experiment is similar to the first two except the water is discharged to a large tank located at the exit of the vortex chamber.

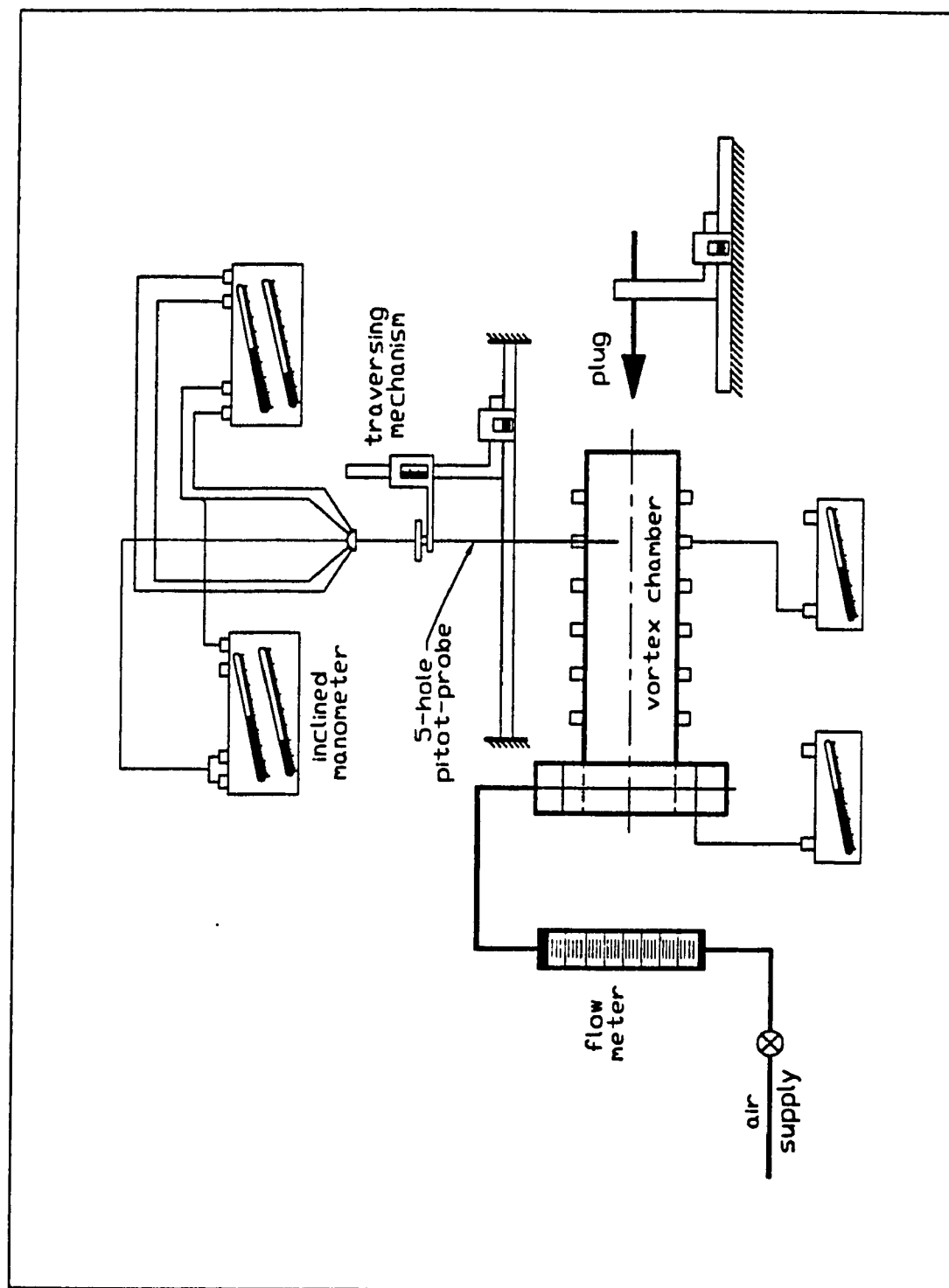


Figure 2.1.1 A Schematic of the Experimental Facility

2.2 APPARATUS AND INSTRUMENTATION OF CONFINED VORTEX FLOW

The design criteria for the experimental apparatus involved consideration of its potential utilization in the future development of the project and the flexibility of the apparatus interface with purchased instrumentation. Every piece of apparatus and instrumentation performs a different function. Although accurate experimental results were always strived for, there is always an "uncertainty interval" or "uncertainty" attribute to the results obtained from the instruments [105]. The next two sections describe the details of the apparatus and the instruments which have been utilized in this project.

2.2.1 APPARATUS

The most important pieces of apparatus which have been designed to accommodate the special situations of this confined vortex flow project, follow.

1. Vortex Generator (Swirler) and Vortex Chamber

The detail structure of the vortex generator and chamber is shown in Figure 2.2.1. The vortex generator block redirects the air flow so that a tangential velocity component is created inside the flowfield. The whole vortex chamber is made of plexiglass for visualization purposes. The end plate of the chamber can be easily changed and several sizes of exit hole are available. The internal diameter of the chamber is 0.1397m (5.5 inches) and the length is adjustable up to 3.6576m (12 feet). All the machining

measurements are within an uncertainty of $\pm 2.54 \times 10^{-5} \text{m}$ ($\pm 0.001''$) or less than $\pm 1\%$ relative to the chamber diameter.

2. Conical Plug

A conical plug is utilized to find out the effect of pressure drop reduction across the vortex chamber. The shape and size of the plug will be shown in detail chapter 5. The position of the conical plug is controlled by a screw type transverse mechanism which has an uncertainty of $\pm 2.54 \times 10^{-5} \text{m}$ ($\pm 0.001''$) or less than $\pm 1\%$ relative to the distance between the tip of the cone and the exit plane of the chamber.

2.2.2 INSTRUMENTATION

A few vital instruments have been selected to complete the whole experimental set up of this project. The important ones will be described as follows:

1. Rotameter

The rotameter measures the volumetric flow rate of the inlet air. The scale is calibrated in Standard Cubic Feet per Minute (SCFM) at 101.4 KN/m^2 (14.7 psia) and 273°K . Its uncertainty is $\pm 4.7195 \times 10^{-4} \text{ m}^3/\text{s}$ ($\pm 1 \text{ SCFM}$) at standard condition which is 101.4 KN/m^2 at 273°K , this implies a $\pm 1.4\%$ to $\pm 2.0\%$ uncertainty for the flow rates this experiment have been used.

2. Five Hole Pitot Probe

Due to the three dimensional nature of a confined vortex, a five hole pitot probe [106] is selected to find out the velocity components, static and

total pressure in the flowfield. Part of the physical appearance of the probe and its dimensions are drawn in Figure 2.2.2. The coordinate system associated with the five hole pitot probe is illustrated in Figure 2.2.3. The probe is mounted on a transverse mechanism which allows the probe to translate and rotate on its own axis. The entire mechanism can be slid along a rail which is parallel to the z-axis of the vortex chamber. After the desired axial position has been chosen, the whole mechanism can be anchored firmly on the rail to allow the probe to take the required measurements. The uncertainty of the mechanism is $\pm 2.54 \times 10^{-4} \text{m}$ ($\pm 0.01''$) or maximum $\pm 6\%$ relative to the minimum distance measured in the r-direction and $\pm 0.2^\circ$ or less than $\pm 1\%$ in reference to the least angle obtained in the angular measurement.

3. Inclined Manometer

The static pressure readings recorded from the probe and the inlet pressure taps are obtained by two inclined manometers. The manometers can be adjusted to three different inclined positions giving an uncertainty of $\pm 1.27 \times 10^{-4} \text{m}$ ($\pm 0.005''$) of H_2O (lowest) to $\pm 2.54 \times 10^{-3} \text{m}$ ($\pm 0.1''$) or maximum $\pm 7\%$ of H_2O (vertical) position.

2.3 EXPERIMENTAL PROCEDURE

For a typical experimental test, the following sequence of steps are suggested to follow:

- 1) Assemble the desired length and exit diameter of the vortex chamber.
- 2) Choose a suitable swirling angle for the vortex generator.

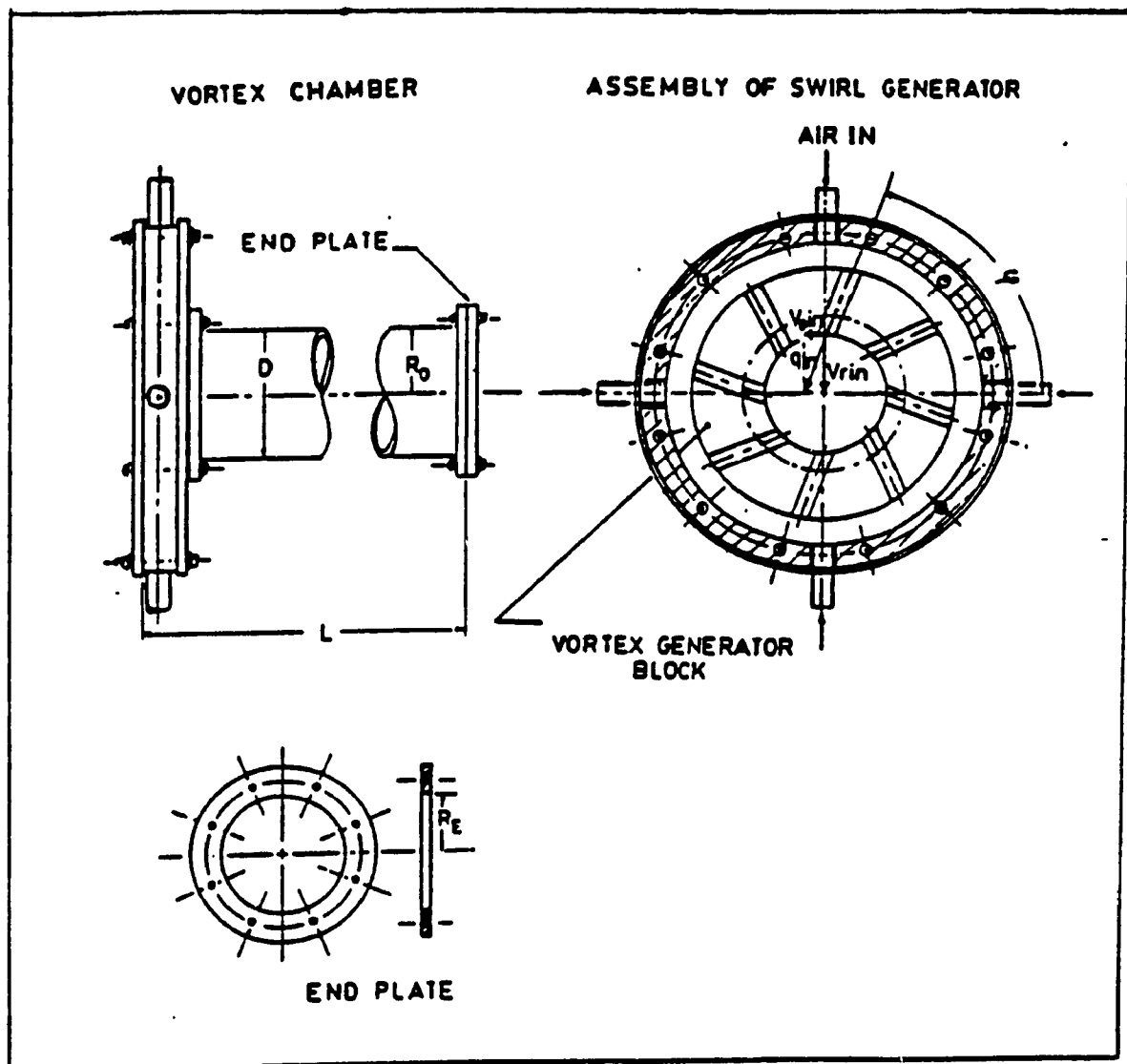


Figure 2.2.1 The Vortex Generator Assembly and the Vortex Chamber

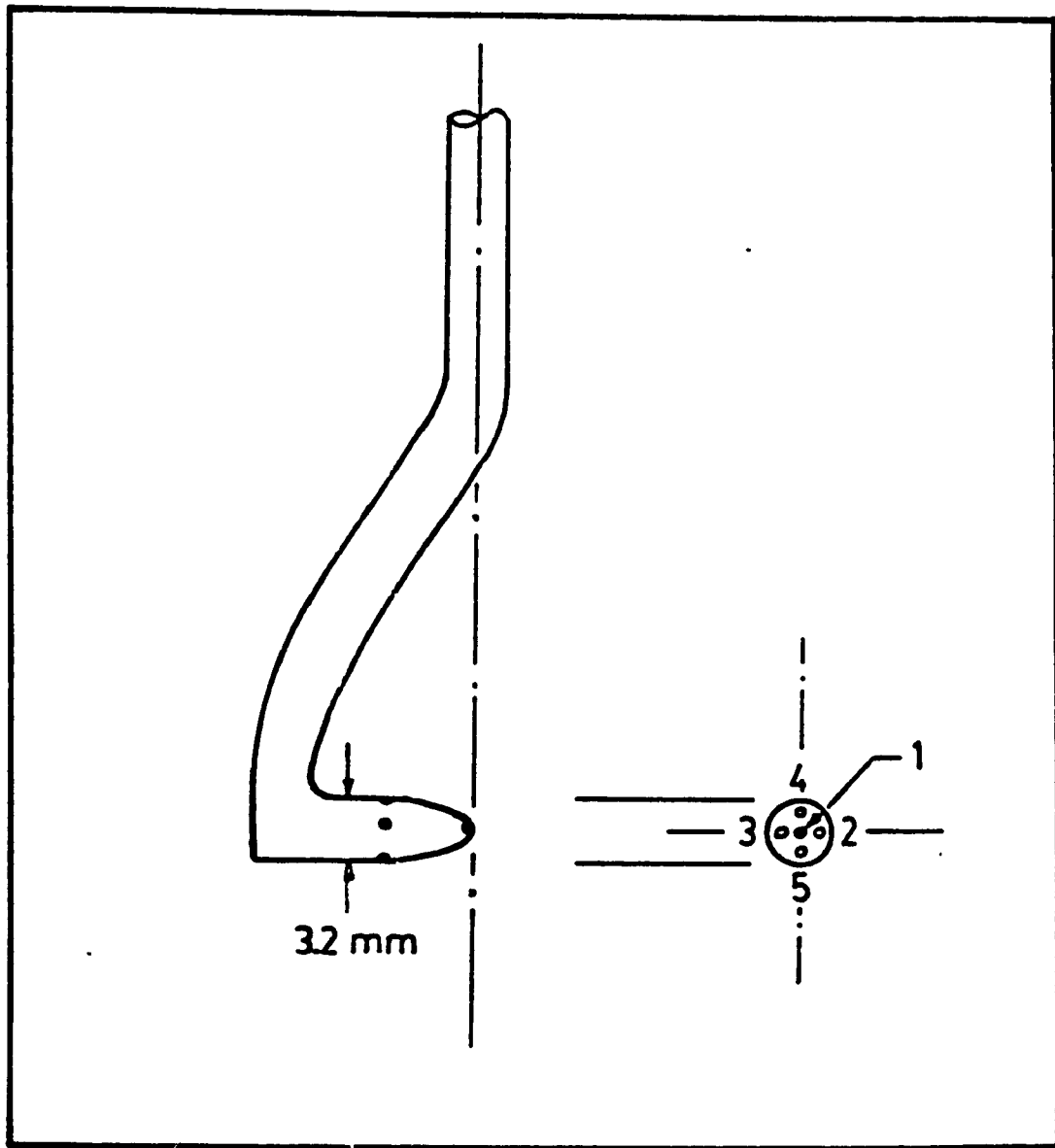


Figure 2.2.2 The Five Hole Pitot Probe

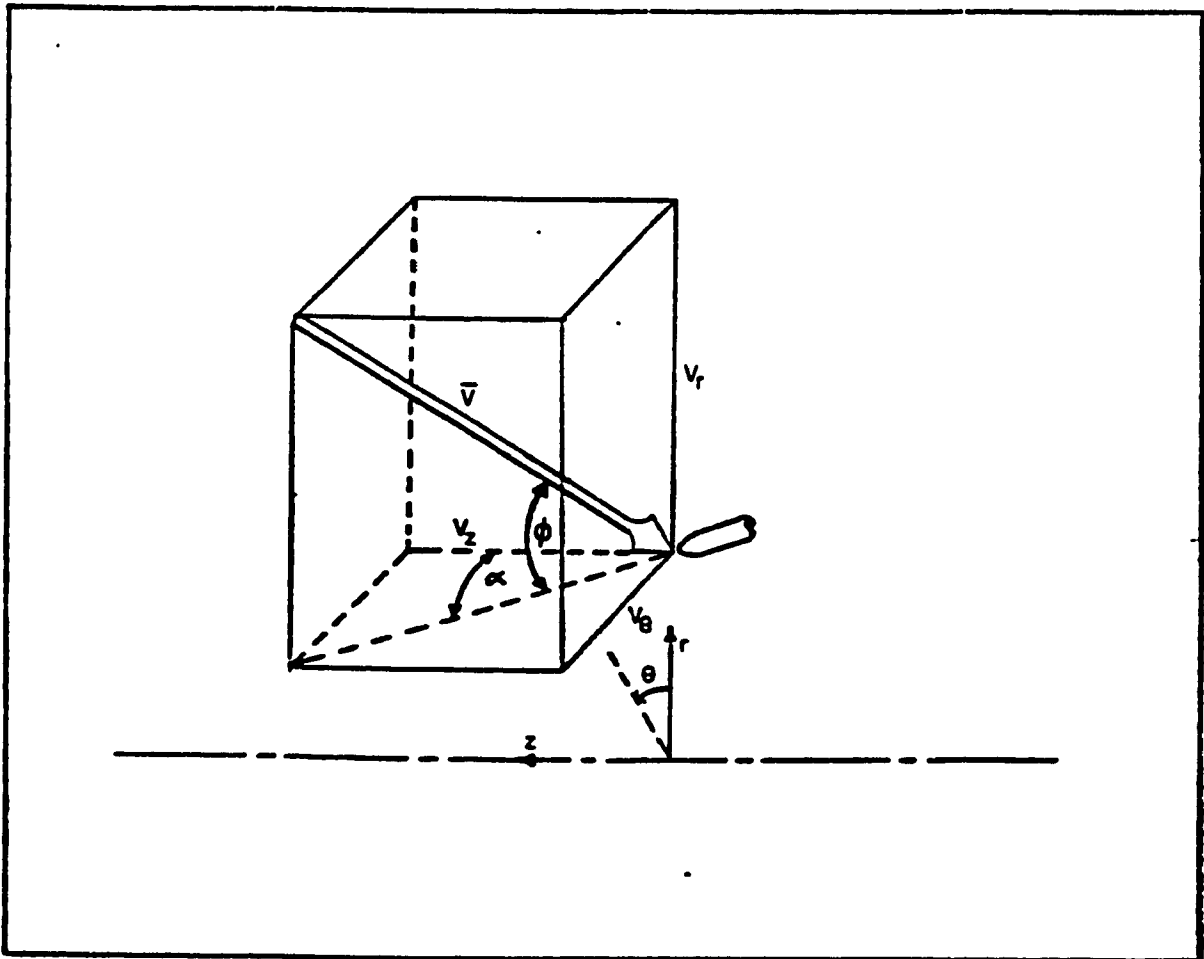


Figure 2.2.3 The 3-D Coordinate System with
the Velocity Components

- 3) Slide the transverse mechanism along the rail until a preferred axial position has been selected.
- 4) Insert the probe into the chamber to a desired radial position and then tighten every part of the mechanism except the tuner for the yaw angle α .
- 5) Turn on the air supply valve until the required flow rate is reached, as indicated by the rotameter.
- 6) With probe situated at a particular position (r_1, θ_1, z_1) , rotate it about its axis until pressure 2 and 3 are balanced. At this moment, hole #1 has been aligned with the projection of the total velocity vector \vec{V} in the z - θ plane.
- 7) Record the pressure differences $P_1 - P_{amb}$, $P_1 - P_2$ and $P_4 - P_5$ and the yaw angle α .
- 8) Move the probe to another radial position and repeat the process from step 6.
- 9) When a complete set of radial transverse data has been taken, go to another axial position to repeat the whole process.

After each test at a particular position (r_1, θ_1, z_1) , the following data should be recorded: the yaw angle α , $P_1 - P_{amb}$, $P_1 - P_2$ and $P_4 - P_5$.

2.4 DATA DEDUCTION

After all the necessary experimental measurements have been taken, the pitch angle ϕ , the pressure coefficients which are the velocity pressure coefficient $\frac{P_t - P_s}{P_1 - P_2}$, and the total pressure coefficient $\frac{P_1 - P_t}{P_t - P_s}$ can be tabulated from the provided calibration chart. From the two pressure coefficients, the

total and static pressure of a local point at the flowfield can be calculated since P_1 and P_2 are obtained during the experiment. By using the Bernoulli's Equation, the magnitude of the total velocity at a particular position could be obtained as,

$$|\vec{V}| = \sqrt{2(P_t - P_s)/\rho} \quad (2.4.1)$$

where P_t and P_s are the total and static pressure respectively. The velocity components at that point could then be calculated from the following equations,

$$V_r = |\vec{V}| \sin\phi \quad (2.4.2)$$

$$V_\theta = |\vec{V}| \cos\phi \sin\alpha \quad (2.4.3)$$

$$V_z = |\vec{V}| \cos\phi \cos\alpha \quad (2.4.4)$$

where ϕ and α are the pitch and yaw angles respectively as defined in Figure 2.2.3. A computer program has been developed to handle the deduction of data in order to minimize the labour time.

There are a few points that are worth considering when using a five hole pitot probe in a three dimensional vortex flow field. Errors will be inevitably introduced into the experimental results, but can be minimized by applying the following techniques. The probe should be relatively small compared to the vortex chamber. A comparatively large probe will disturb the vortex or even destroy the swirling flowfield. The size of the probe is usually fixed due

to manufacturing reasons, therefore the experimental results could be improved if a relatively bigger chamber is used.

Due to the presence of a strong centrifugal flow field inside the vortex chamber, the measured $P_4 - P_5$ values may not be the exact value contributed by the velocity components. The measured $P_4 - P_5$ values contain the contribution induced by the radial static pressure field [106]. This error may be significant if the local pressure gradient is high. If the probe is located below the center line, hole 4 is always above hole 5. This implies the measured value $P_4 - P_5$ is lesser in magnitude than the actual one. In the other case, the probe is above the center line, then the measured value will be greater in magnitude than the actual one. This problem is illustrated in Figure 2.4.1. From the diagram, one can conclude that the radial pressure profile has a lot of influence on the $P_4 - P_5$ readings. A numerical method has been developed to approximate the error and deduce better results in the velocity and pressure values.

The concept of this numerical scheme is to obtain a radial static pressure field from the original experimental data. Then this radial static pressure profile was used to calculate its pressure contribution to $P_4 - P_5$ at each local point. After obtaining the pressure errors, the $P_4 - P_5$ values are updated and all the procedures for the velocities and static pressure values are recalculated. The new tabulated results are compared with the previous ones to verify that they are within a preset tolerance. If they are so, the deduced results are accepted or else the iteration process is repeated by using the new radial static pressure profile to estimate the pressure errors induced on $P_4 - P_5$ values.

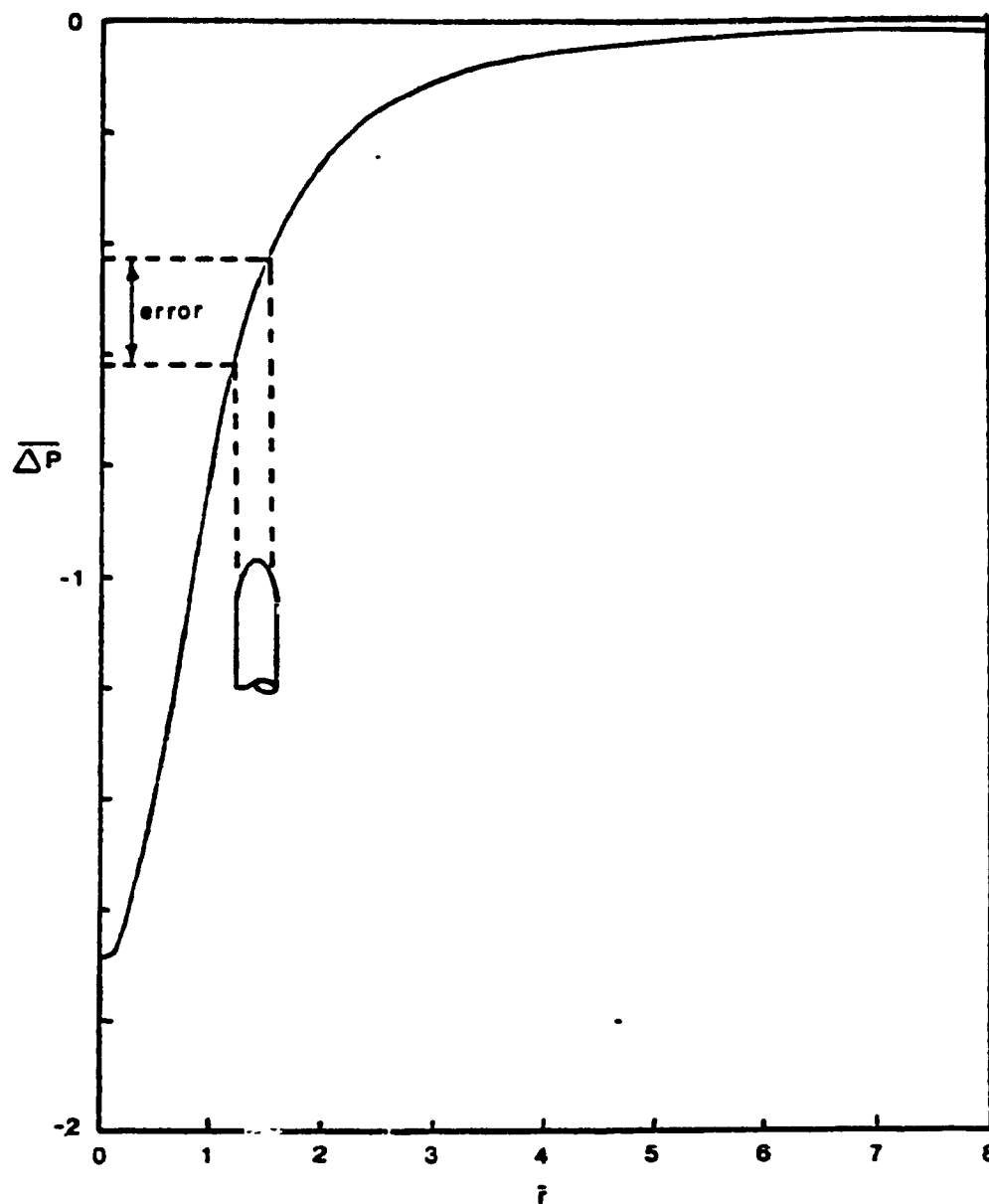


Figure 2.4.1 Errors which Introduced to the Probe
by the Radial Static Pressure Field

Throughout the numerical iteration process, the cubic spline polynomials interpolation technique is used in order to simplify the computation. For a polynomial which is in the range of (X_i, X_{i+1}) is [108],

$$Y = F_i(X) = A_i (X-X_i)^3 + B_i (X-X_i)^2 + C_i (X-X_i) + D_i \quad (2.4.5)$$

for $X_i \leq X \leq X_{i+1}$

where X_i and Y are the independent and dependent variables respectively.

The boundary conditions of each cubic spline polynomial will vary from different cases, they depend on the physical situations that the problem will face. The provided calibration graphs from the manufacturer are numerically converted into three cubic spline polynomials. The chosen boundary condition is zero bending moment, that is free boundary condition, at the ends of the three different calibration curves. After obtaining the cubic spline for the three calibration curves, the computation procedure of the velocity components and pressure values has been largely simplified. The assumptions which have been taken into account are constant air density, steady and axisymmetric flow. The deduced radial static pressure field will also be represented by a cubic spline polynomial. In that case, the independent variable is \bar{r} (non-dimensional radius r/R_O) and the dependent variable is C_p (pressure coefficient). \bar{r} and C_p will be defined later in this section. The boundary conditions are zero slope near the center and zero bending moment (free boundary condition) near the wall. The separation distance between hole 4 and hole 5 on the tip of the probe is $2.794 \times 10^{-3} \text{m}$ (0.11"), or $2.794 \times 10^{-3} \text{m} / 0.06985 \text{m}$ (or $0.11" / 2.75"$) = 0.04 in nondimensional

form. Therefore it is 0.02 from the center hole 1. The polynomial in the interval of $(\bar{r}_i, \bar{r}_{i+1})$ is,

$$C_p = F_i(\bar{r}) = A_i (\bar{r} - \bar{r}_i)^3 + B_i (\bar{r} - \bar{r}_i)^2 + C_i (\bar{r} - \bar{r}_i) + D_i \quad (2.4.6)$$

for $\bar{r}_i \leq \bar{r} \leq \bar{r}_{i+1}$

where $C_p = 2(P_{\text{wall}} - P(\bar{r})) / \rho q_{\text{in}}^2$

$$\bar{r} = r / R_O$$

$R_O = 0.06985\text{m}$ (2.75", radius of the vortex chamber)

Hence, the values of C_{P4} and C_{P5} at the i -th radial position are,

$$C_{P4} = A_{i-1} \delta r^3 + B_{i-1} \delta r^2 + C_{i-1} \delta r + D_{i-1} \quad (2.4.7)$$

and

$$C_{P5} = A_i (0.02)^3 + B_i (0.02)^2 + C_i (0.02) + D_i \quad (2.4.8)$$

where $\delta r = (\bar{r}_i - 0.02) - \bar{r}_{i-1}$

$C_{P4} = C_p$ value of point 4 at the pitot probe

$C_{P5} = C_p$ value of point 5 at the pitot probe

It can be easily shown that,

$$C_{P4} - C_{P5} = -2(P_4 - P_5) / \rho q_{\text{in}}^2 \quad (2.4.9)$$

Therefore at the i-th radial position, on can get

$$(P_4 - P_5)_{\text{actual}} + (P_4 - P_5)_{\text{error}} = (P_4 - P_5)_{\text{expt}} \quad (2.4.10)$$

or

$$(P_4 - P_5)_{\text{actual}} = (P_4 - P_5)_{\text{expt}} - \text{error} \quad (2.4.11)$$

$$\text{where error} = - (1/2)\rho q_{\text{in}}^2 (C_{P4} - C_{P5})$$

Hence the iterative procedure for a particular axial position can be summarized as:

1. Input the measured experimental pressure readings (P_1 to P_5 from the probe) and the yaw angle α (from the transverse mechanism).
2. Calculate the pitch angle ϕ , velocity pressure coefficients $\frac{P_t - P_s}{P_1 - P_2}$ and the total pressure coefficients $\frac{P_t - P_t}{P_1 - P_s}$ from the three cubic spline calibration polynomials created from the manufacturer's graph.
3. Obtained the static and total pressure and the velocity components.
4. Create a cubic spline for the deduced radial static pressure field.
5. Calculate the local error at each radial location for the whole axial position through interpolation of the cubic spline polynomial.
6. Check the difference between the new and old error, if it does not meet the required tolerance, then the new error will be added to or subtracted from the measured $P_4 - P_5$. Go to step 2.
7. If the tolerance has been met, then stop the iteration.

As mentioned in section 2.3, a complete FORTRAN program has been developed to handle the data deduction process. The source code is listed in Appendix I for reference purpose.

2.5 RELIABILITY OF THE RESULTS DUE TO OSCILLATION OF THE VORTEX CORE

Visualization experiments have shown that the vortex core is under the influence of transverse wave fronts. The whole core oscillates about the axis of symmetry with a certain amplitude and frequency. At the same time, wave trains propagate along the core giving the impression of standing waves. In other situations, bending of the core might be present.

If a probe is located near or inside the core, the measured pressure values are not expected to be the true values due to the above mentioned core behavior. Hence the deduced velocity values may be more or less than the true value depending on the amplitude of the oscillation. However it is certain that the deduced absolute maximum of the velocity profile must be less than the corresponding true value. This concept is illustrated in Figure 2.5.1 and 2.5.2 by using the Burger's tangential velocity profile. The concept of absolute maximum can be easily understood since the adjacent velocity values must be less than the absolute maximum. Hence, the measured maximum value (which can be treated as the mean value due to oscillation) has to be less than the true maximum.

In Figure 2.5.2, it shows the measuring magnitude of the maximum tangential velocity component versus time. The pitot probe was actually

measuring an oscillating signal as shown in this figure. If the measured signal is averaged out, an average value which is always less than the true maximum value would be obtained.

The observed amplitude of oscillation is small compared to the size of the core. Quantitative measurements of the oscillations have not been taken. However, it can be concluded from the visualization experiments that the amplitude of oscillation is less than 5% of the core size. The oscillations definitely has some effects on the measuring data but it seems to be insignificant in any aspects. Hence, the deduced data is considered reliable within the acceptable tolerance.

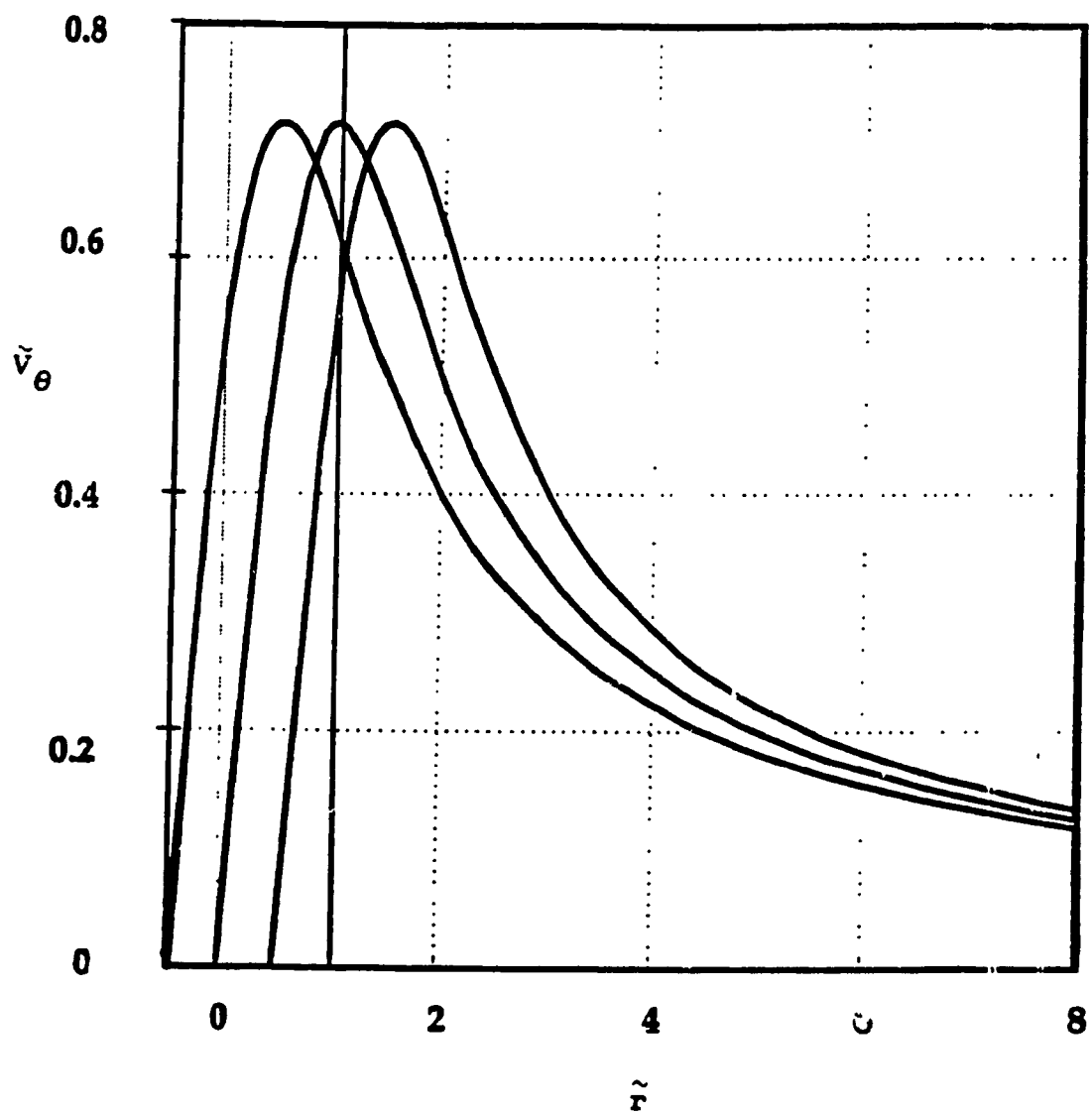


Figure 2.5.1 Three Tangential Velocity Profiles to Illustrate the Concept of Maximum

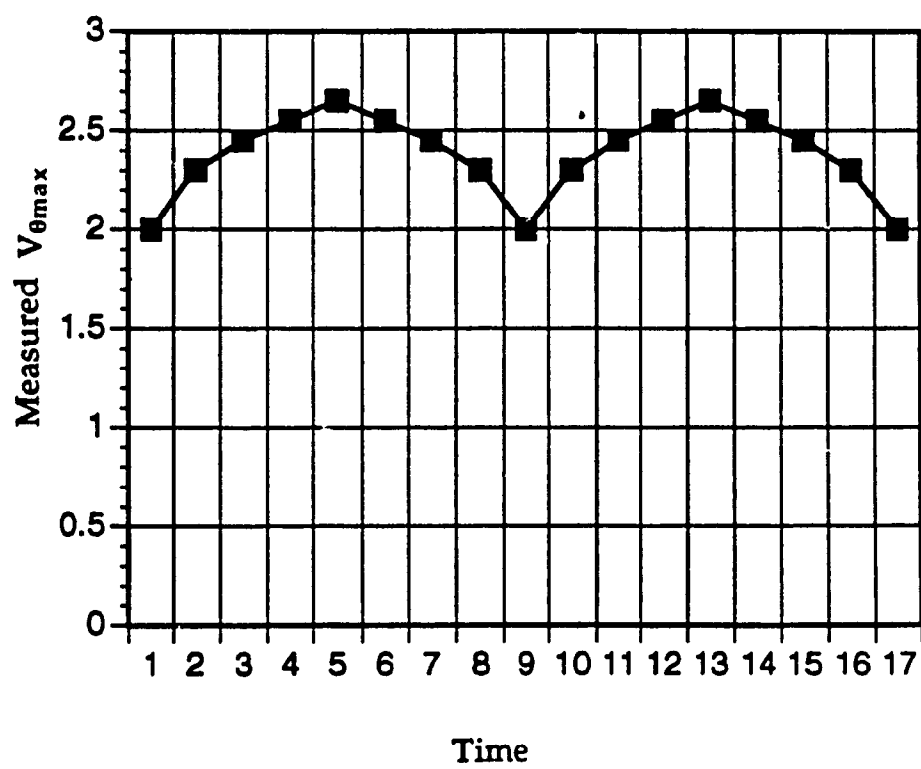


Figure 2.5.2 Measured Maximum Tangential Velocity Component vs. Time

CHAPTER 3

DIMENSIONAL ANALYSIS OF CONFINED VORTEX FLOWS

Complete solutions to fluid mechanics problems can seldom be obtained by analytical methods alone. Experiments are usually necessary for comprehensive determination of the relationships between variables. Dimensional analysis has proved very useful in reducing to a minimum the number of experiments required. Although dimensional analysis is not producing analytical solutions to the problems, it does provide useful information about the form of mathematical relations connecting the relevant variables, and suggests the most effective way of grouping the variables together.

Dimensional analysis will be applied to the problem of confined vortex flows. Based on the past experiences and some assumptions, a set of independent and dependent dimensionless variables have been developed. The analysis is divided into two main parts. The first one will be performed on the core radius inside and at the exit of the vortex chamber, then the velocities and pressures will be examined in detail. The following dimensional analysis concentrates on a chamber with an aspect ratio of 1.0-3.0, or so called "short chamber".

There are not many researchers that have provided the dimensional analysis results of confined vortex flow. However, some researchers did try to develop certain analytical models which can be fitted into their experimental

data. Escudier et al [114] had found a mathematical model which represents their experimental data of tangential velocity component. Garg and Leibovich [115] also discovered analytical profiles for axial and tangential velocity components. Despite all the previous effort, no concrete conclusions have been developed to generalize most of the important physical components of confined vortex flows.

3.1 DIMENSIONAL ANALYSIS ON THE CORE RADIUS

If the core radius inside the chamber remains uniform except near the exit and the viscous effect is negligible. The inlet swirling strength of a vortex will certainly affect the size of the core. Hence, the core radius is depend on the inlet vortex strength, $\Gamma = 2\pi R_O q_{in} \cos\phi$, the volumetric flow rate, $Q = q_{in} A_{in}$, and the exit radius, R_E . Mathematically, R_{CD} and R_{CF} can be expressed as follows,

$$R_{CD} = f_1 (\Gamma, Q, R_E) \quad (3.1.1)$$

and

$$R_{CF} = f_2 (\Gamma, Q, R_E) \quad (3.1.2)$$

where R_{CD} = core radius inside the chamber

R_{CF} = core radius at the exit

f_1 or f_2 = any mathematical functions

R_O = radius of the vortex chamber

ϕ = inlet flow angle measured from the tangent to the inlet velocity

A_{in} = inlet flow area at the swirler

q_{in} = inlet total velocity

R_E = exit radius

There are only two basic dimensions involved in Eqs.(3.1.1) and (3.1.2), which are the length and time scale [116]. Hence, there may be only one independent parameter for both of the equations. The dependent parameters are obviously R_{CD}/R_E and R_{CF}/R_E for Eqs.(3.1.1) and (3.1.2) respectively. The independent parameter can be easily derived as $Q/(R_E\Gamma)$. Therefore,

$$R_{CD}/R_E = f_1(Q/(R_E\Gamma)) \quad (3.1.3)$$

and

$$R_{CF}/R_E = f_2(Q/(R_E\Gamma)) \quad (3.1.4)$$

To simplify the above equations, Γ and Q can be expressed in terms of the inlet conditions and the geometric parameters of the vortex chamber. Since $\Gamma = 2\pi R_O q_{in} \cos\phi$ and $Q = q_{in} A_{in}$,

hence Eqs.(3.1.3) and (3.1.4) can be written as,

$$X_{CD} = \frac{R_{CD}}{R_E} = f_1 \left(\frac{A_{in}/A_O}{(R_E/R_O) \cos \phi} \right) \quad (3.1.5)$$

and

$$X_{CF} = \frac{R_{CF}}{R_E} = f_2 \left(\frac{A_{in}/A_O}{(R_E/R_O) \cos \varphi} \right) \quad (3.1.6)$$

or

$$X_{CD} = f_1(\beta) \quad (3.1.7)$$

and

$$X_{CF} = f_2(\beta) \quad (3.1.8)$$

$$\text{where } \beta = \left(\frac{A_{in}/A_O}{(R_E/R_O) \cos \varphi} \right)$$

The above equations indicate that X_{CD} and X_{CF} wholly depend on the geometric parameter β . The parameter β , defined as the ratio of the axial to tangential momenta, is the reciprocal of the swirl number S , i.e. $S = 1/\beta$, often quoted in the technical literature. Based on the value of β , swirling flows may be characterized as follows:

- (i) strongly swirling if $\beta < \sim 1.70$ (or $S > \sim 0.60$)
- (ii) medium swirl if $1.70 < \beta < 2.50$ (or $0.40 < S < 0.60$)
- (iii) weakly swirl if $\beta > \sim 2.50$ (or $S < \sim 0.40$)

In the next section, R_{CD} will be used as a reference in some of dimensional relationships. From the experiment, the normalized R_{CD} ($X_{CD} = R_{CD}/R_E$) was shown to be a function of the geometric parameter β . Therefore, a least squares curve can be fitted to the experimental data to obtain a numerical relationship between β and X_{CD} . Hence, for a known

value of β , the core size R_{CD} can be approximately calculated from the least squares curve which could be calculated from the experimental data. If there is insufficient experimental data for the curve fit, the theoretical analysis [107] is still available for the approximation of the core size R_{CD} .

3.2 DIMENSIONAL ANALYSIS ON VELOCITIES AND PRESSURES

The dependent variables involved in this section are the three velocity components, namely V_θ (tangential), V_r (radial) and V_z (axial). The second set of dependent variables are the static pressure inside the chamber, $P(r)$, and the inlet static and dynamic pressure, $(P_{in} - P_{amb}) + \rho q_{in}^2/2$. The following equations show the relationship between the dependent and the independent variables. Each equation will be examined in detail in the forthcoming section.

$$P - P_{wall} = f_3(r, \rho, \Gamma, R_{CD}) \quad (3.2.1)$$

$$(P_{in} - P_{amb}) + \rho q_{in}^2/2 = f_4(\rho, \Gamma, Q, R_E) \quad (3.2.2)$$

$$V_\theta = f_5(r, \Gamma, R_{CD}) \quad (3.2.3)$$

$$V_r = f_6(r, z, R_O, \nu, \Gamma, Q, R_E) \quad (3.2.4)$$

$$V_z = f_7(r, z, R_O, \nu, \Gamma, Q, R_E) \quad (3.2.5)$$

where ρ = density of the fluid

ν = kinematic viscosity of the fluid

$f_3, f_4, f_5, f_6, \text{ or } f_7$ = any mathematical functions

P_{amb} = ambient pressure

P_{in} = inlet static pressure

Q = volumetric flow rate

q_{in} = inlet total velocity

R_{CD} = core radius inside the chamber

R_{E} = exit radius

R_{O} = radius of the vortex chamber

Γ = inlet vortex strength

Examining Eq.(3.2.1) which is

$$P - P_{\text{wall}} = f_3(r, \rho, \Gamma, R_{\text{CD}})$$

$P - P_{\text{wall}}$ is dependent on r because the flow is assumed to be axisymmetric and also the axial effect is negligible. Parameters ρ and Γ are the other two independent variables because the pressure relies on the density of the fluid and the strength of the vortex inside the chamber. The static pressure term balances the centrifugal force, which maintains the flow stability inside the chamber, hence ρ and Γ are involved. There are 3 basic dimensions in the equation, mass, length and time. Five variables are involved, hence $5-3=2$, this implies there may be a maximum of 2 nondimensional parameters that could be found. One independent parameter is obviously r/R_{CD} , and the dependent parameter can be derived as,

$$\frac{P - P_{\text{wall}}}{\frac{1}{2}\rho\left(\frac{\Gamma}{R_{\text{CD}}}\right)^2}$$

where P_{wall} is the known static pressure at R_O . From the experiment, for a short chamber and strong swirl, P_{wall} is found to be approximately equal to P_{in} . Since Γ , the inlet vortex strength, can be expressed as follows,

$$\Gamma = 2\pi R_O q_{\text{in}} \cos\varphi \quad (3.2.6)$$

then by replacing Γ in the dependent parameter with the above expression, one obtains,

$$\frac{P - P_{\text{wall}}}{\frac{1}{2}\rho\left(\frac{\Gamma}{R_{\text{CD}}}\right)^2} = \frac{2(P - P_{\text{wall}})}{\rho q_{\text{in}}^2} \left[\frac{R_{\text{CD}}/R_O}{\cos\varphi} \right]^2 \frac{1}{4\pi^2} \quad (3.2.7)$$

Eliminating the constant term $1/(4\pi^2)$ in Eq.(3.2.7), the dependent parameter becomes

$$\frac{2(P - P_{\text{wall}})}{\rho q_{\text{in}}^2} \left[\frac{\xi}{\cos\varphi} \right]^2$$

where $\xi = R_{\text{CD}}/R_O$. Hence the final form of Eq.(3.2.1) can be rewritten as,

$$\overline{\Delta P} = \frac{2(P - P_{\text{wall}})}{\rho q_{\text{in}}^2} \left[\frac{\xi}{\cos\varphi} \right]^2 = f_3(\tilde{r}) \quad (3.2.8)$$

where $\tilde{r} = r/R_{\text{CD}}$

Eq.(3.2.2) states that,

$$(P_{in} - P_{amb}) + \rho q_{in}^2/2 = f_4(\rho, \Gamma, Q, R_E)$$

Eq.(3.2.2) relates the inlet total pressure term to the exit radius R_E , the inlet volumetric flow rate Q , the fluid density ρ and inlet swirling strength Γ . The first independent parameter $Q/(R_E\Gamma)$ can be easily derived. However, from the previous analysis, the above parameter is the same as β which is defined as follows,

$$\beta = \frac{A_{in}/A_O}{(R_E/R_O) \cos \varphi}$$

The dependent parameter can be written in the following nondimensional form as,

$$\frac{(P_{in} - P_{amb}) + \frac{1}{2}\rho q_{in}^2}{\frac{1}{2}\rho \left[\frac{\Gamma}{R_E} \right]^2}$$

The above expression can be further simplified , since $\Gamma = 2\pi R_O q_{in} \cos \varphi$,

$$\frac{(P_{in} - P_{amb}) + \frac{1}{2}\rho q_{in}^2}{\frac{1}{2}\rho q_{in}^2} \frac{1}{4\pi^2} \left[\frac{R_E/R_O}{\cos \varphi} \right]^2 = \left[\frac{2(P_{in} - P_{amb})}{\rho q_{in}^2} + 1 \right] \frac{1}{4\pi^2} \left[\frac{R_E/R_O}{\cos \varphi} \right]^2$$

Without loss of generality, the constant term $1/4\pi^2$ can be dropped and the dependent variable obtained as,

$$\left[\frac{2(P_{in} - P_{amb})}{\rho q_{in}^2} + 1 \right] \left[\frac{R_E/R_O}{\cos \varphi} \right]^2$$

The above expression is named $\widetilde{\Delta P}$, hence for Eq.(3.2.2), the final form is,

$$\widetilde{\Delta P} = f_4 (\beta) \quad (3.2.9)$$

For Eq.(3.2.3) which relates the tangential velocity component to the various parameters is,

$$V_\theta = f_5 (r, \Gamma, R_{CD})$$

There are 4 variables and 2 basic dimensional units, which are length and time. In the tangential direction, the viscosity of the fluid is not involved because tangential velocity is the dominant velocity component among the three velocity components. Since the inertia effects dominate, viscosity effect can be considered as negligible in that direction. This fact had been substantiated by experimental results. V_θ is definitely varying in the radial direction and the inlet swirling strength of the vortex will also have an effect on it. The independent parameter is r/R_{CD} which is called \tilde{r} . The dependent parameter can be obtained as,

$$\frac{V_\theta}{\Gamma/R_{CD}}$$

The above expression can be further simplified since $\Gamma = 2\pi R_O q_{in} \cos\phi$ and $V_{\theta in} = q_{in} \cos\phi$, hence $\Gamma = 2\pi R_O V_{\theta in}$, then,

$$\frac{V_\theta}{\Gamma/R_{CD}} = \frac{V_\theta R_{CD}}{2\pi R_O V_{\theta in}} = \frac{V_\theta}{V_{\theta in}} \left[\frac{R_{CD}}{R_O} \right] \frac{1}{2\pi} \quad (3.2.10)$$

Without loss of generality, the constant term which is $1/2\pi$ can be eliminated. Therefore the dependent parameter is, where $\xi = R_{CD}/R_O$,

$$\frac{V_\theta}{V_{\theta in}} \xi$$

and the final nondimensional equation is,

$$\frac{V_\theta}{V_{\theta in}} \xi = f_5(\tilde{r}) \quad (3.2.11)$$

The last two equations, Eqs.(3.2.4) and (3.2.5) are,

$$V_r = f_6(r, z, R_O, \nu, \Gamma, Q, R_E) \quad (3.2.4)$$

$$V_z = f_7(r, z, R_O, \nu, \Gamma, Q, R_E) \quad (3.2.5)$$

They are similar to each other. The two obvious independent parameters are r/R_O and z/R_O . The other independent parameter is $Q/(R_E \Gamma)$ which is β . The last one is the Reynolds Number, which is $Q/(\pi R_O \nu)$. The dependent parameter can be obtained as follows, since $Q/\pi R_O^2$ is the average axial velocity, $Q = A_{in} q_{in}$ and $A_O = \pi R_O^2$, hence the following can be derived,

$$\frac{V_z}{Q/\pi R_O^2} = \frac{V_z}{A_{in} q_{in}} \pi R_O^2 = \frac{V_z}{q_{in}} \frac{A_O}{A_{in}}$$

hence Eqs.(3.2.4) and (3.2.5) become

$$\frac{V_r}{q_{in}} \left[\frac{A_O}{A_{in}} \right] = f_6(\bar{r}, \bar{z}, \beta, Re) \quad (3.2.12)$$

$$\frac{V_z}{q_{in}} \left[\frac{A_O}{A_{in}} \right] = f_7(\bar{r}, \bar{z}, \beta, Re) \quad (3.2.13)$$

where $\bar{r} = r/R_O$
 $\bar{z} = z/R_O$
 $Re = Q/(R_O v)$

After the derivation, the above dimensional relationships can be summarized as follows,

$$\overline{\Delta P} = \frac{2(P - P_{wall})}{\rho q_{in}^2} \left[\frac{\xi}{\cos \varphi} \right]^2 = f_3(\tilde{r}) \quad (3.2.8)$$

$$\widetilde{\Delta P} = \left[\frac{2(P_{in} - P_{amb})}{\rho q_{in}^2} + 1 \right] \left[\frac{R_E/R_O}{\cos \varphi} \right]^2 = f_4(\beta) \quad (3.2.9)$$

$$\widetilde{V}_\theta = \left[\frac{V_\theta}{V_{\theta in}} \right] \xi = f_5(\tilde{r}) \quad (3.2.11)$$

$$\frac{V_r}{q_{in}} \left[\frac{A_O}{A_{in}} \right] = f_6(\bar{r}, \bar{z}, \beta, Re) \quad (3.2.12)$$

$$\frac{V_z}{q_{in}} \left[\frac{A_O}{A_{in}} \right] = f_7(\bar{r}, \bar{z}, \beta, Re) \quad (3.2.13)$$

where $\bar{r} = r/R_O$
 $\bar{z} = z/R_O$
 $\tilde{r} = r/R_{CD}$

$$\xi = R_{CD}/R_O$$

$$Re = Q/(R_O v)$$

3.3 VERIFICATION OF THE ANALYSIS

The first equation to undergo analysis is Eq.(3.1.7). It states that X_{CD} is a function of β . Laser Doppler Anemometer (LDA) results by Faler [117] and Vatistas' et al results [28] have been used along with the present experimental results. The graph in Figure 3.3.1 has clearly shown that there is a correlation between X_{CD} and β . However, the theoretical prediction [107] has overestimated the value of X_{CD} . Experiments have proved that X_{CD} decreases with increase of β as it is shown in Figure 3.3.1.

There are few ways to vary β . The first is to adjust A_{in}/A_O , the second way is to change R_E/R_O and the last method is to vary $\cos\phi$. An experiment which is running with a certain mass flow rate is discussed as an example. If A_{in}/A_O is increased, the inlet fluid flow velocity will be slowed down and hence the vortex strength will be weakened. As known from experiment, the static pressure at or near the core region is relatively low and is sub-atmospheric in most of the situations. Hence, a reverse flow will probably occur at the exit. Therefore most of the mass and energy should be transferred to the atmosphere through the outside of the core region. However, the inlet total velocity has been weakened (increase of A_{in}/A_O), it may directly affect the axial velocity component. That means the mass and energy transfer process will also be slowed down. By the principle of mass conservation, the same amount of mass has to be transferred in the same unit

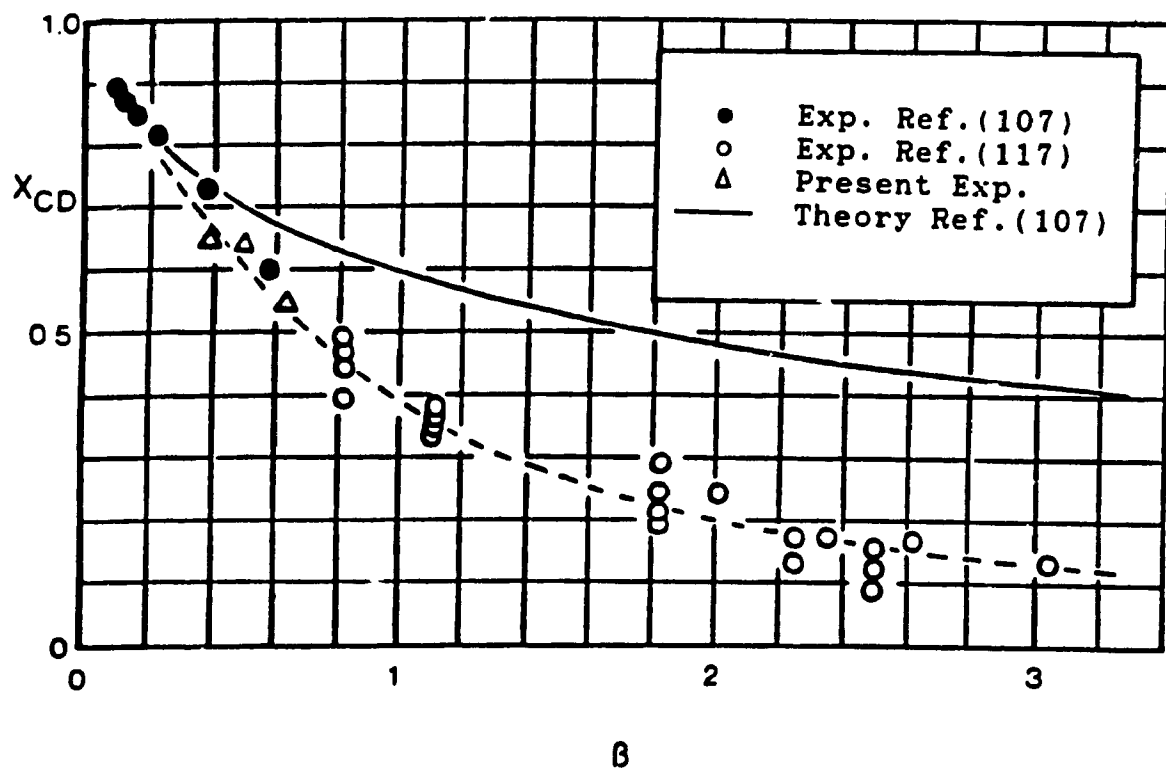


Figure 3.3.1 Nondimensional Core Radius X_{CD} vs. β

of time. Therefore, the core size will have to diminish in size in order to maintain the same mass transfer to the atmosphere.

The other way to increase β is to lower the value of R_E/R_O which is equivalent to reducing the exit area. This method will increase the axial velocity magnitude compared to a larger exit area. Although the axial velocity has been significantly increased, the core size still decreases in a relative manner.

This can be explained as follows, since mass flow rate = $\rho A_E V_E$

where ρ - Density of the fluid

A_E - Exit area (πR_E^2)

V_E - Axial exit velocity (average)

If R_E is decreased by 50%, the magnitude of the axial exit velocity has to be increased by 400% to keep the same mass flow rate. Experimental data showed that the axial velocity does not have that kind of increment when the exit area is lower. Hence, the other way to recover the mass transfer process is perhaps the decrease of the core size.

The last method to increase β is to decrease $\cos\phi$, this means to decrease the inlet swirling strength (Γ) of the vortex. When the inlet swirling strength of the vortex is decreased, the tangential velocity component will be decreased accordingly inside the chamber. That means there is a shift of momentum to the axial or radial direction since the inlet total velocity remains the same as before. This will indirectly change the momenta in the axial or radial direction. However, the shift of momentum has mainly happened in the

radial direction because the inlet velocity consists the tangential and radial components only. Experimental results showed that this leads to a decrease of the core size as it is shown in Figure 3.3.1.

For β larger than 0.4, the theoretical analysis [107] has overestimated the value of X_{CD} . The analysis utilized the free-forced (Rankine Vortex) vortex tangential velocity profile to calculate the core radius. The analysis assumed all the mass and energy are transferred outside the core region through the exit to the atmosphere. The core region becomes a stagnant and vacuum area and hence it has no contribution to the mass and energy transfer process. At the same time the analysis applied the energy equation (Bernoulli Equation) at the position of the core radius and was coupled with the mass equation to solve X_{CD} . The analysis did not consider the core region which is mainly a reverse flow region. Hence, the vortex model implies a lower axial velocity component to drive out the same amount of mass and energy. The key factor for the overestimation of X_{CD} is due to the fact that the analysis should have included reverse flow at the core region. Hence, the outward mass flow rate at the exit should have been the sum of the inlet mass flow rate and the reverse flow rate. However, to calculate the reverse flow rate is a very difficult task that most researchers are presently facing.

For Eq.(3.1.8), the relationship of X_{CF} and β has been demonstrated in Figure 3.3.2. The experimental data are well correlated by the theory in [107] for different values of β . However, the theoretical analysis of [111] and [112] do overestimate X_{CF} . For the solid line, it represents Eqns.(4.1.6) and (4.2.6) and they will be discussed in chapter 4.

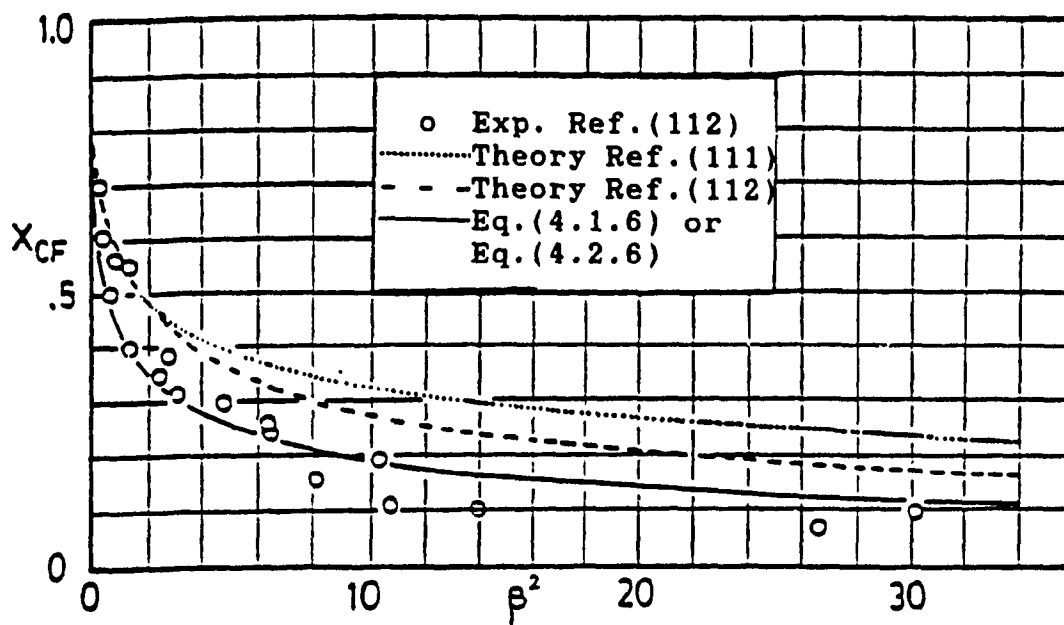


Figure 3.3.2 Nondimensional Exit Core Radius X_{CF} vs. β^2

The following analysis illustrates that an approximate solution of $\overline{\Delta P}(\tilde{r})$ can be obtained if the tangential velocity profile is a known function of \tilde{r} . Two tangential velocity profiles will be used to formulate the analysis and the derived $\overline{\Delta P}(\tilde{r})$ will be compared with the experimental data. As known from experiment, the tangential velocity component is dominant within the vortex flowfield. Hence for the radial equilibrium and a dominant tangential velocity V_θ , the following equation can be derived by considering the radial equilibrium [124],

$$\frac{\partial P}{\partial r} = \frac{\rho V_\theta^2}{r} \quad (3.3.3)$$

$$\text{since } \tilde{V}_\theta = \frac{V_\theta}{V_{\theta in}} \xi ; \tilde{r} = \frac{r}{R_{CD}} ; \xi = \frac{R_{CD}}{R_O}$$

Eqn.(3.3.3) can be transformed into,

$$\rho \frac{\tilde{V}_\theta^2 V_{\theta in}^2}{\tilde{r} R_{CD} \xi^2} = \frac{\rho q_{in}^2}{2 R_{CD}} \frac{\partial}{\partial \tilde{r}} \left[\frac{2(P - P_{wall})}{\rho q_{in}^2} \right] \quad (3.3.3a)$$

or

$$2 \frac{\tilde{V}_\theta^2}{\tilde{r}} = \frac{\xi^2}{\cos^2 \varphi} \frac{\partial}{\partial \tilde{r}} \left[\frac{2(P - P_{wall})}{\rho q_{in}^2} \right] \quad (3.3.4)$$

In Eqn.(3.3.4), the right hand side can further be simplified as,

$$2 \frac{\tilde{V}_\theta^2}{\tilde{r}} = \frac{\partial \overline{\Delta P}}{\partial \tilde{r}} \quad (3.3.5)$$

Eqn.(3.3.5) can then be integrated, the two limits are from any value \tilde{r} to the wall of the vortex chamber. However, R_O is usually much greater than R_{CD} , hence R_O/R_{CD} is approaching to a very large value. Therefore, the upper limit of the following definite integrals is replace by infinity or a very large value.

$$\int_{\tilde{r}}^{\infty} d\overline{\Delta P} = 2 \int_{\tilde{r}}^{\infty} \frac{\tilde{V}_{\theta}^2}{\tilde{r}} d\tilde{r} \quad (3.3.6)$$

The left hand side of Eqn.(3.3.6) can be written as,

$$\overline{\Delta P}(\tilde{r}) - \overline{\Delta P}(\tilde{r} \rightarrow \infty) = -2 \int_{\tilde{r}}^{\infty} \frac{\tilde{V}_{\theta}^2}{\tilde{r}} d\tilde{r} \quad (3.3.7)$$

where $\overline{\Delta P}(\tilde{r} \rightarrow \infty) \equiv 0$, hence the above equation results in a final form as,

$$\overline{\Delta P}(\tilde{r}) = -2 \int_{\tilde{r}}^{\infty} \frac{\tilde{V}_{\theta}^2}{\tilde{r}} d\tilde{r} \quad (3.3.8)$$

Eqn.(3.3.8) suggests that if the tangential velocity component is a function of \tilde{r} , the radial pressure can be solved in terms of the independent variable \tilde{r} . The modified Burgers' and Rankine vortices have been used in the following section to get an explicit radial pressure profile. The tangential velocity profile of the above mention vortices are as follows,

Modified Burgers' vortex:

$$\tilde{V}_\theta = \frac{1}{\tilde{r}} (1 - e^{-a\tilde{r}^2}) \quad (3.3.9)$$

The parameter a is a constant which is evaluated using the maximum tangential velocity condition at the core ($\tilde{r} = 1$). Since,

$$\frac{\partial \tilde{V}_\theta}{\partial \tilde{r}} = \frac{-1}{\tilde{r}^2} (1 - e^{-a\tilde{r}^2}) + 2ae^{-a\tilde{r}^2}$$

for $\tilde{r} = 1$, the above derivative is equal to zero or,

$$\frac{\partial \tilde{V}_\theta}{\partial \tilde{r}} = 0$$

The resulting equation of a is, $(2a+1)\exp(-a) - 1 = 0$. The root of the above equation is found to be approximately equal to 1.256.

Rankine vortex:

$$\tilde{V}_\theta = \tilde{r} \quad \text{for } 0 \leq \tilde{r} \leq 1 \quad (3.3.10a)$$

$$\tilde{V}_\theta = \frac{1}{\tilde{r}} \quad \text{for } 1 \leq \tilde{r} \leq \infty \quad (3.3.10b)$$

In Figure 3.3.3, the maximum tangential velocity $V_{\theta\max}/V_{\theta\text{in}}$ as a function of the parameter ξ (R_{CD}/R_O) is shown. Two theoretical curves have been derived from Eqns.(3.3.9) and (3.3.10) by setting $\tilde{r} = 1$. They are:

Modified Burgers' vortex:

$$\tilde{V}_\theta = \frac{1}{\tilde{r}} (1 - e^{-a\tilde{r}^2})$$

for $\tilde{r} = 1$, the resulting equation is,

$$\left[\frac{V_{\theta\max}}{V_{\theta\text{in}}} \right] \xi = 1 - e^{-a}$$

or

$$\frac{V_{\theta\max}}{V_{\theta\text{in}}} = \frac{0.715}{\xi} \quad (3.3.11)$$

Rankine vortex:

$$\tilde{V}_\theta = \tilde{r} \quad \text{for } 0 \leq \tilde{r} \leq 1$$

for $\tilde{r} = 1$, the resulting equation is,

$$\left[\frac{V_{\theta\max}}{V_{\theta\text{in}}} \right] \xi = 1$$

or

$$\frac{V_{\theta\max}}{V_{\theta\text{in}}} = \frac{1.000}{\xi} \quad (3.3.12)$$

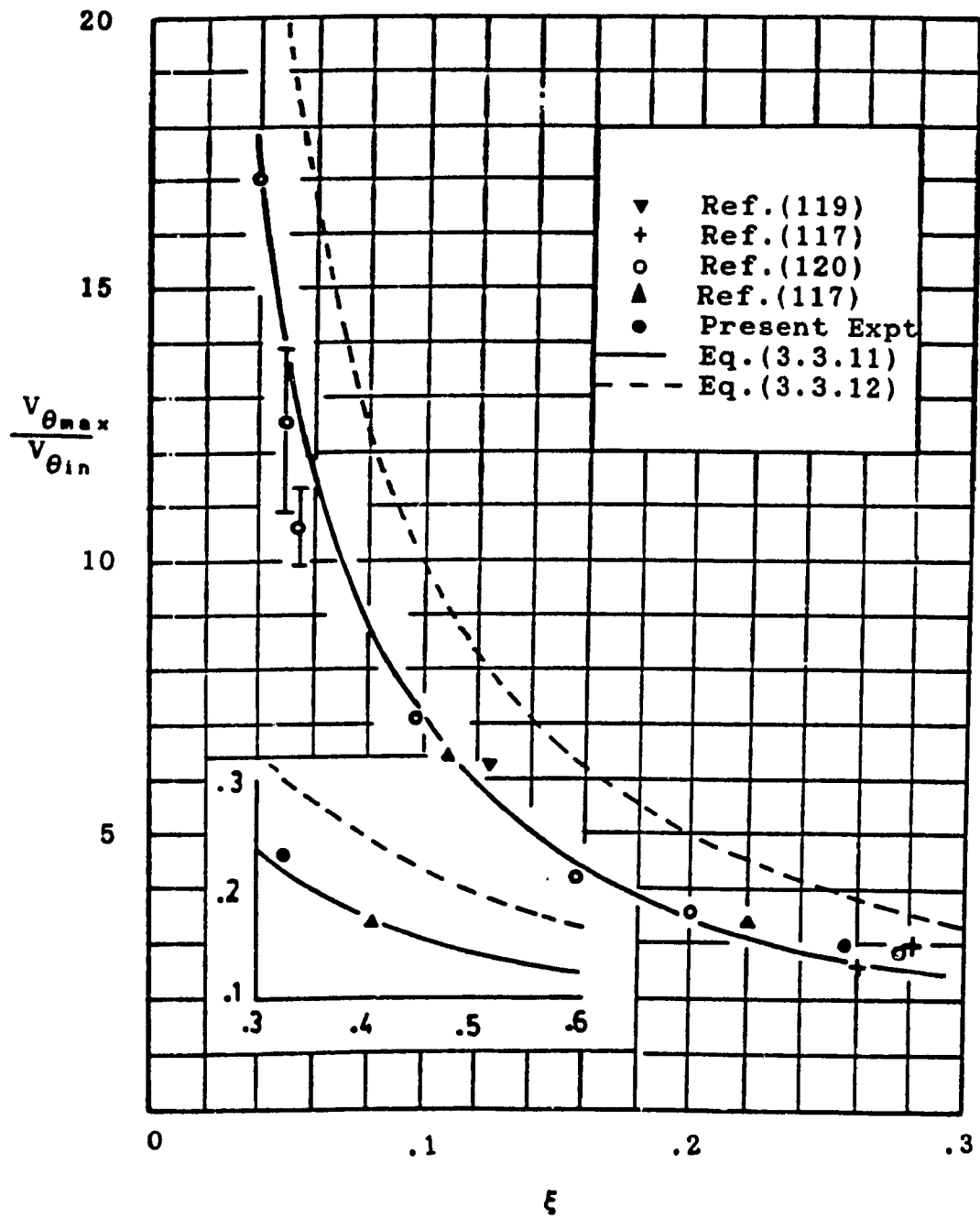


Figure 3.3.3 $\frac{V_{\theta_{max}}}{V_{\theta_{in}}}$ vs ξ

Figure 3.3.3 shows that the present and other experimental results correlate well with Eqn.(3.3.11) for ξ between 0.04 to 0.4. For Eqn.(3.1.12), it indicates an overestimation on $V_{\theta\max}/V_{\theta\text{in}}$ for the mentioned range of ξ .

By substituting Eqns.(3.3.9) and (3.3.10) into Eq.(3.3.8), two separate radial pressure formulas (for Burgers' and Rankine) can be obtained.

Pressure equation for modified Burgers' Vortex:

$$\overline{\Delta P}(\tilde{r}) = - \frac{(1 - e^{-a\tilde{r}^2})^2}{\tilde{r}^2} - 2a[\text{Ei}(-a\tilde{r}^2) - \text{Ei}(-2a\tilde{r}^2)] \quad (3.3.13a)$$

$$\text{where } \text{Ei}(-x) = - \int_x^\infty \frac{e^{-z}}{z} dz$$

For different radii \tilde{r} , $\overline{\Delta P}$ values are listed in Table (3.3.1). In the limiting case when \tilde{r} is approaching to zero, $\overline{\Delta P}$ can be obtained as,

$$\overline{\Delta P}(\tilde{r} \rightarrow 0) = - \lim_{\tilde{r} \rightarrow 0} \left[\tilde{r} - \sum_{m=2}^{\infty} \frac{(-a)^m \tilde{r}^{2m-1}}{m!} \right]^2 - 2a \int_0^\infty \frac{\exp(-a\tilde{r}^2) - \exp(-2a\tilde{r}^2)}{\tilde{r}^2} d(\tilde{r}^2) \quad (3.3.13b)$$

since the first term, the McLaurient expansion of the velocity, on the right hand side of Eqn.(3.3.13b) is zero and from [113],

$$\int_0^\infty \frac{\exp(-px) - \exp(-qx)}{x} d(x) = \ln\left(\frac{q}{p}\right)$$

Table (3.3.1) Values of $\overline{\Delta P}$ as a function of radii \tilde{r}

\tilde{r}	$\overline{\Delta P}$	\tilde{r}	$\overline{\Delta P}$	\tilde{r}	$\overline{\Delta P}$
0.0	1.74118	0.9	0.92146	4.0	0.06250
0.1	1.72562	1.0	0.81426	5.0	0.04000
0.2	1.67966	1.2	0.63090	6.0	0.02778
0.3	1.60688	1.4	0.48954	7.0	0.02040
0.4	1.51228	1.6	0.38430	8.0	0.15620
0.5	1.40124	1.8	0.30682	9.0	0.01234
0.6	1.22800	2.0	0.24950	10	0.01000
0.7	1.15872	2.5	0.16000	50	0.00040
0.8	1.03720	3.0	0.11110	100	0.00010

for the above expression, $p = a$ and $q = 2a$, hence $q/p = 2$

$$\int_0^{\infty} \frac{\exp(-a\tilde{r}^2) - \exp(-2a\tilde{r}^2)}{\tilde{r}^2} d(\tilde{r}^2) = \ln(2)$$

Then, $\overline{\Delta P}(\tilde{r} \rightarrow 0) = 2a\ln(2)$

Pressure equation for Rankine Vortex:

$$\overline{\Delta P}(\tilde{r}) = -2 + \tilde{r}^2 \quad \text{for } 0 < \tilde{r} \leq 1 \quad (3.3.14a)$$

$$\overline{\Delta P}(\tilde{r}) = -\frac{1}{\tilde{r}^2} \quad \text{for } 1 \leq \tilde{r} < \infty \quad (3.3.14b)$$

The radial pressure coefficient $\overline{\Delta P}(\tilde{r})$ as a function of \tilde{r} has shown some very interesting results in Figure 3.3.4. As it was expected, the radial pressure coefficient $\overline{\Delta P}(\tilde{r})$ drops drastically near or inside the core region (i.e. $\tilde{r} \rightarrow 0$). The dimensional analysis generalized the radial pressure regardless of the value of contraction ratio (R_E/R_O). In the figure, the solid line and dotted line represent Eq.(3.3.13) and Eq.(3.3.14) respectively. The two analytical radial pressure profiles agreed with the experimental data. It is important to note that the core radius is located at approximately half way between the maximum and minimum $\overline{\Delta P}$ for the case of the Burgers' vortex while it is exactly half way for Rankine vortex. This value is exactly equal to $(\overline{\Delta P}_{\max} + \overline{\Delta P}_{\min})/2 = (0 - 2)/2 = -1$. In another words, for $\tilde{r} = 1$ and, $\overline{\Delta P} = -1$ for Rankine vortex.

The other correlation which is going to be shown is the inlet total pressure coefficient $\widetilde{\Delta P}$ vs. β . Shakespeare and Levy's [112], Vatistas' [28] and the present tangential velocity component data have been utilized and they all correlate in the same way. This figure will be discussed in further detail in chapter 4.

Eq.(3.2.11) shows the dimensional relationship between the tangential velocity and \tilde{r} . It is an important one because it generalizes the tangential velocity component of almost all kinds of vortex flows. The confined vortex flow, cyclone, hurricane and etc. can now be correlated together by using Eq.(3.2.11). Figure 3.3.6 and 3.3.7 show the similarity of different sets of experimental results on concentrated vortices. The peak value is within 0.65 - 0.80. All the results are well correlated. The two figures show that the similarity relationship represents well with most of the concentrated vortices regardless of their method of production.

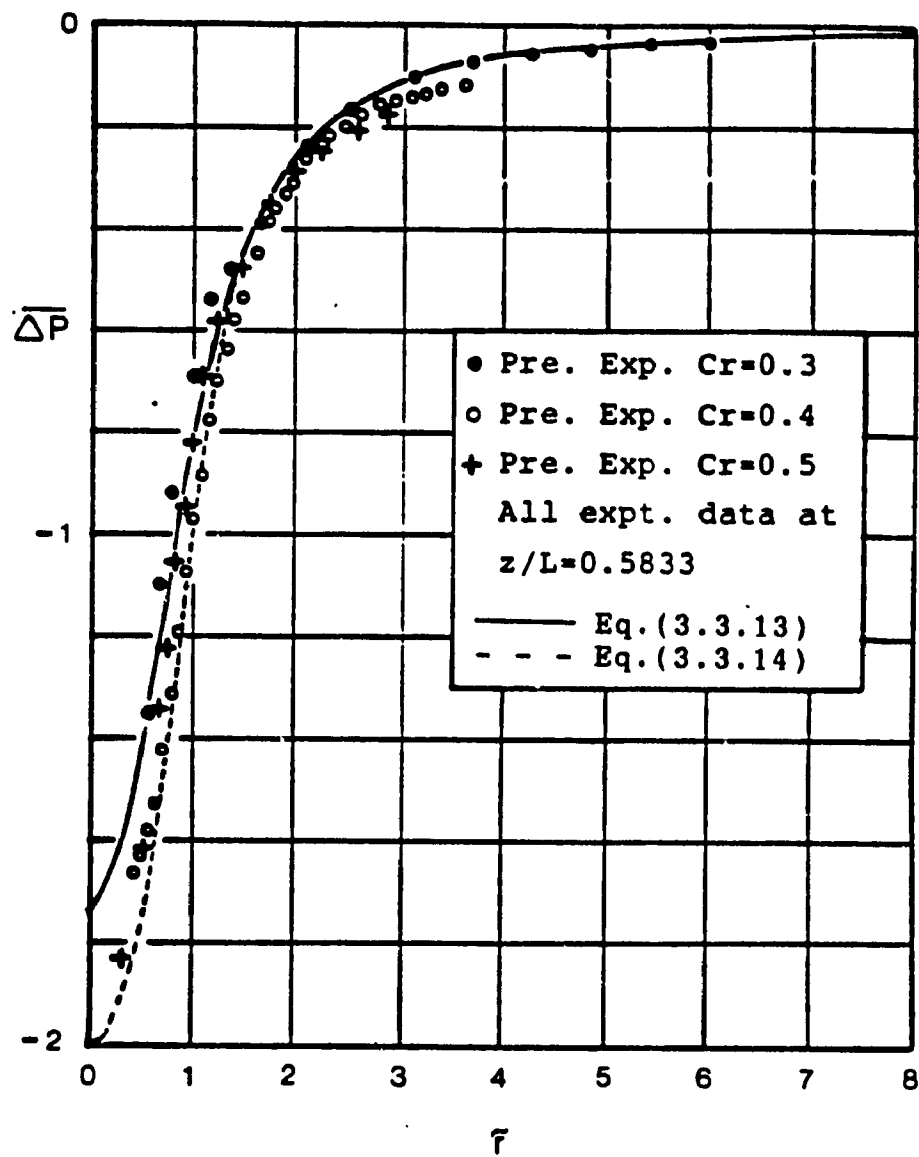


Figure 3.3.4 Nondimensional Radial Pressure $\overline{\Delta P}$ vs. \bar{r}

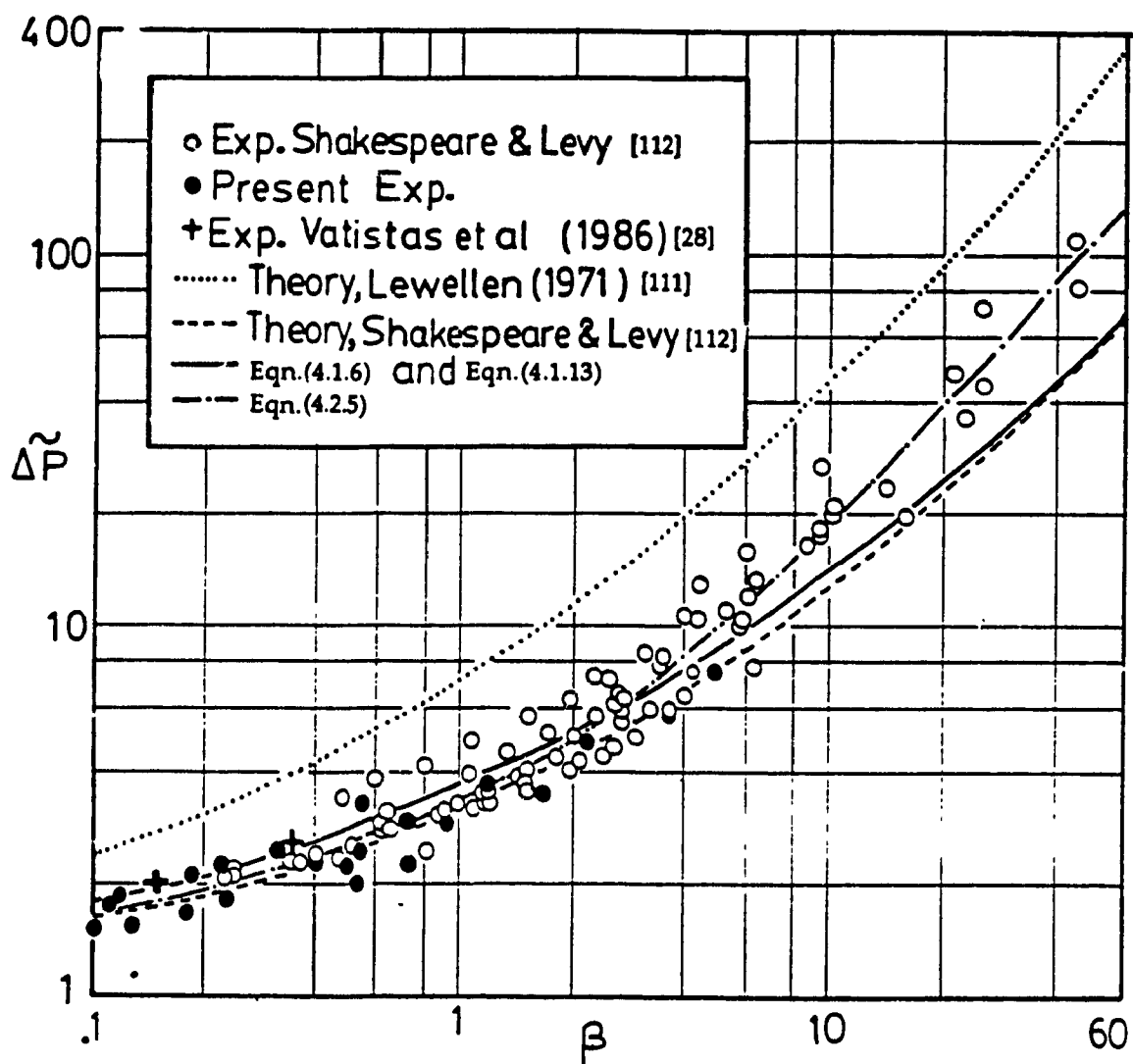


Figure 3.3.5 Nondimensional Total Pressure $\Delta\tilde{P}$ vs. β

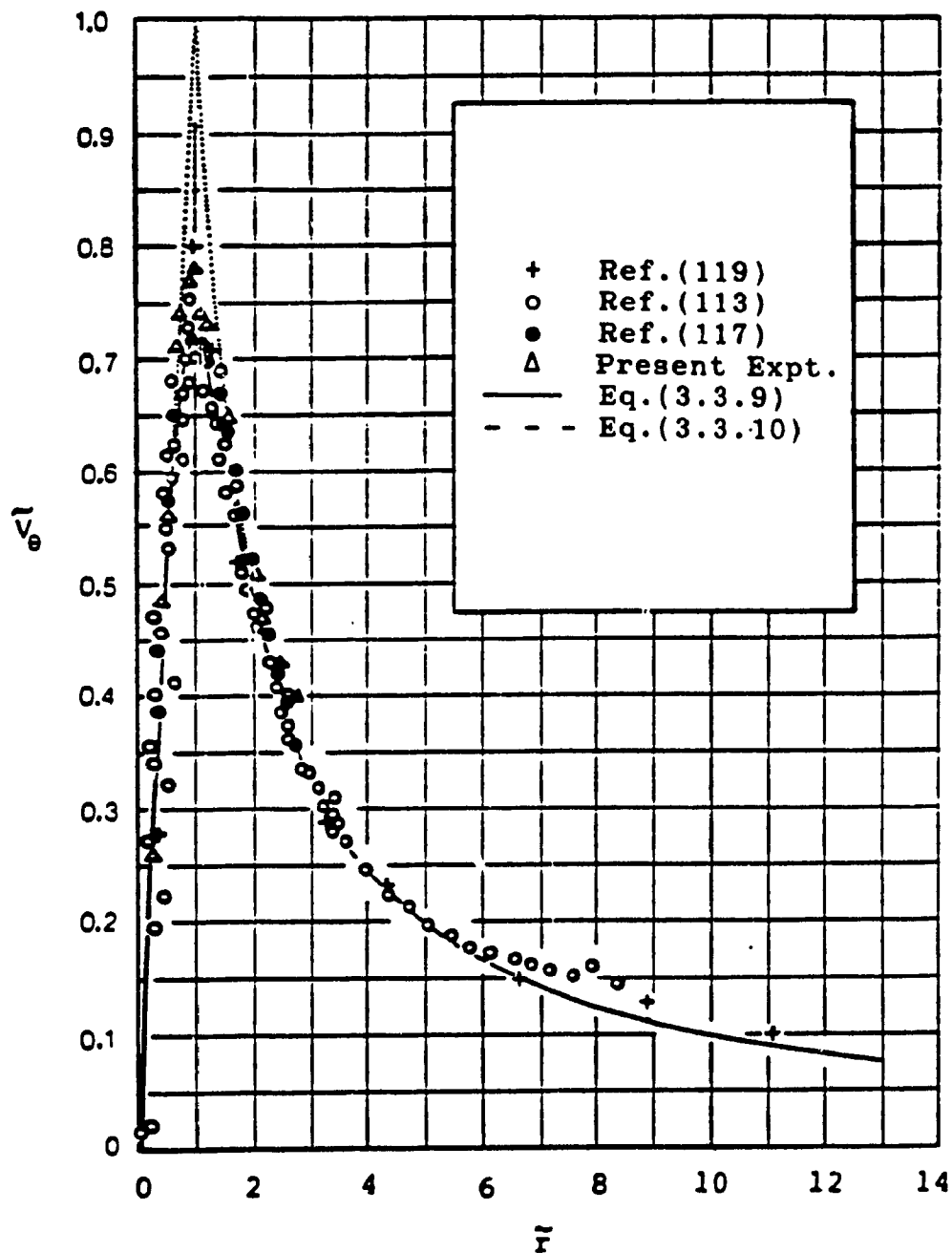


Figure 3.3.6 Nondimensional tangential velocity \tilde{V}_θ vs \tilde{r}
for concentrated vortices

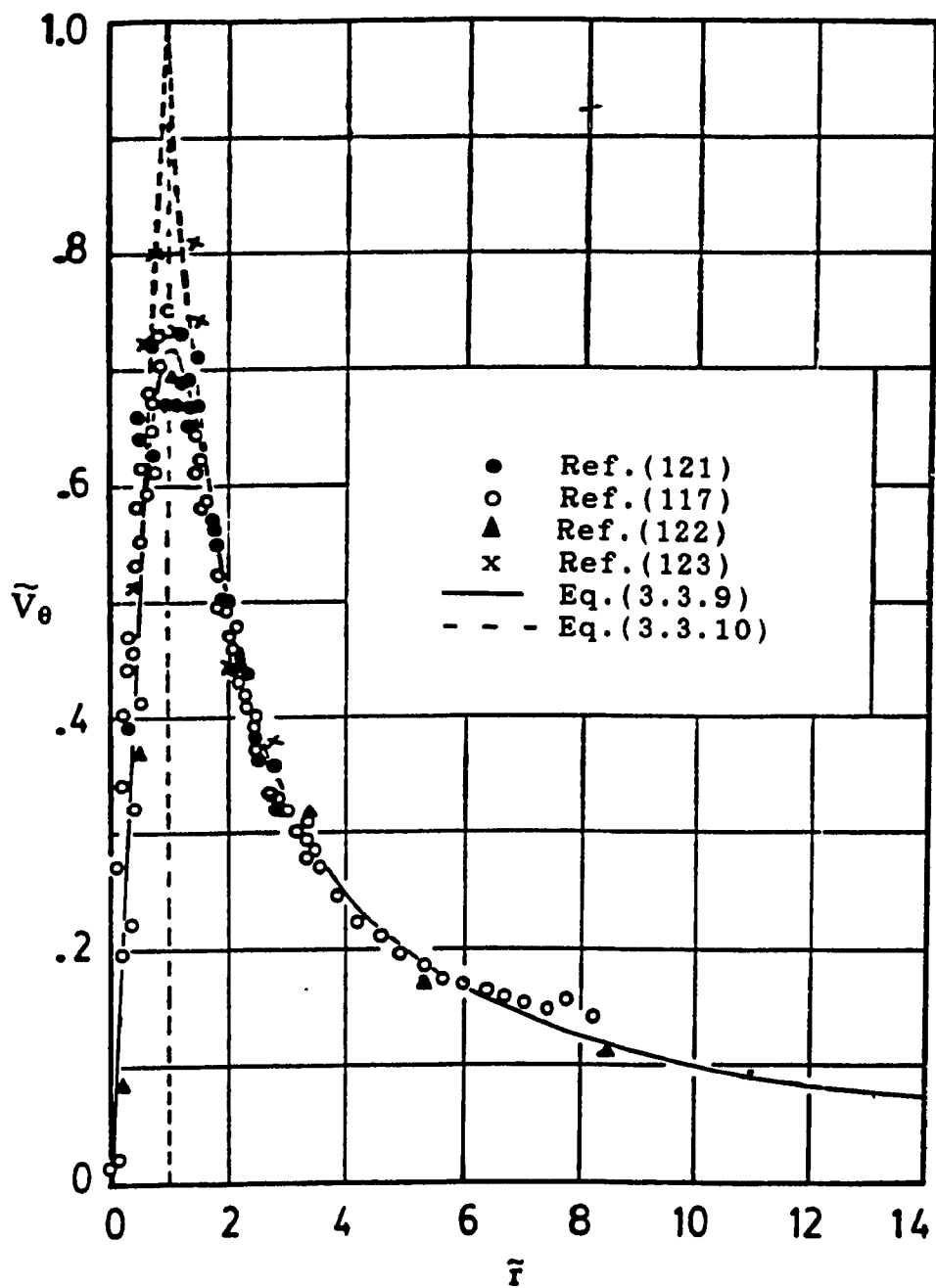


Figure 3.3.7 Nondimensional tangential velocity \tilde{V}_θ vs \tilde{r} for concentrated vortex.

CHAPTER 4

CORE SIZE AND STATIC PRESSURE DROP

This chapter concentrates on the core size and pressure drop across the vortex chamber. The normalized core radius is shown to be solely dependent on a dimensionless parameter which involves only the geometric quantities. The geometric quantities consist of the inlet area, the swirling angle and the exit radius. The pressure drop across the chamber has been the subject of several papers [28,109-112]. The most recent work by Vatistas et al [28] has shown the pressure drop to be strongly dependent on this dimensionless parameter. The following analysis was applied on vortex chambers with aspect ratios (length/diameter) between 1.0 - 3.0.

4.1 GOVERNING EQUATIONS FOR PRESSURE DROP AND CORE SIZE

Figure 4.1.1 shows the schematic of the confined vortex flow problem. The flow is considered to be steady, incompressible and the main flow region is inviscid. The main flow region ignores the core at the center and the boundary layer at the wall. The above assumptions have been used by Vatistas et al [28] in their confined vortex theoretical analysis. From their analysis [28] for the vortex chamber flows, it can lead to a pressure drop equation. The analysis stated that,

$$\left(\frac{P_{in}}{\rho} + \frac{1}{2}q_{in}^2\right)Q = 2\pi \int_{R_{CF}}^{R_E} \left[\frac{P_{amb}}{\rho} + \frac{1}{2}(V_{\theta}^2 + V_z^2)\right] V_z r dr$$

$$\left(\frac{P_{in}}{\rho} + \frac{1}{2}q_{in}^2\right)Q = \frac{\pi P_{amb} V_z (R_E^2 - R_{CF}^2)}{\rho} + \pi V_z \int_{R_{CF}}^{R_E} V_{\theta}^2 r dr + \frac{\pi V_z^3 (R_E^2 - R_{CF}^2)}{2}$$

$$\text{but } V_z = \frac{Q}{\pi(R_E^2 - R_{CF}^2)}$$

$$\left(\frac{P_{in}}{\rho} + \frac{1}{2}q_{in}^2\right)Q = \frac{P_{amb}Q}{\rho} + \frac{Q}{(R_E^2 - R_{CF}^2)} \int_{R_{CF}}^{R_E} V_{\theta}^2 r dr + \frac{Q^3}{2\pi^2(R_E^2 - R_{CF}^2)^2}$$

finally,

$$\frac{2\Delta P}{\rho} = \left[\frac{Q}{\pi R_E^2}\right]^2 \frac{1}{(1-X_{CF}^2)^2} + \frac{2}{R_E^2(1-X_{CF}^2)} \int_{R_{CF}}^{R_E} V_{\theta}^2(r) r dr - \left[\frac{Q}{A_{in}}\right]^2 \quad (4.1.1)$$

where, $\Delta P = P_{in} - P_{amb}$

$X_{CF} = R_{CF}/R_E$

R_{CF} = core radius at the exit

Q = volumetric flow rate

q_{in} = total inlet velocity

R_E = exit radius

Γ = inlet swirling strength

A_{in} = inlet area of the vortex jet

ρ = density of the air

V_z = average exit axial velocity component

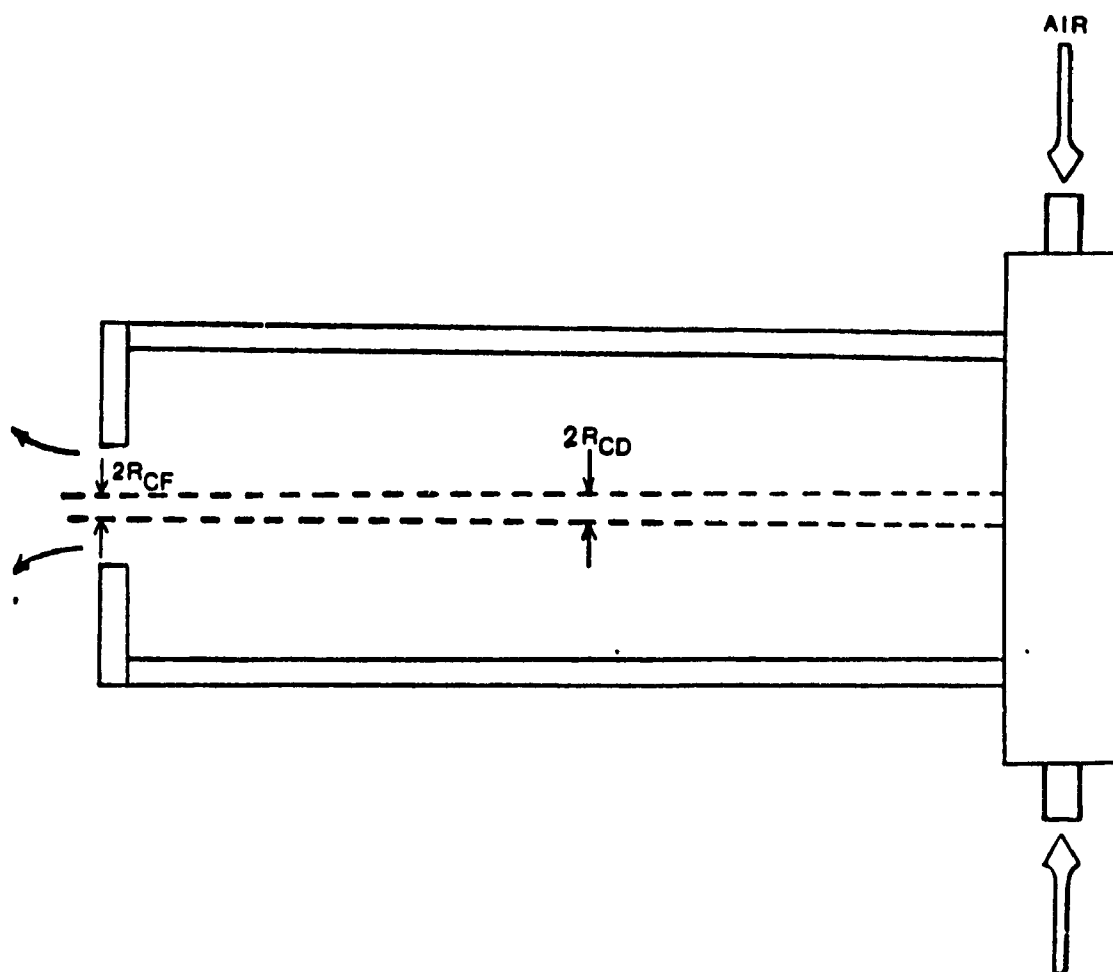


Figure 4.1.1 Schematic of the Physical Problem

V_θ = tangential velocity component

By minimizing ΔP in Eqn.(4.1.1) with respect to R_{CF} , that is

$$\frac{\partial \Delta P}{\partial R_{CF}} = 0 \quad (4.1.2)$$

the following equation is obtained,

$$\left[\frac{Q}{\pi R_E^2} \right]^2 \frac{4X_{CF}}{R_E (1 - X_{CF}^2)^3} + \frac{4X_{CF}}{R_E^3 (1 - X_{CF}^2)^2} \int_{R_{CF}}^{R_E} V_\theta^2(r) r \, dr - \frac{2R_{CF} V_\theta^2(R_{CF})}{R_E^2 (1 - X_{CF}^2)} = 0$$

and the final equation is,

$$\left[\frac{2Q}{\pi R_E^2} \right]^2 \frac{1}{(1 - X_{CF}^2)^3} + \frac{4}{R_E^2 (1 - X_{CF}^2)^2} \int_{R_{CF}}^{R_E} V_\theta^2(r) r \, dr - \frac{2X_{CF}^2 V_\theta^2(R_{CF})}{(1 - X_{CF}^2)} = 0 \quad (4.1.3)$$

From Vatistas et al's work [28], the pressure drop equation was derived by assuming a Rankine tangential velocity profile or by substituting $V_\theta(r)$ as $\Gamma/2\pi r$ into Eqn.(4.1.1) above. Then the pressure drop equation will be,

$$\frac{2\Delta P}{\rho} = \left[\frac{Q}{\pi R_E^2} \right]^2 \frac{1}{(1 - X_{CF}^2)^2} + \frac{1}{2} \left[\frac{\Gamma}{\pi R_E} \right]^2 \frac{\ln(1/X_{CF})}{1 - X_{CF}^2} - \left[\frac{Q}{A_{in}} \right]^2 \quad (4.1.4)$$

By minimizing ΔP in Eqn.(4.1.4) with respect to X_{CF} , or

$$\frac{\partial \Delta P}{\partial X_{CF}} = 0 \quad (4.1.5)$$

the following equation is obtained,

$$X_{CF}^4(2\ln X_{CF} - 1) + 2X_{CF}^2((\beta^2 + 1) - \ln X_{CF}) - 1 = 0 \quad (4.1.6)$$

where $\beta = \left[\frac{A_{in}/A_o}{(R_E/R_O) \cos \phi} \right]$

$$A_o = \pi R_O^2$$

R_O = radius of the chamber

ϕ = swirling angle (angle between the total inlet velocity and the tangent)

The same equation, Eqn.(4.1.6) will be obtained by simply substituting V_θ as $\Gamma/2\pi r$ in Eqn.(4.1.3). Therefore, Eqns.(4.1.1) and (4.1.3) are the derived expression for the pressure drop and core size equations as long as the tangential velocity profile is a function of radius r . Eqn.(4.11) was derived from energy balanced and flow continuity for a control volume. Eqn.(4.1.3) was obtained by the principle of minimum pressure drop across the chamber. Eqn.(4.1.6) represents a similarity relationship between two dimensionless parameters, the exit core radius X_{CF} and β . Figure 4.1.2 shows how the core size varies with β^2 . Taking into the consideration of some of the difficulties associated with the experimental determination of X_{CF} , the results obtained from Eqn.(4.1.6) are in good agreement with the observations. In Table (4.1.1), the core size equations from [111] and [112] are listed. From Figure 4.1.2, both of these equations are shown to overestimate the core.

There are several papers which dealt with the pressure drop across vortex chambers. Tager [109] normalized the pressure difference ΔP by

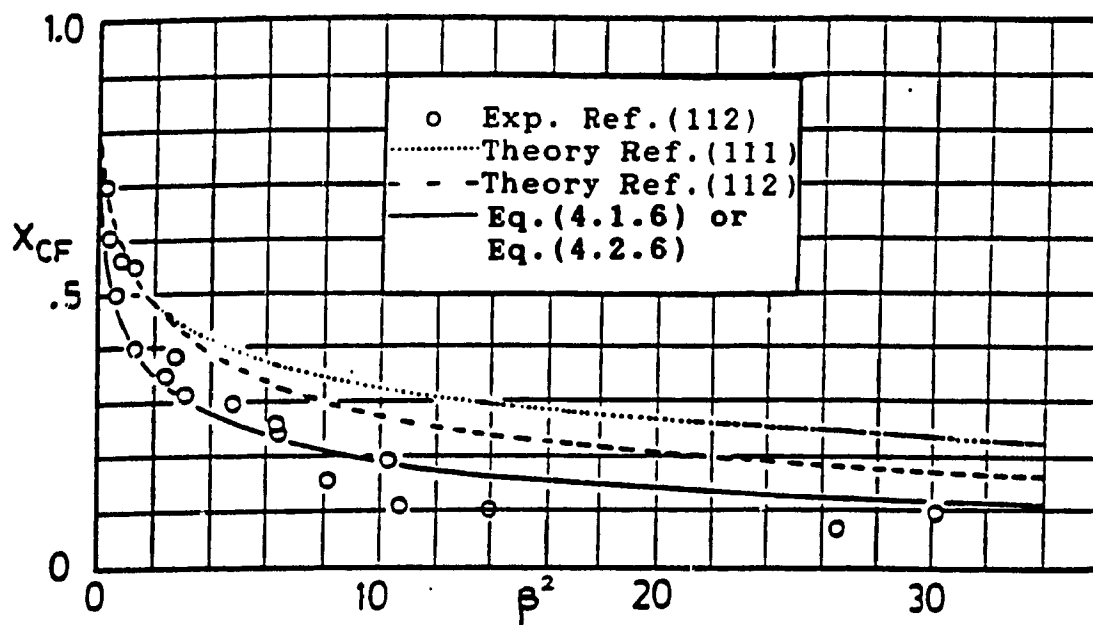


Figure 4.1.2 Nondimensional Core Size X_{CF} at the Exit vs.
the Parameter β

Table (4.1.1): Core Size Equations

Source	Equation for X_{CF}
Lewellen [111]	$X_{CF}^6 - 3X_{CF}^4 + 2\beta^2 X_{CF}^3 + 3X_{CF}^2 - 1 = 0$
Shakespear [112]	$X_{CF}^2 + \beta^{2/3} X_{CF}^{1/3} - 1 = 0$

Table (4.1.2): Pressure Drop Equations

Source	Equation for ΔP
Lewellen [111]	$(X_{CF}^2 + 1)/2X_{CF}^4$
Shakespear [112]	$1/X_{CF}^2$

Table (4.2.1): Values of the Coefficients in Eqn.(4.2.4)

a_0	a_1	a_2	a_3	a_4	a_5	a_6	a_7
8.52	0.45	0.31	0.14	-0.21	-0.01	0.1	-0.04

Table (4.2.2): Values of the Coefficients in Eqn.(4.2.5)

b_0	b_1	b_2	b_3	b_4	b_5
3.1	-13.34	24.08	-8.46	-39.76	79.83
b_6	b_7	b_8	b_9	b_{10}	
-148.3	519.1	-1228.0	1368.0	562.5	

dividing it with that when $R_E/R_O = 0.45$. Based on his experimental results, he proposed the following empirical equation,

$$\frac{\Delta P}{\Delta P_{0.45}} = \frac{0.9}{R_E/R_O} - 1 \quad (4.1.7)$$

For the range of contraction ratios R_E/R_O (Cr) within 0.3 - 0.7, which is of practical interest, Tager has shown that Eqn.(4.1.7) fairly approximates his experimental results. A similar expression can also be obtained using the empirical equation of Troyanking and Baluev [110],

$$\frac{\Delta P}{\Delta P_{0.45}} = \frac{2.1}{(1 + R_E/R_O)^2} \quad (4.1.8)$$

From Eqn.(4.1.4), it can be showed that,

$$\left[\frac{2\Delta P}{\rho q_{in}^2} + 1 \right] = \left[\frac{A_{in}/A_o}{(R_E/R_O)^2} \right]^2 \frac{1}{(1 - X_{CF}^2)^2} - \frac{2 \cos^2 \phi \ln(X_{CF})}{(R_E/R_O)^2 (1 - X_{CF}^2)} \quad (4.1.9)$$

Then,

$$\frac{\Delta P}{\Delta P_{0.45}} = \frac{\left[a_1/(R_E/R_O)^2 \right]^2 \left[1 + a_2/(R_E/R_O)^2 \right]}{24.386 a_1^2 - (1 + 4.938 a_2)} \quad (4.1.10)$$

$$\text{where, } a_1 = \frac{A_{in}/A_o}{1 - X_{CF}^2}, \quad a_2 = \frac{2 \cos^2 \phi \ln(X_{CF})}{1 - X_{CF}^2}$$

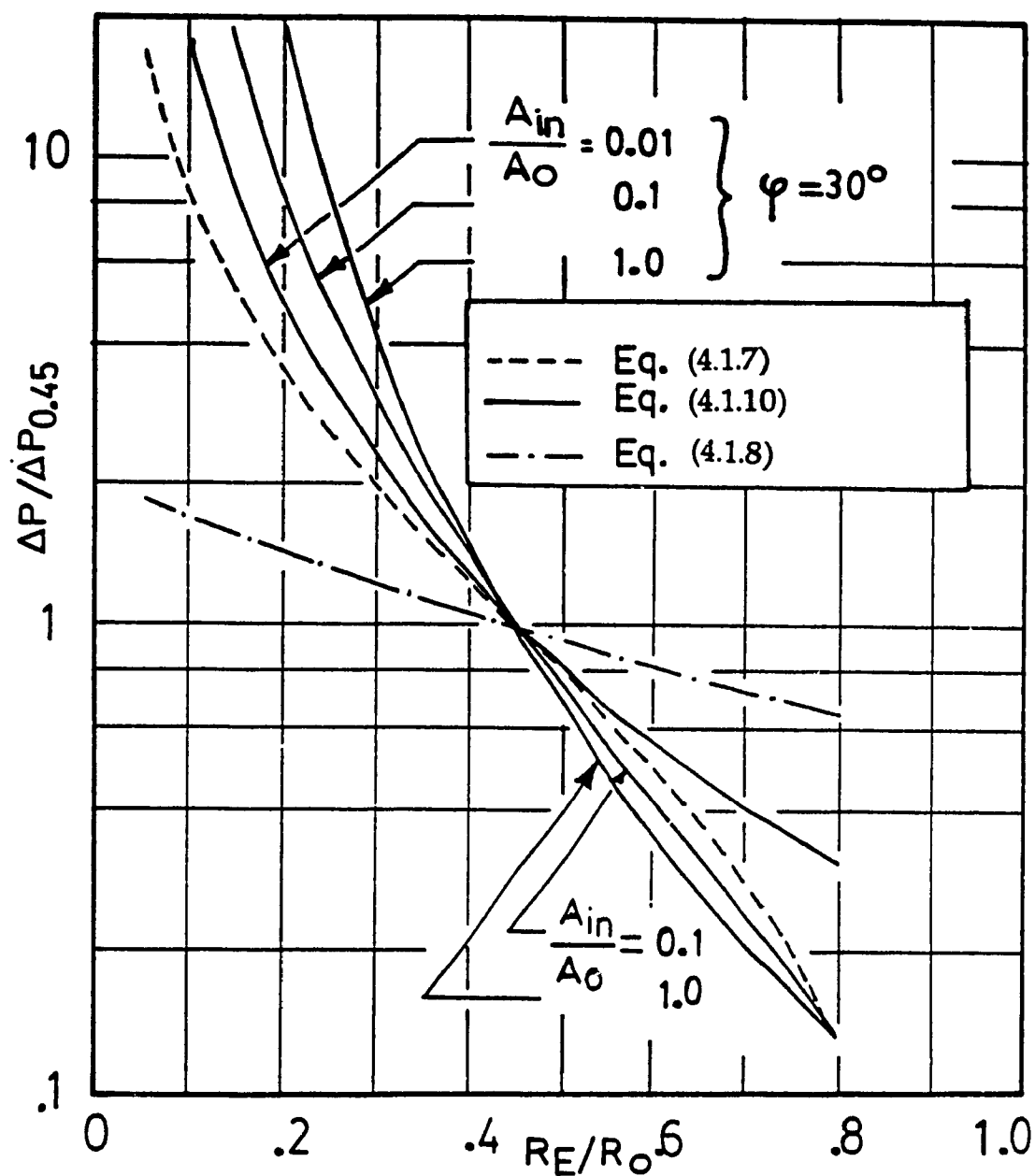


Figure 4.1.3 Variation of the Normalized Pressure vs. the Contraction Ratio with Different Area Ratios

A comparison among Eqns.(4.1.7), (4.1.8), and (4.1.10) shows the first and second depend only on the contraction ratio while the third to be also a function of A_{in}/A_o and ϕ . In Figure 4.1.3 the results obtained from Eqn.(4.1.7) and Eqn.(4.1.8) are shown together with those calculated by Eqn.(4.1.10). It is clear that Eqn.(4.1.8) disagrees considerably with the other two. In the range of $R_E/R_O = 0.3 - 0.8$ the difference between Eqn.(4.1.7) and Eqn.(4.1.10) is not as significant as it is in the case for small contraction ratios and large area ratios. In Figure 4.1.4, the present and Tager's [109] experimental results are compared with the calculations made using the above mentioned equations. Eqn.(4.1.8) is in disagreement with the experimental data. The discrepancy of Eqn.(4.1.7) with the present experimental results is large for small contraction ratios. Unfortunately Tager does not give any information concerning the inlet conditions (A_{in}/A_o and ϕ) therefore Eqn.(4.1.10) cannot draw any concrete conclusion with Tager's experimental data.

$$\text{since } \widetilde{\Delta P} = \left[\frac{2\Delta P}{\rho q_{in}^2} + 1 \right] \left[\frac{R_E/R_O}{\cos\phi} \right]^2,$$

then Eqn.(4.1.9) can be written as,

$$\widetilde{\Delta P} = \frac{\beta^2}{(1 - X_{CF}^2)^2} - \frac{2 \ln(X_{CF})}{1 - X_{CF}^2} \quad (4.1.11)$$

However, from Eq.(4.1.6) β can be written in terms of X_{CF} ,

$$\beta^2 = \frac{1 - X_{CF}^4(2\ln(X_{CF}) - 1)}{2X_{CF}^2} + \ln(X_{CF}) - 1 \quad (4.1.12)$$

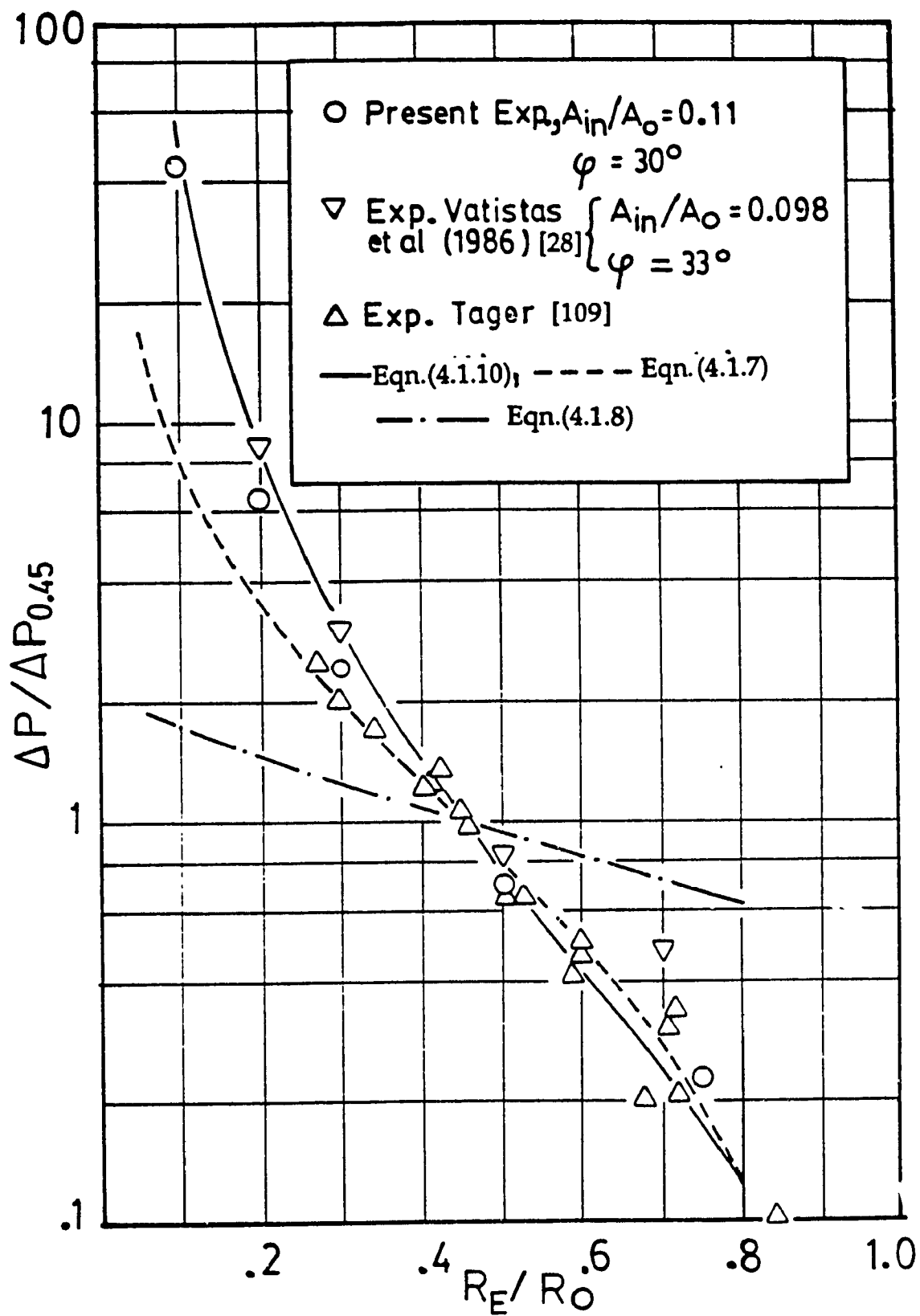


Figure 4.1.4 The Normalized Pressure Difference as a Function of the Contraction Ratio

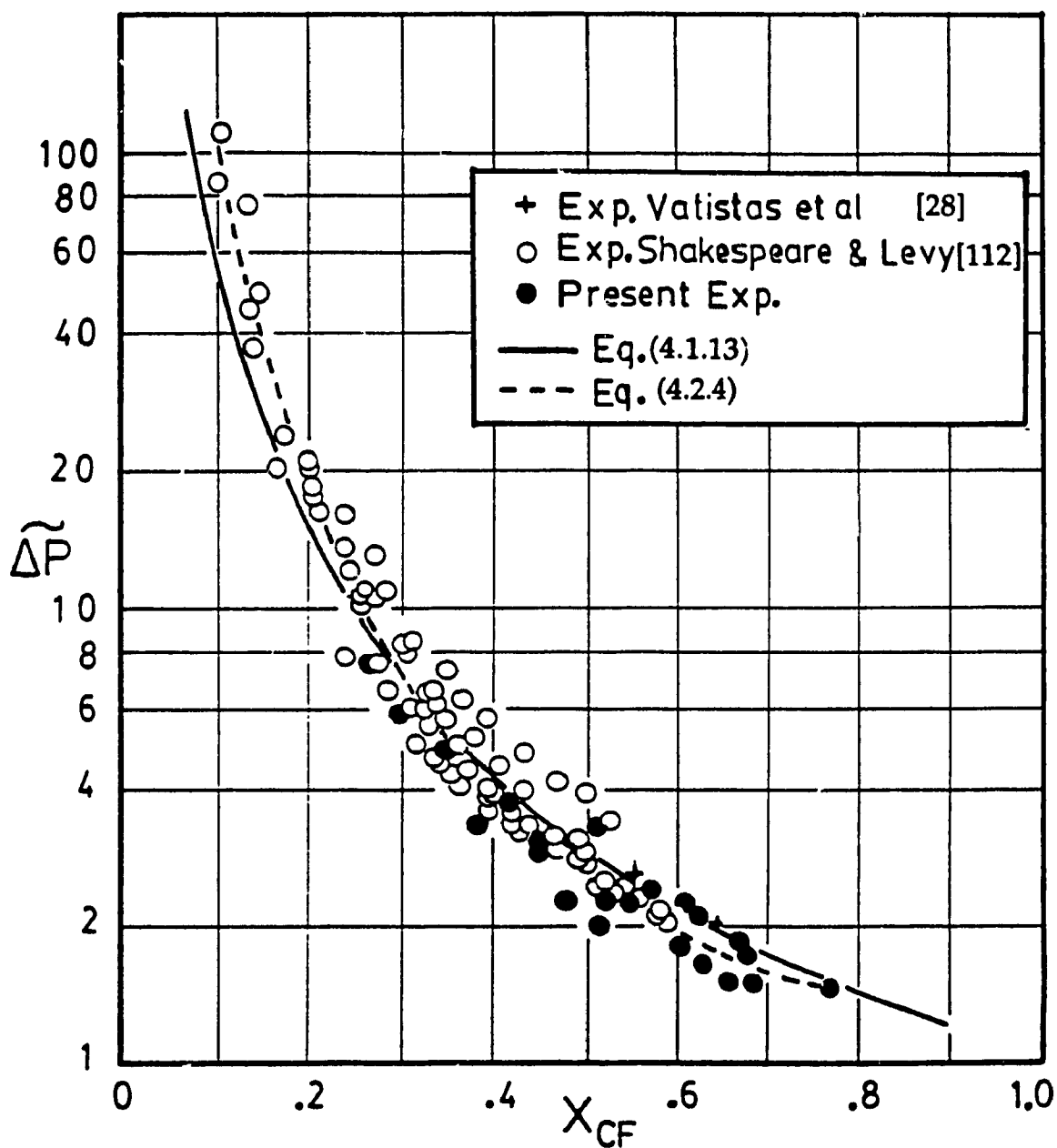


Figure 4.1.5 Dimensionless Pressure Difference as a Function of the Exit Core

By substituting Eqn.(4.1.12) into Eqn.(4.1.11),

$$\widetilde{\Delta P} = \frac{1 - X_{CF}^2 (2 \ln(X_{CF}) + 1)}{2 X_{CF}^2 (1 - X_{CF}^2)} \quad (4.1.13)$$

Equation (4.1.13) shows that the dimensionless pressure drop is a function of the core at the exit. This conclusion is established in Figure 4.1.5 where $\widetilde{\Delta P}$ is seen to collapse into an almost single curve if it is plotted as a function of X_{CF} . For contraction ratios greater than 0.3, Eqn.(4.1.13) correlates well with the experimental data. Similar expressions to Eqn.(4.1.13) have been derived using the theories of Refs.[111] and [112]. These are given in Table (4.1.2).

4.2 THE LEAST SQUARES METHOD FOR THE EXPERIMENTAL DATA

The following section reveals the least squares method (LSM) to best fit the experimental data. From Eqn.(4.1.13), $\widetilde{\Delta P}$ is a function of X_{CF} , or

$$\widetilde{\Delta P} = f(X_{CF}) \quad (4.2.1)$$

However, X_{CF} is a function of β , or

$$X_{CF} = g(\beta) \quad (4.2.2)$$

Therefore, $\widetilde{\Delta P}$ is a function of β , or

$$\widetilde{\Delta P} = h(\beta) \quad (4.2.3)$$

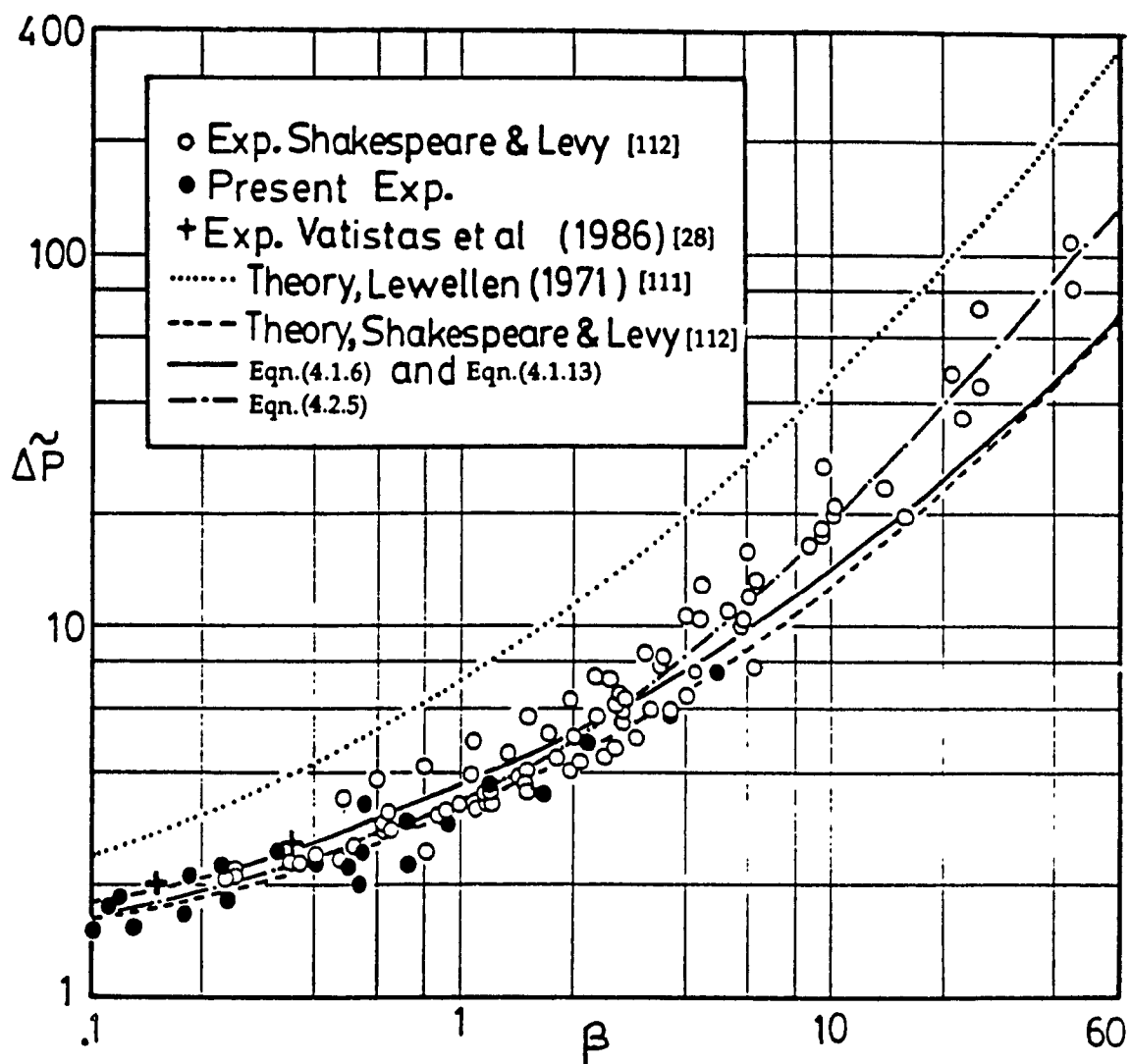


Figure 4.2.1 Dimensionless Pressure Difference vs.
the Geometrical Parameter β

Hence, Eqn.(4.2.3) should also represent a similarity relationship of $\widetilde{\Delta P}$ with the dimensionless parameter β . Based on that, $\widetilde{\Delta P}$ is plotted versus β in Figure 4.2.1 and as it can be seen that the similarity relationship suggested by the above equation is a reasonable one. For values of $\beta < 3$ the present theoretical results and the results of Reference [112] agree well with the experiment. However, the theory presented in Reference [111] is seen to have greatly overestimated the pressure drop. For $\beta > 3$, there is a noticeable difference between the predicted and actual values of the pressure.

However, it is difficult to solve $\widetilde{\Delta P}$ in terms of β analytically. The least squares method (LSM) is employed to best fit the experimental data. Eqns.(4.2.1) and (4.2.3) can be written as,

$$\log_{10} \widetilde{\Delta P} = \sum_{i=0}^n a_i X_{CF}^i \quad (4.2.4)$$

and

$$\log_{10} \widetilde{\Delta P} = \sum_{r=0}^m b_r (\log_{10} \beta)^r \quad (4.2.5)$$

From Eqns.(4.2.4) and (4.2.5) , the following can be obtained,

$$\sum_{i=0}^n a_i X_{CF}^i - \sum_{r=0}^m b_r (\log_{10} \beta)^r = 0 \quad (4.2.6)$$

Equation (4.2.6) represents a general equation for the core radius. A tenth degree polynomial ($m=10$), with b_r 's given in Table (4.2.2), was found to fit well with the experimental points of Figure 4.2.1. To completely define

Eq.(4.2.6), the values of a_i coefficients must be found. This is achieved using the following iterative method:

- (1) calculate the first set assumed X_{CF} values for each experimental point $\widetilde{\Delta P}$ in Figure 4.1.5 using Eqn.(4.1.6).
- (2) fit a polynomial by using the LSM to the experimental data $\widetilde{\Delta P}$ and the assumed X_{CF} values.
- (3) with the calculated values of a_i 's in step (2), solve Eqn.(4.2.6) to determine the new values of X_{CF} associated by each experimental point.
- (4) check whether the calculated values of X_{CF} are closed to the assumed X_{CF} values.
- (5) if yes, then stop the iteration, otherwise use the calculated X_{CF} values to repeat the whole procedure from step (2).

The above iterative procedure is valid for experiment which X_{CF} values are not measured. If experimental X_{CF} data are available, then a_i coefficients can be directly calculated from Figure 4.1.5.

Six iterations were more than sufficient to obtain the required results. The polynomial obtained is of order 7 ($n=7$) and the coefficients a_i 's are given in Table (4.2.1). It can be seen that X_{CF} values calculated using Eqns.(4.1.6) and (4.2.6) in Figure 4.1.2 are represented by a single curve. The latter is due to the fact that they differ only after the third decimal place.

A similarity relationship for the pressure drop across a vortex chamber has been found to exist. The pressure drop has been shown to depend solely on the single dimensionless number β . For $\beta < 3.0$, all but one of the

theoretically derived equations for the pressure drop can predict reality within a reasonable accuracy. The empirical formula obtained using the least square method can precisely predict the pressure drop in a wider range of design conditions.

CHAPTER 5

EXPERIMENTAL RESULTS OF CONFINED VORTEX FLOW

As it was mentioned in chapter 2, three sets of experiments have been completed. The first set, the visualization experiments, produced qualitative results to illustrate some of the important characteristics of a confined vortex. The second and third sets investigated the internal structure of a confined vortex quantitatively. In these experiments, measurements had been carried out in order to understand the flow characteristics of a confined vortex. The deduced mean velocity components and static pressure distributions are examined in later sections.

These experiments have been conducted in a vortex chamber with an aspect ratio of 2.59. The swirling angle is 40° measured from the tangent to the inlet of the vortex generating block. Three different contraction ratio (R_E/R_O), 0.3, 0.4 and 0.5, have been used. Two volumetric flow rates, $0.0236\text{m}^3/\text{s}$ and $0.03304\text{m}^3/\text{s}$ at standard pressure 101.4 KN/m^2 and temperature 273°K (50 and 70 SCFM), were utilized for this experiment. The inlet area of the vortex jet was measured to be $22.77 \times 10^{-4}\text{ m}^2$. The diameter of the chamber is 0.1397m (5.5 inches). The air was maintained at around 22°C .

As it is mentioned in chapter 2, a computer program has been developed to correct all the measured values due to the contribution of the strong centrifugal effect of the vortex. The departure between the measured values to the corrected ones will be compared graphically. However, unless

otherwise specified, all the tabulated experimental results are the corrected values.

The third project was similar to the second one except a conical plug was placed at the exit of the chamber. Measurements of velocity and pressure had been conducted to compare the results with the second project.

5.1 RESULTS OF THE VISUALIZATION EXPERIMENT

The purpose of the visualization experiment is to demonstrate the flow properties of a confined vortex in a qualitative manner.

The experimental set up was similar to the one which was used to measure the velocity and pressure profile. The working fluid was water and food color dye was utilized to visualize part of the flow characteristics of the vortex. The dye was injected through the inlet of the vortex generating block so that it could stay inside the main stream of the vortex. The injection of the dye and the overall view of the apparatus are shown in Photo 5.1.1 and 5.1.2. The outlet of the vortex chamber was connected to a large storage tank which was always maintained at a constant level of water.

Two sets of experiments were conducted in terms of the high ($Re \approx 1.5 \times 10^5$, Reynolds number Re which is defined as $Q/(R_O v)$) and low ($Re \approx 4.5 \times 10^4$) flow rate respectively. Experimental results showed that the core of the vortex remains approximately the same diameter throughout the chamber especially for the high flow rate. For the low flow rate ($Re \approx 4.5 \times 10^4$), the core does not change much in terms of the size through out the chamber.



Photo 5.1.1 An Overall View of the Visualization Experimental Set-up

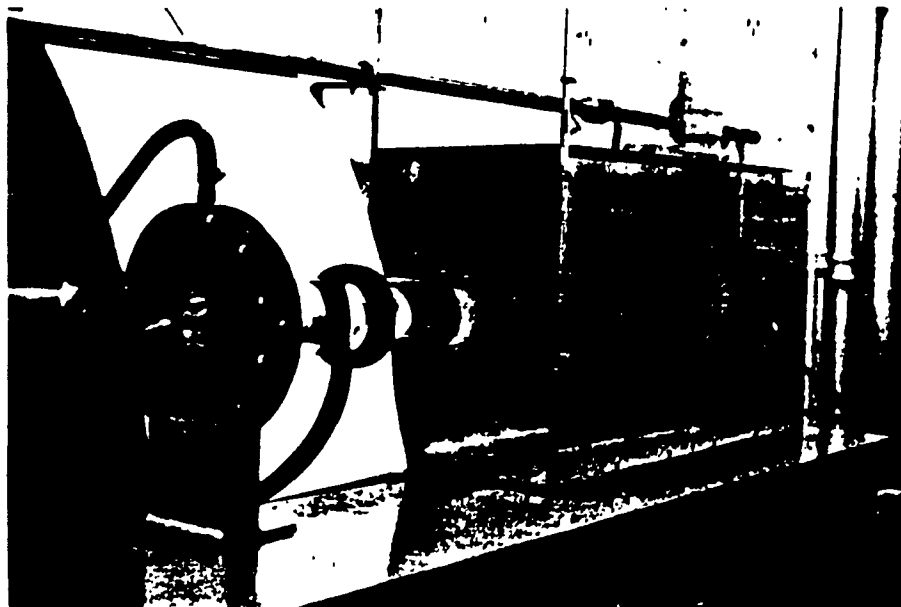


Photo 5.1.2 Another View of the Visualization Experimental Set-up

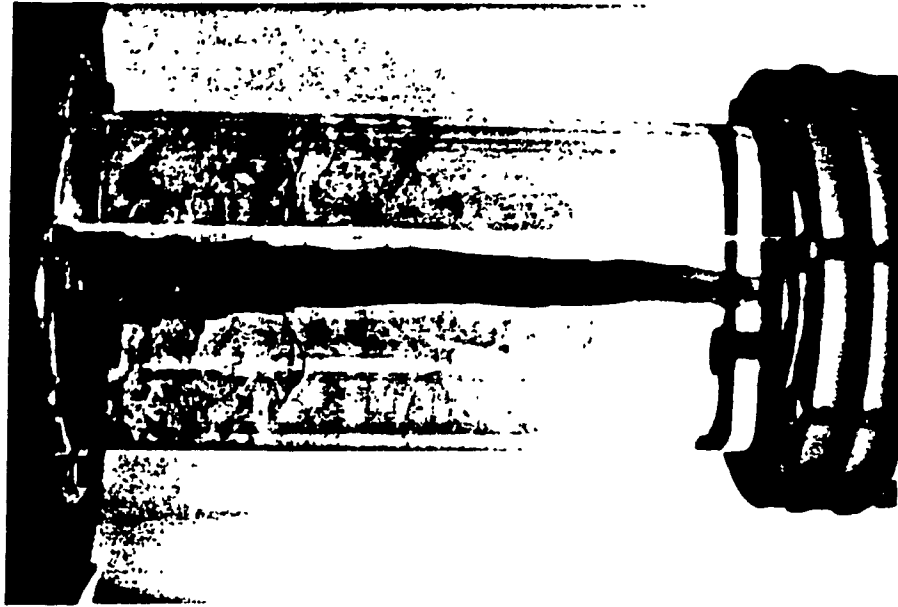


Photo 5.1.3 The Development of the Core Inside the
Vortex for Low Flow Rate ($Re \approx 4.5 \times 10^4$)

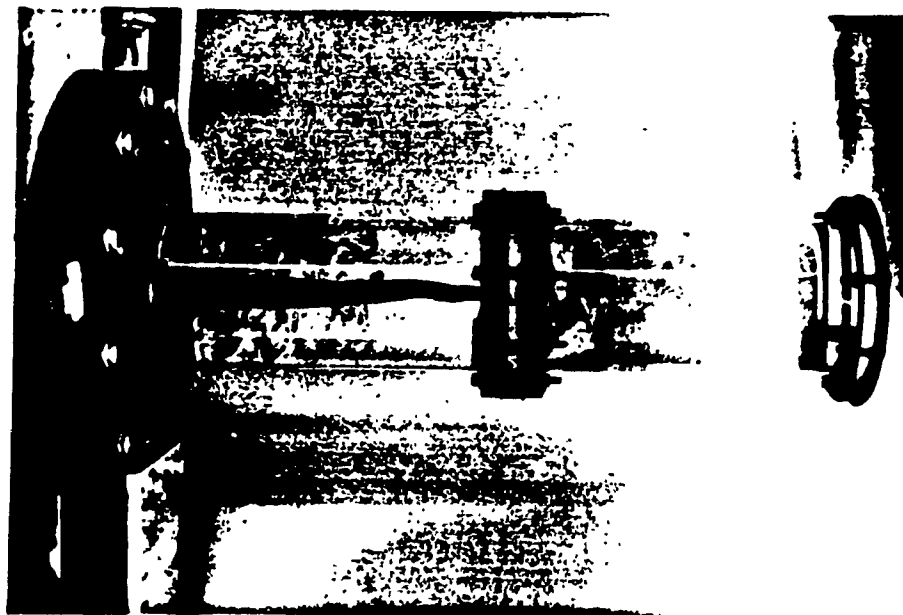


Photo 5.1.4 Vortex Breakdown in the Downstream for
the Low Flow Rate ($Re \approx 4.5 \times 10^4$)

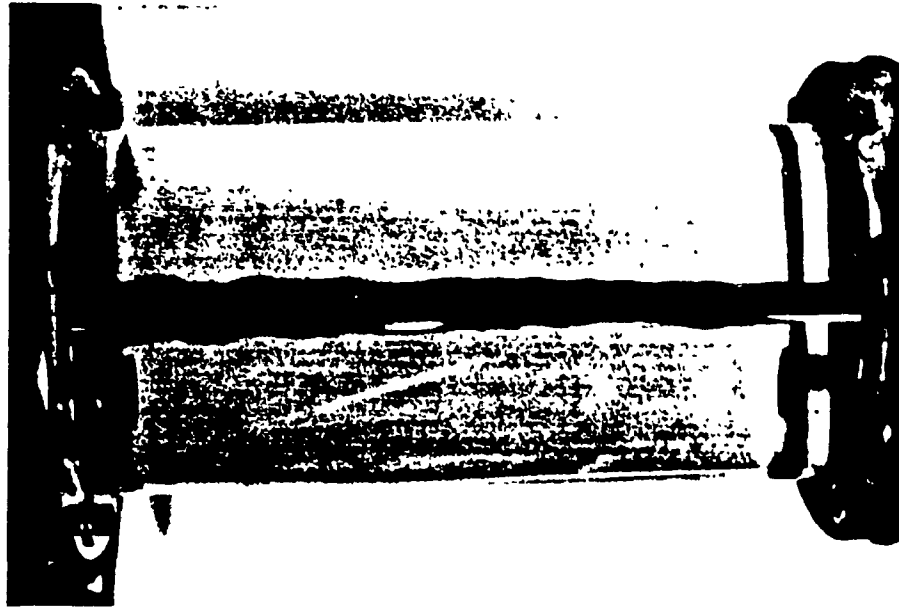


Photo 5.1.5 The Development of the Core Inside
the Vortex for a High Flow Rate ($Re \approx 1.5 \times 10^5$)

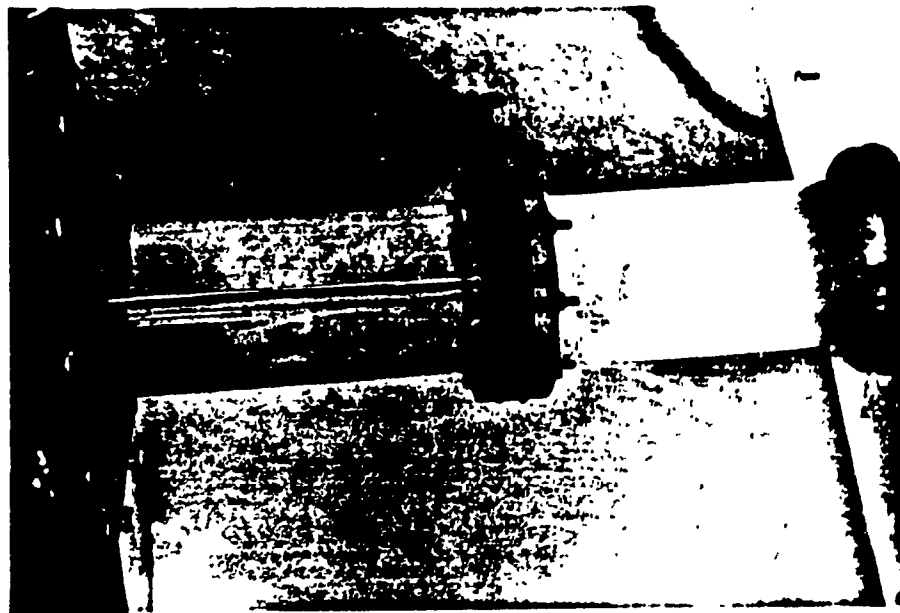


Photo 5.1.6 The Development of a Reverse Flow and Vortex Breakdown
Downstream for a Higher Flow Rate ($Re \approx 3.0 \times 10^5$)

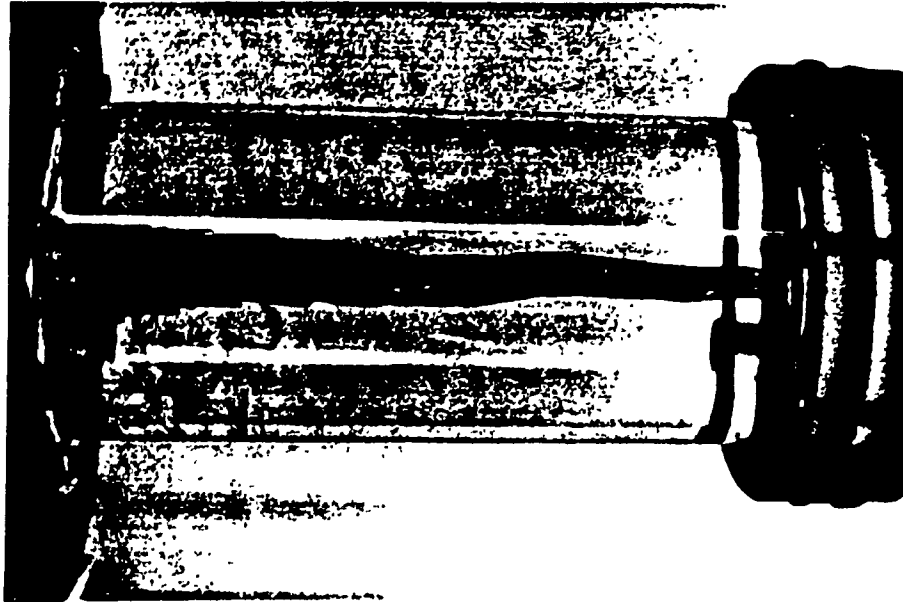


Photo 5.1.7 Intense Oscillation along the Core for a
Low Flow Rate ($Re \approx 4.5 \times 10^4$)

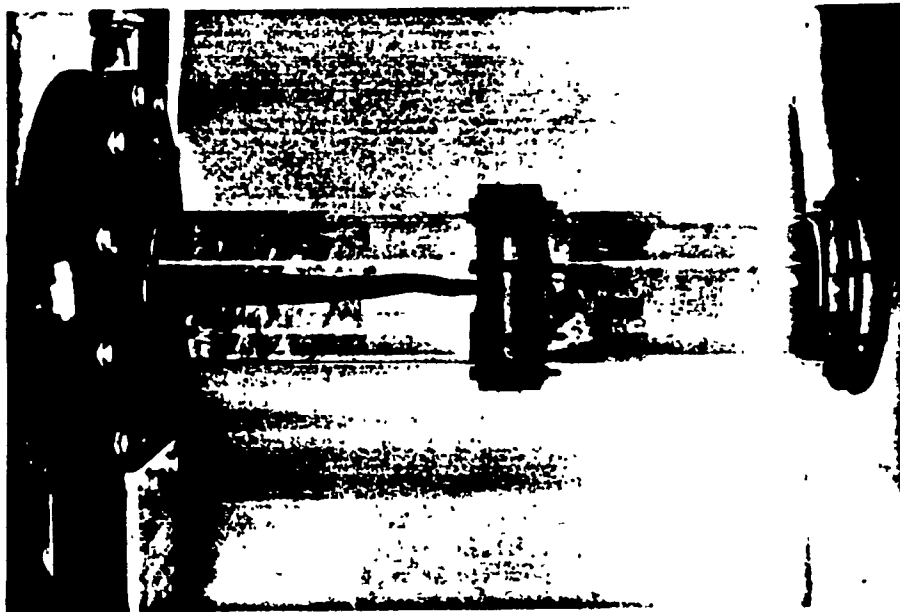


Photo.(5.1.8) Another View of the Core Oscillation

However, the vortex will breakdown in the downstream due to the lack of swirl. These phenomena are shown in Photo 5.1.3 and 5.1.4. If the flow rate is increased ($Re \approx 1.5 \times 10^5$), the core will maintain the same size from upstream to downstream. Photo 5.1.5 illustrates the constant size of the core inside a vortex. For a very high flow rate ($Re \approx 3.0 \times 10^5$), a tremendous amount of reverse flow was occurred at the downstream region. This shows that the core is usually a low pressure area relative to other regions. The reverse flow phenomenon is illustrated in Photo 5.1.6. Besides all those phenomena, a wavy motion of the core was noticed when the flow rate is relatively low ($Re \approx 4.5 \times 10^4$). This motion, which has been mentioned in chapter two, is called the oscillation of the center core. Photo 5.1.7 and 5.1.8 clearly caught the core in oscillation mode.

5.2 VELOCITY PROFILE AND STATIC PRESSURE PROFILE INSIDE THE VORTEX CHAMBER

There are three categories for the velocity component: the tangential velocity, V_θ , the radial velocity, V_r , and the axial velocity, V_z . The dominant velocity component through out the flowfield is the tangential velocity. The experimental flowfield was found to be similar to a free-force vortex pattern. This implies that the tangential velocity increases radially in a linear manner from the center to a local maximum and then it decreases slowly and smoothly towards the wall region. The radial position where the maximum tangential velocity occurs is defined as the size of the core for a certain axial location. The axial and radial velocity components also show some special characteristics from the experimental results.

a) TANGENTIAL VELOCITY

Three tangential velocity profiles were measured from different contraction ratios ($R_E/R_O = 0.3, 0.4$ and 0.5) and are shown in Figure 5.2.1. As the figure has indicated, the magnitude of the normalized tangential velocity from the smallest contraction ratio is the highest and vice versa. The core size increases as the exit radius gets bigger. The approximate value of the normalized core size (R_{CD}/R_E) for the respective contraction ratio are listed in Table 5.2.1.

Table 5.2.1 Normalized Core Size for Respective Contraction Ratio

Contraction Ratio (R_E/R_O)	0.3	0.4	0.5
Normalized Core Size (R_{CD}/R_E)	0.158	0.248	0.333

From Figure 5.2.1, a decrease of 20% in exit radius (from $Cr = 0.5$ to 0.4) will lead to the increase of the maximum tangential velocity by almost 50% (from about 2 to 3). From $Cr = 0.5$ to 0.4 , it is a reduction of 36% in terms of area changes. A further decrease of the exit radius (from $Cr = 0.5$ to 0.3), implies to a reduction of 40% in exit radius and is equivalent to a decrease of about 64% in exit area. The maximum tangential velocity increases drastically by about 100% (from about 2 to 4). The overall increase of the tangential velocity due to the reduction of exit radius is occurred predominantly near the core region only. For $r/R_O > 0.4$, $V_\theta/V_{\theta in}$ is almost identical for all three profiles.

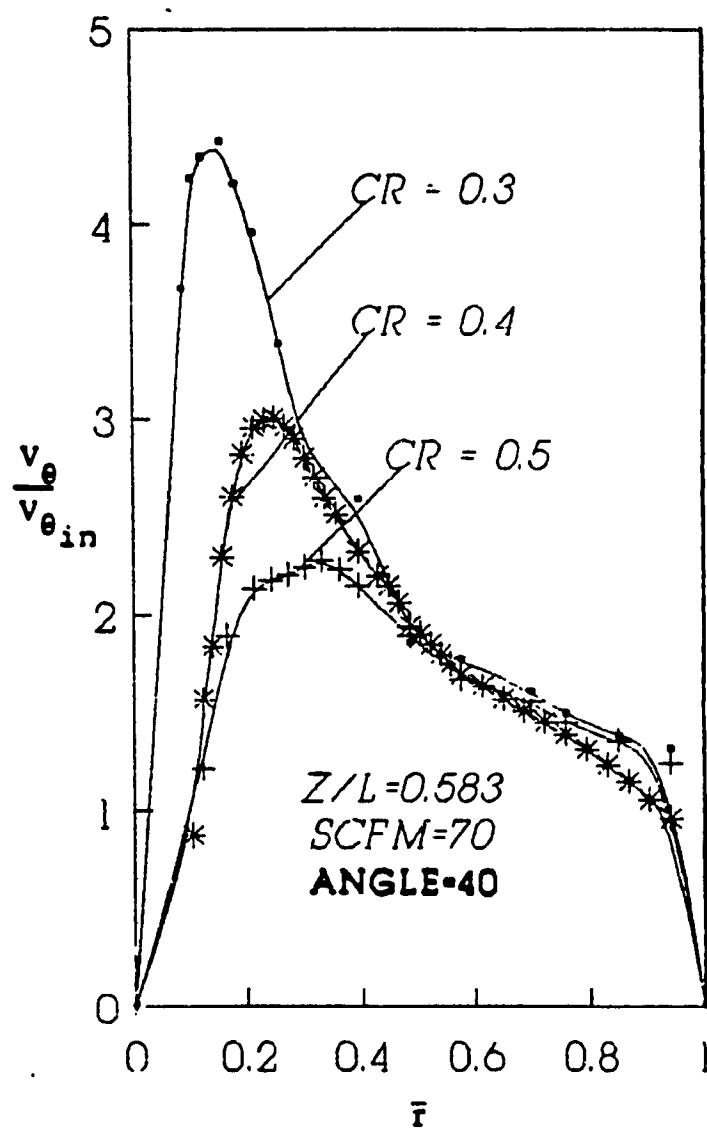


Figure 5.2.1 Measured Tangential Velocity, V_θ , for
Three Different Contraction Ratio, Cr

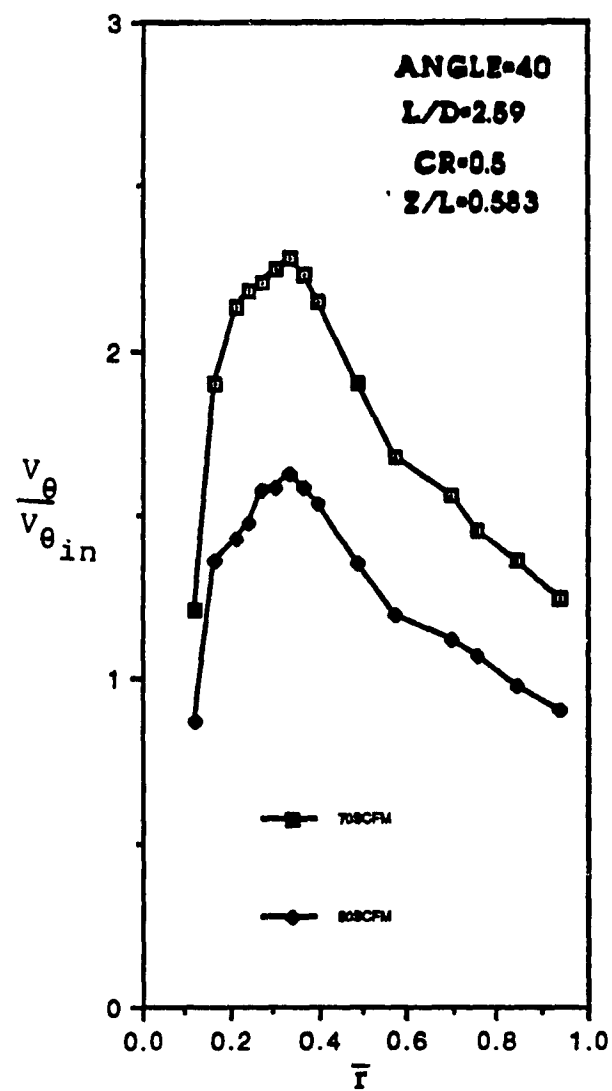
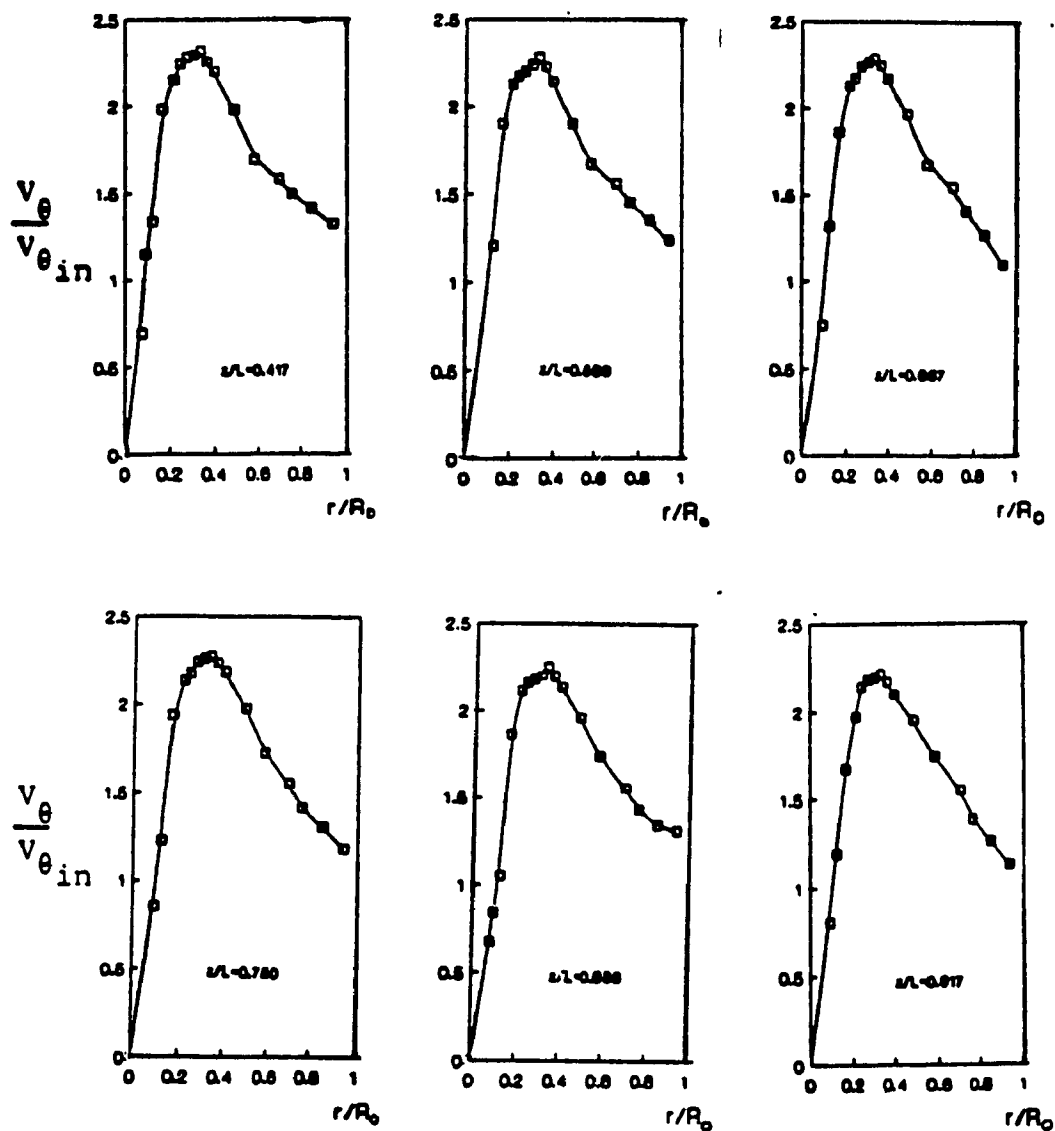


Figure 5.2.2 Measured Tangential Velocity, V_θ , for Two Different Volumetric Flow Rates



ANGLE=40
L/D=2.59
SCFM=70
CR=0.5

Figure 5.2.3 Measured Tangential Velocity, V_θ , for Six Different Axial Locations

Figure 5.2.2 shows the effect of different flow rates on the tangential velocity component. There is approximately 30% difference between the two recorded tangential velocity profiles for the two flow rates. An increase of 40% in volumetric flow rate (i.e. from 50 SCFM to 70 SCFM) does seem to have some influences on the tangential flowfield. The change on the velocity profile due to the increase of flow rate (from 50 to 70 SCFM) is around 30% in terms of magnitude. This could imply that the vortex is sensitive to changes of volumetric flow rate.

In Figure 5.2.3, a series of tangential velocity profiles at different axial positions are shown. The six figures demonstrated that the core remains around the same size in the recorded flowfield (from $z/L=0.417$ to 0.917). The figures also show that there is little changes in the tangential velocity profile between $z/L = 0.417$ to 0.917 . The tangential velocity component is quite stable through out this region.

b) AXIAL VELOCITY

There are no clear cut distinctions that can be found among the three axial velocity profiles from the three contraction ratios ($Cr=0.3, 0.4$ and 0.5) which is shown in Figure 5.2.4. There is no major conclusion that can be obtained from the three measured axial velocity profiles. The irregularities of the three profiles may be due to the oscillation of the core. However, most of the changes are happening near the core region (for $r/R_0 < 0.4$) for every velocity profile. The maximum axial velocity occurs inside or near to the core for $Cr = 0.3$ and 0.4 . For $r/R_0 > 0.4$, all three velocity components increase their magnitudes in the radial direction. For $Cr = 0.4$ and 0.5 , there is

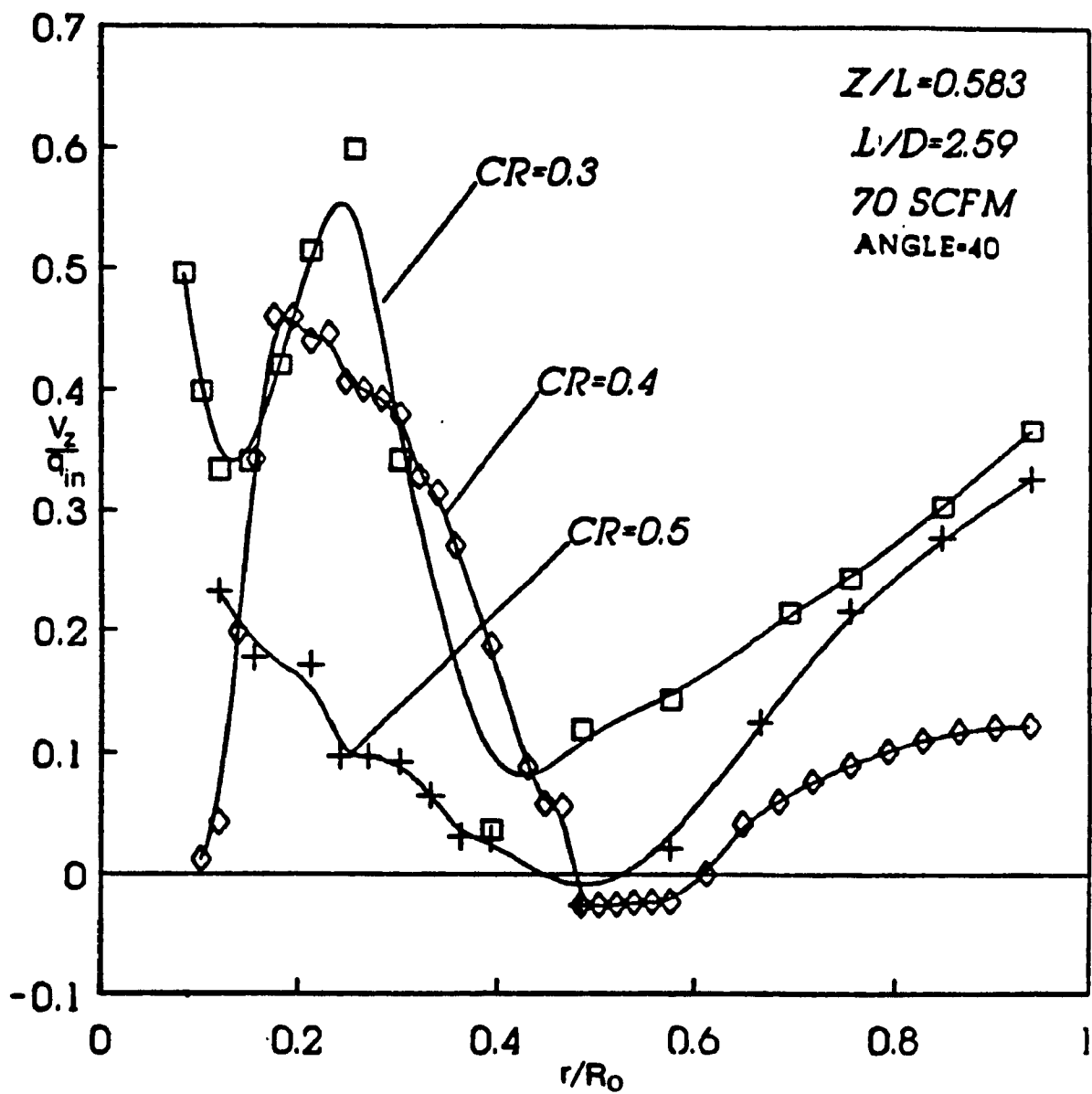


Figure 5.2.4 Measured Axial Velocity, V_z , for
Three Different Contraction Ratios

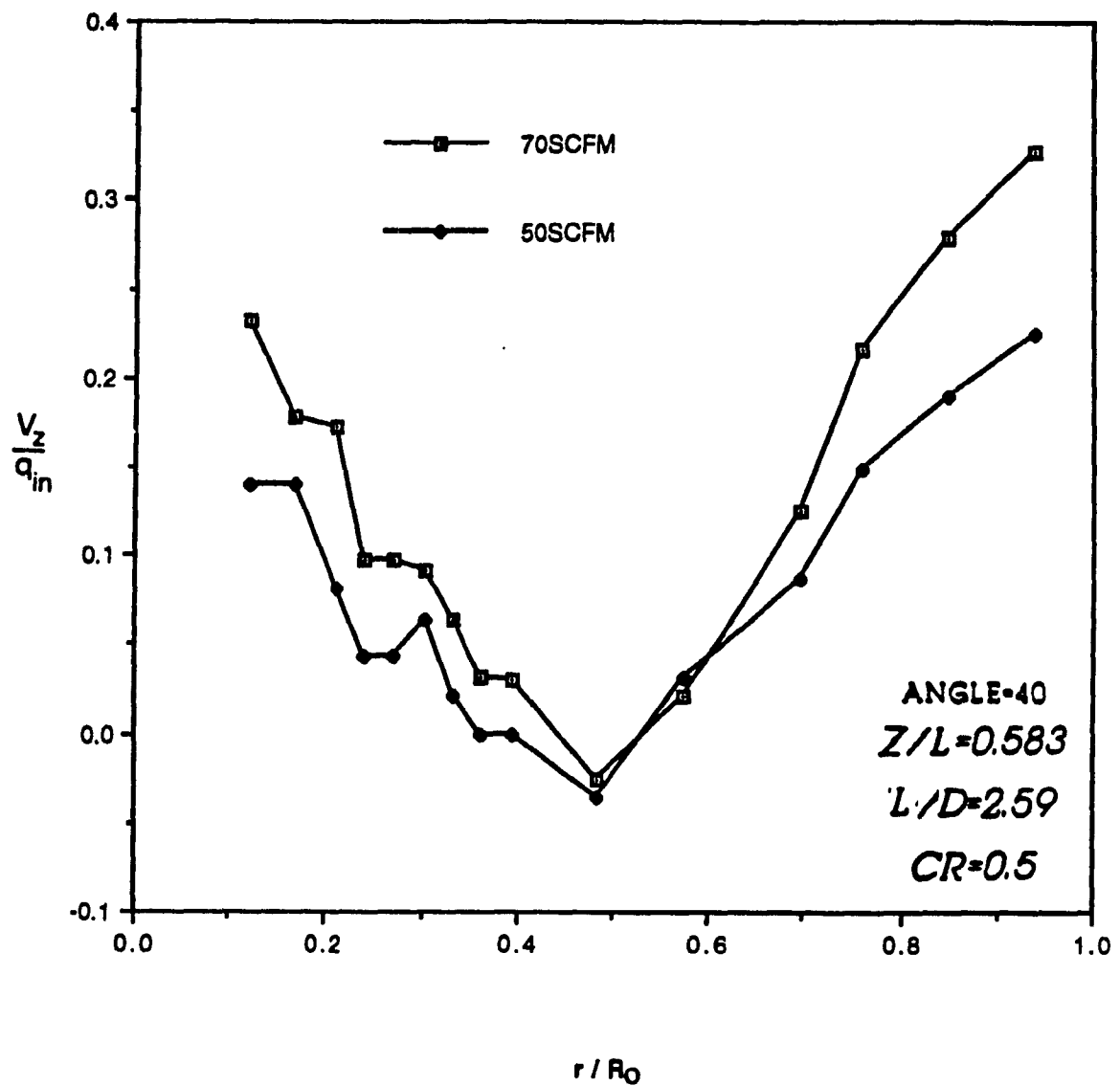
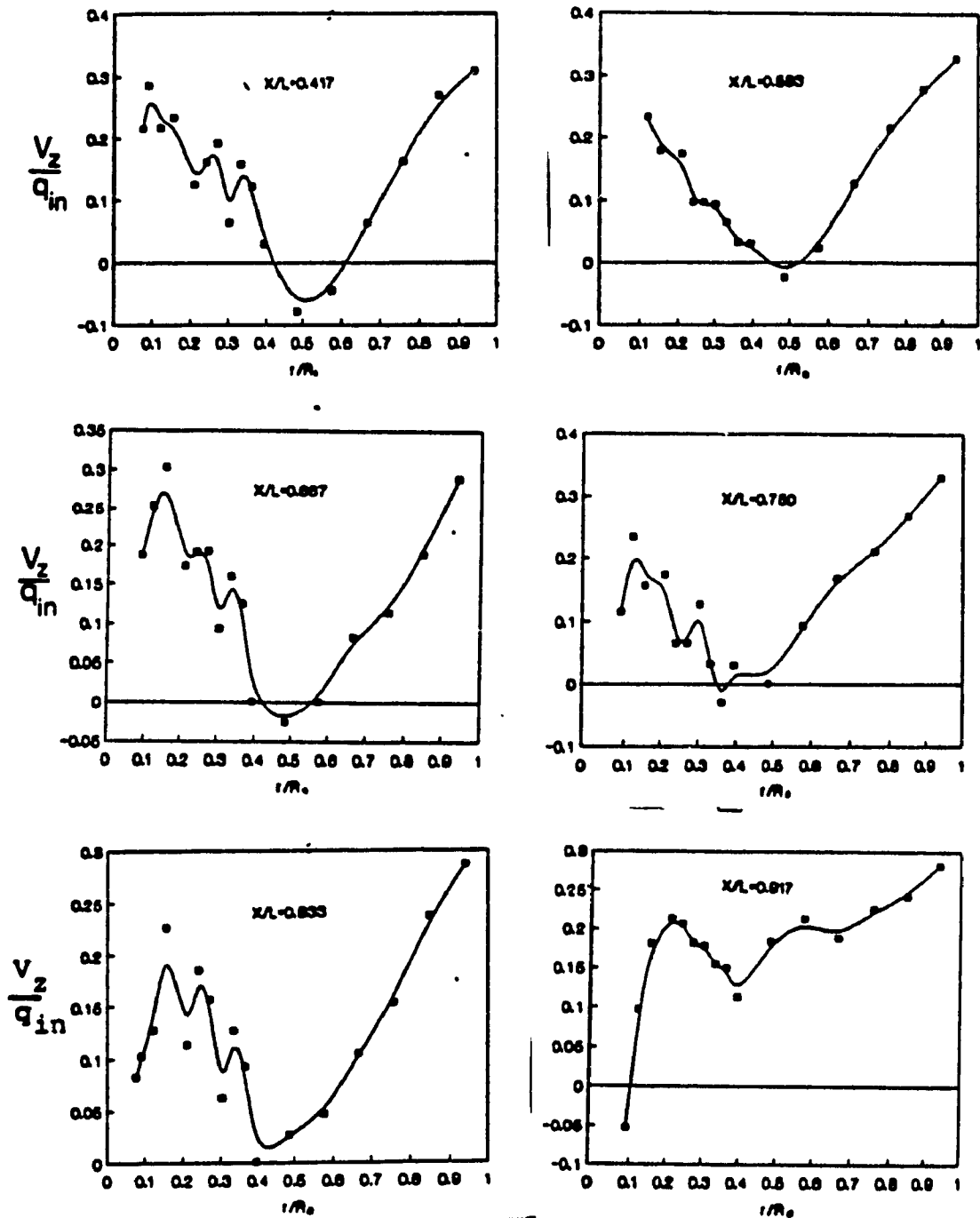


Figure 5.2.5 Measured Axial Velocity, V_z , for Two Different Volumetric Flow Rates



ANGLE=40

L/D=2.59

SCPM=70

CR=0.5

Figure 5.2.6 Measured Axial Velocity, V_z , for Six Different Axial Locations

a small reverse flow region ($V_z < 0$) happens between $r/R_O = 0.4$ to 0.6 .

In Figure 5.2.5, the two axial velocity profiles at two distinct flow rate are compared. For $r/R_O < 0.45$, there is approximately a 40% difference in magnitude. For $r/R_O > 0.45$, the differences are around 30%. However, the two velocity profiles behave in a similar fashion, they both decrease from the core to $r/R_O = 0.5$ and then increase toward $r/R_O = 1$. Both profiles experience a small reverse flow region between $r/R_O = 0.4$ to 0.6 .

The axial progression for the axial velocity is shown in Figure 5.2.6. From $z/L=0.417$ to 0.833 , the axial velocity components basically decrease radially outward from the core region to the center ($r/R_O = 0.5$). There is a small reverse flow region (negative value of V_z) around $r/R_O = 0.5$ for $z/L = 0.417$ to 0.75 . The axial velocity increases radially outward from $r/R_O = 0.5$ to 0.9 for all the six profiles. Also the small reverse flow region at $r/R_O = 0.5$ disappears when it goes downstream (for $z/L = 0.833$ and 0.917).

At the position of $z/L = 0.917$, there is a reverse flow region inside the core. When the flow approaches the exit, the axial velocity profile behaves in a different pattern compare those which are at the location of $z/L < 0.75$. The exit environment has a definite effect on the axial velocity profile, this can be seen from the last two profiles ($z/L = 0.833$ and 0.917). Mass balance had been done at the exit of the vortex chamber to confirmed the axial velocity data is reliable.

The similarity among the axial velocity profiles (decreases from the core to $r/R_O = 0.5$ then increases toward the wall) maintains up to $z/L = 0.750$,

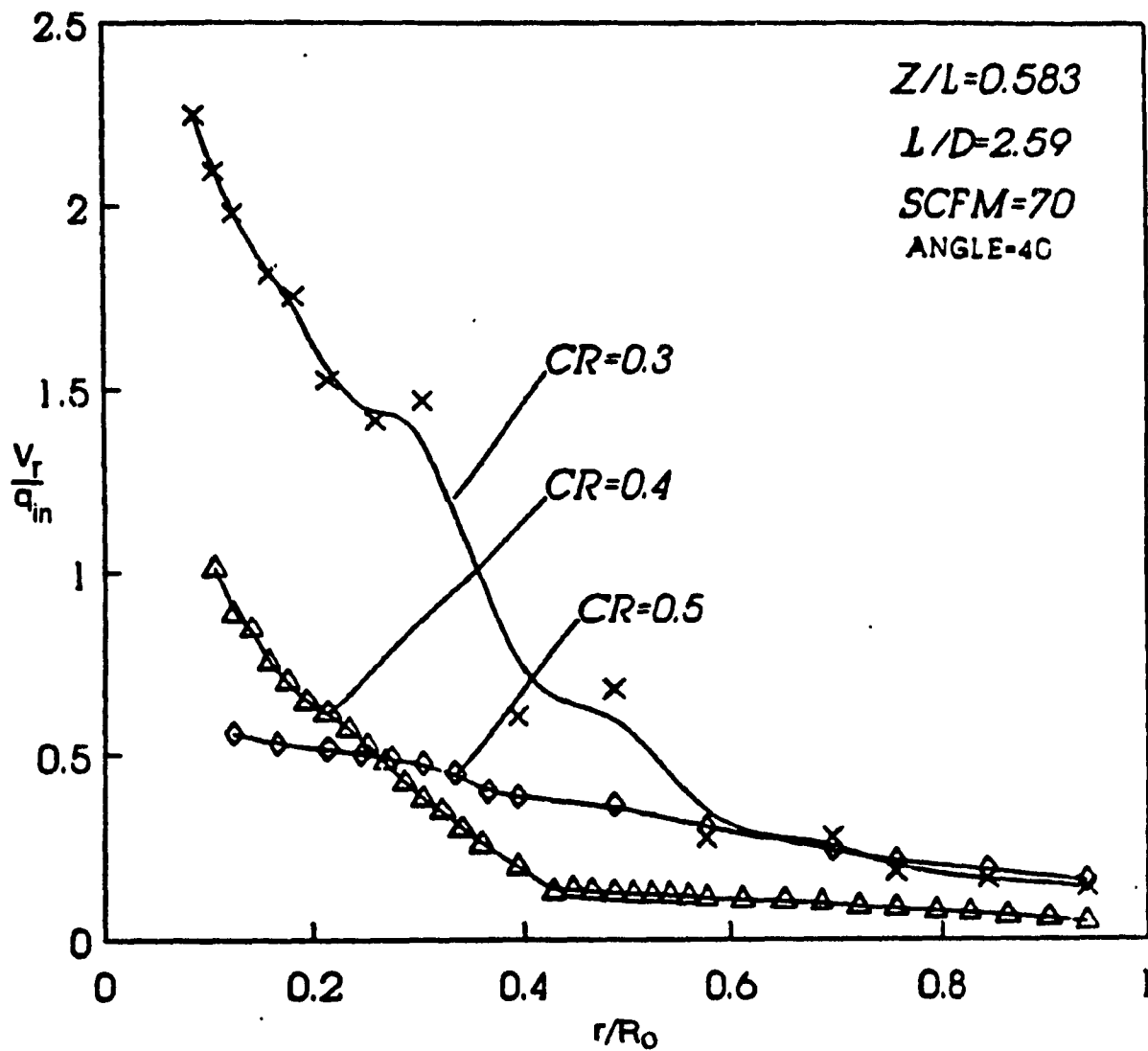


Figure 5.2.7 Measured Radial Velocity, V_r , for Three Different Contraction Ratios

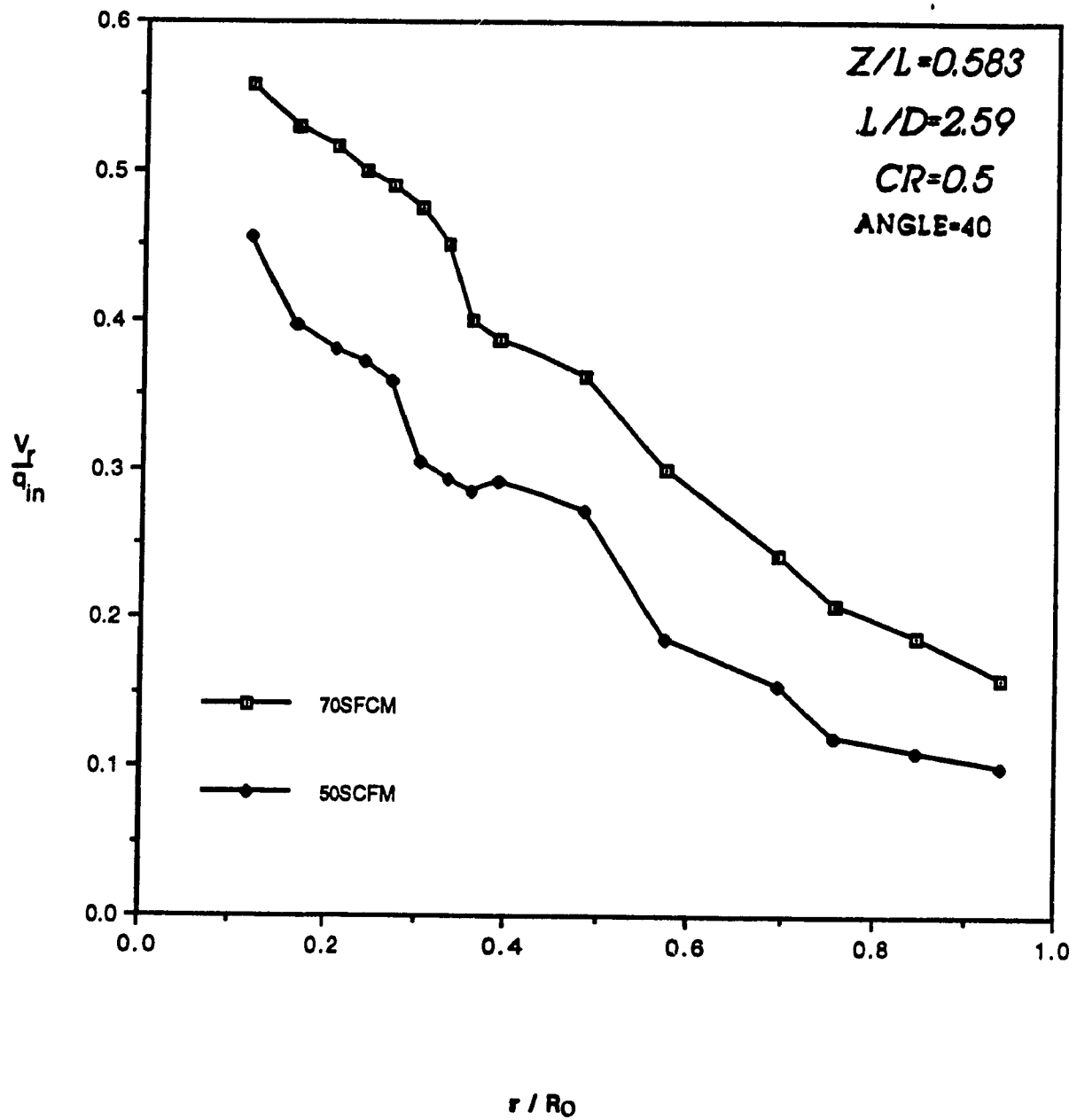
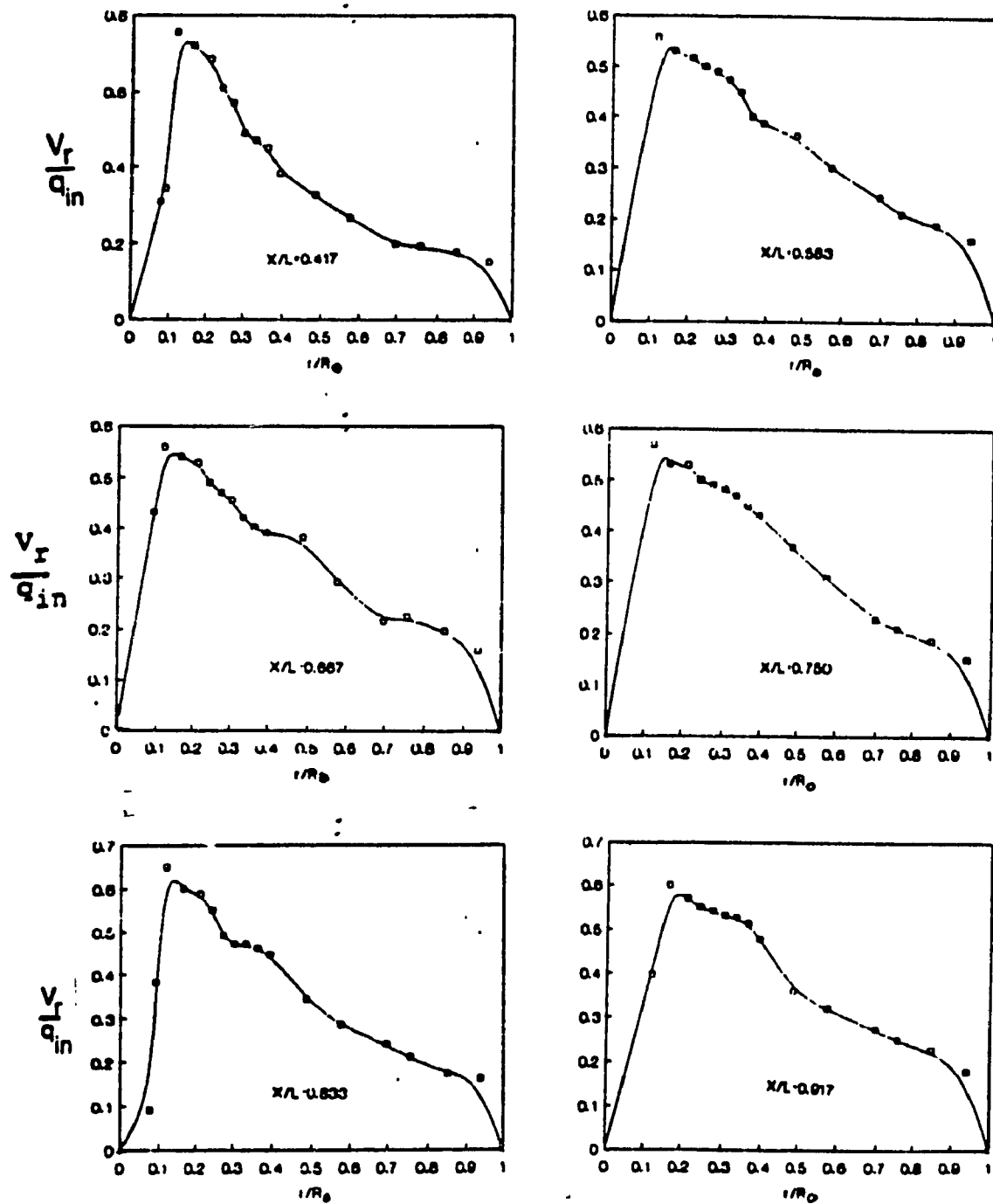


Figure 5.2.8 Measured Radial Velocity, V_r , for Two Different Volumetric Flow Rates



ANGLE=40

L/D=2.59

SCFM=70

CR=0.5

Figure 5.2.9 Measured Radial Velocity, V_r , for Six Different Axial Locations

then it starts to vary when it approaches the exit. However, it is noticeable that the axial velocity near the wall is usually the highest (except $z/L = 0.667$) for most of the axial locations.

c) RADIAL VELOCITY

The third velocity component is going to be discussed is the radial velocity, V_r . Figure 5.2.7 shows the differences between the three profiles which were measured at their respective contraction ratio. It indicates a deviation among the three for $r/R_O < 0.6$. The changes of the radial velocity component occur mainly near the core region (from $r/R_O = 0.1$ to 0.6) and it is quite observable. A decrease of 20% in exit radius (from $Cr = 0.5$ to 0.4) gives a maximum change in magnitude of almost 100% from $r/R_O = 0.1$ to 0.6 . A further decrease of the exit radius (from $Cr = 0.5$ to 0.3) gives an increase of almost 340% in magnitude from $r/R_O = 0.1$ to 0.6 . For $r/R_O > 0.6$, the magnitude of the radial velocity of the three different contraction ratios show limited difference.

In Figure 5.2.8, flow rate variation has a definite influence on the radial velocity component. An approximately 40% difference due to the change of flow rate occurred through out the whole domain. The two velocity profiles decreases radially outward from the core towards the wall region. The sensitive behavior towards the changes of volumetric flow rate has been reflected some observable results.

The axial progression of the radial velocity component is shown in Figure 5.2.9. All the six profiles consist a similar pattern, that the velocity

component decrease from $r/R_O = 0.1$ to 0.95 gradually. The profiles are similar to each other and the exit environment has little effect on the velocity component.

d) STATIC PRESSURE

The static pressure inside the chamber is shown in Figure 5.2.10 for three different contraction ratios. The static pressure profile of the smallest contraction ratio ($Cr=0.3$) contains the highest and smallest static pressure values. The static pressure drops to a negative value as it approaches the core. A decrease of exit radius (from $Cr = 0.5$ to 0.4) by 20% has an effect of almost 50% increase of the maximum static pressure values. A decrease of 40% (from $Cr = 0.5$ to 0.3) in contraction ratio ripples a 240% increase of the maximum static pressure value.

For the two different flow rates, Figure 5.2.11 also indicates some deviations between the two static pressure profiles. The change is more prominent at the two ends of each curve. The slope of the curve is steeper for a higher flow rate. Both profiles attain the negative value at around $r/R_O < 0.3$.

In Figure 5.2.12, the six static pressure profiles in different axial stations show little difference among each other. When the flow approaches downstream, the exit boundary conditions have little effect on the static pressure profile.

The summary of the above discussion can be generalized as follows:

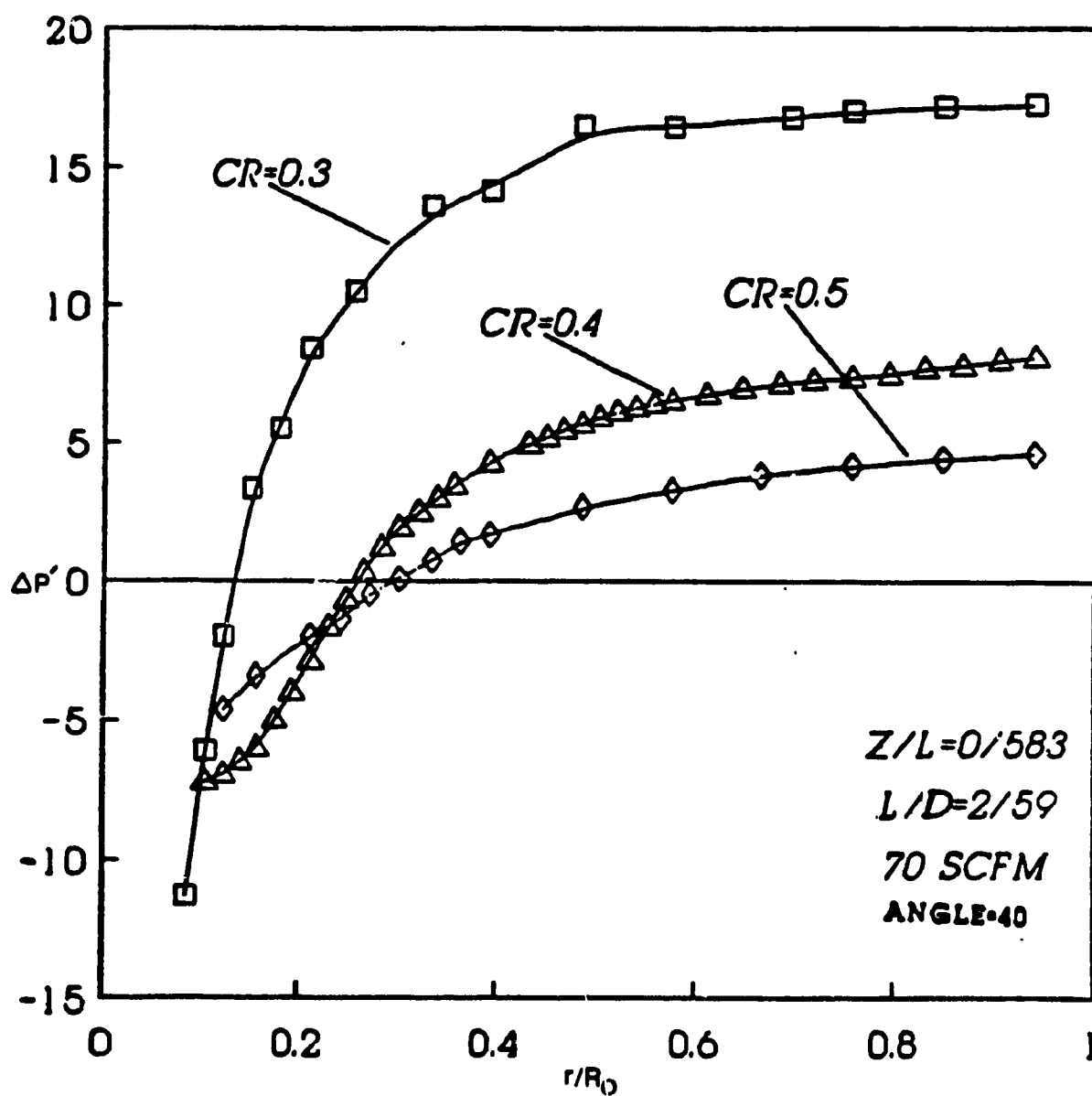


Figure 5.2.10 Measured Radial Pressure, $2(P(r)-P_{amb})/\rho q_{in}^2$, for
Three Different Contraction Ratios

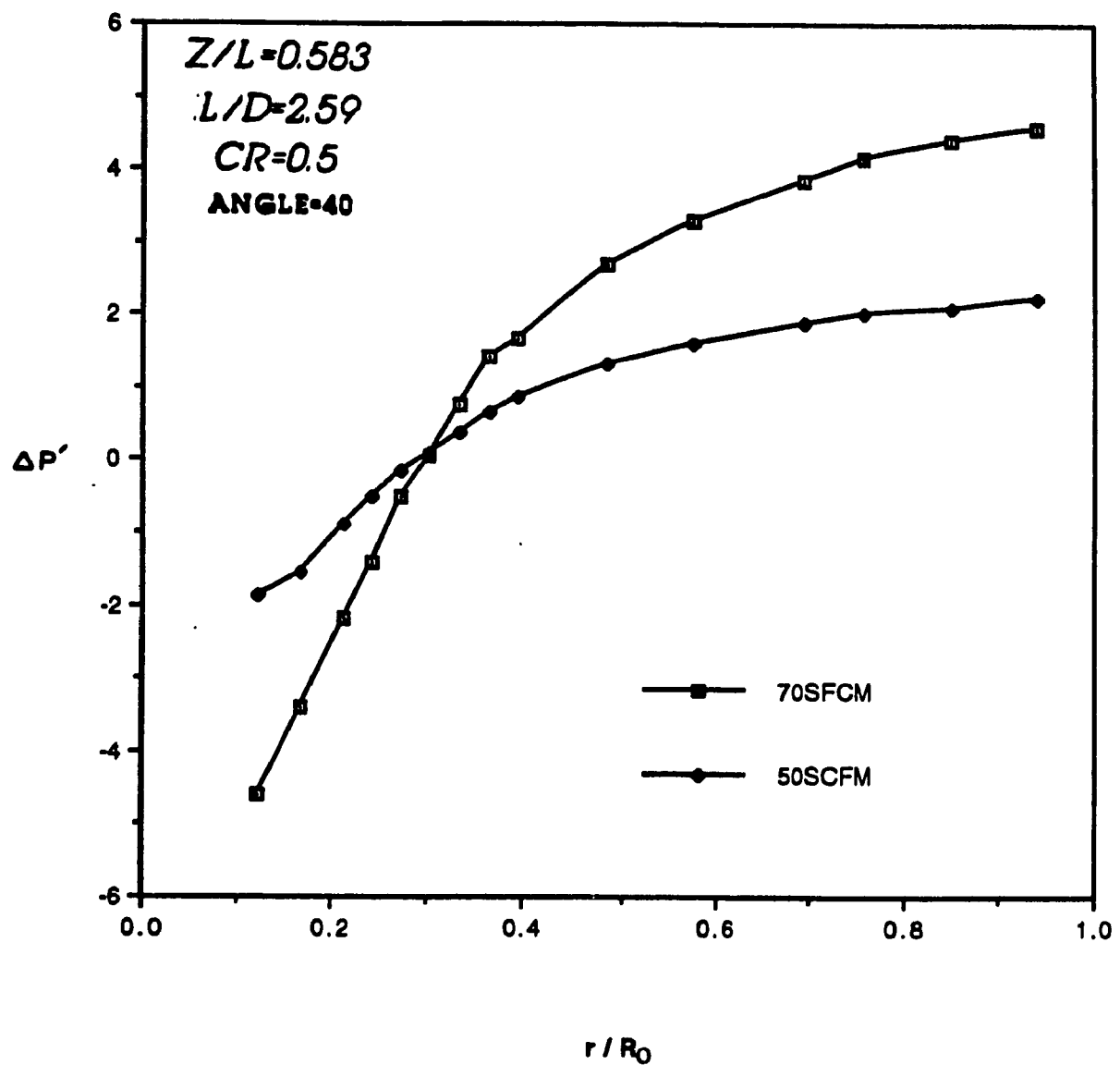
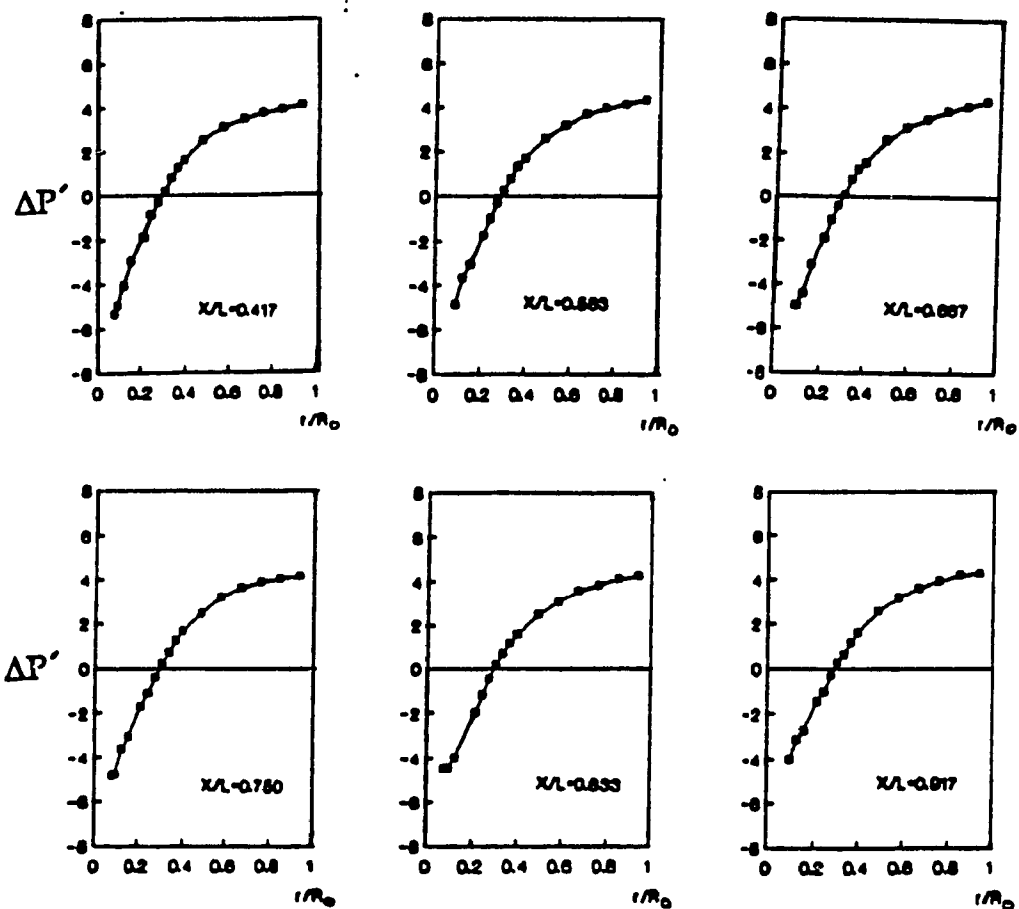


Figure 5.2.11 Measured Radial Pressure, $2(P(r)-P_{amb})/\rho q_{in}^2$, for
Two Different Flow Rates



ANGLE=40
L/D=2.59
SCFM=70
CR=0.5

Figure 5.2.12 Measured Radial Pressure, $2(P(r)-P_{amb})/\rho q_{in}^2$, for Six Different Axial Locations

1. Variation of contraction ratio, $Cr = R_E/R_O$ (for $Cr=0.3, 0.4$ and 0.5)

It causes some observable changes on V_θ and V_r . The changes occur predominantly near the core region. The effect on the static pressure distribution is also quite noticeable. However, no concrete conclusion were arrived at with respect to the axial velocity component.

2. Variation of volumetric flow rate (50 and 70 SCFM)

It affects all the velocity components and the static pressure. The percentage difference in terms of magnitude varies in all the situations.

3. Axial variation

Axial velocity component shows observable changes for different axial locations. The tangential velocity, radial velocity and static pressure show limited axial variation for the six recorded axial locations.

4. The effect of the exit boundary conditions

Among all the velocity and pressure profiles, it affects the axial velocity component to the greatest extent. It has limited effect on the tangential velocity component, radial velocity component and the static pressure.

5.3 THE COMPARISON BETWEEN THE MEASURED AND CORRECTED EXPERIMENTAL DATA

As mentioned in chapter 2, all the experimental data was corrected due to the fact that the flow field is influenced by a strong centrifugal force. The centrifugal effect contributes a pressure error towards $P_4 - P_5$ for the pitot probe during the experimentation. Referring to Eqn.(2.4.11), if the data is

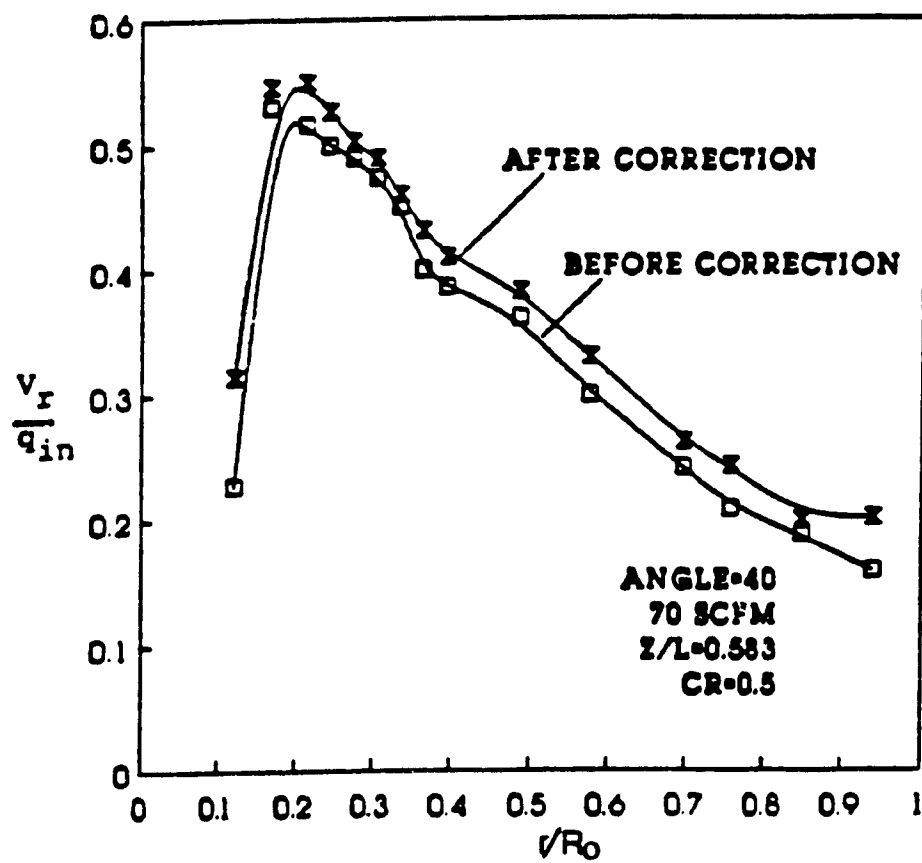


Figure 5.3.1 The comparison between the two sets of radial velocity data

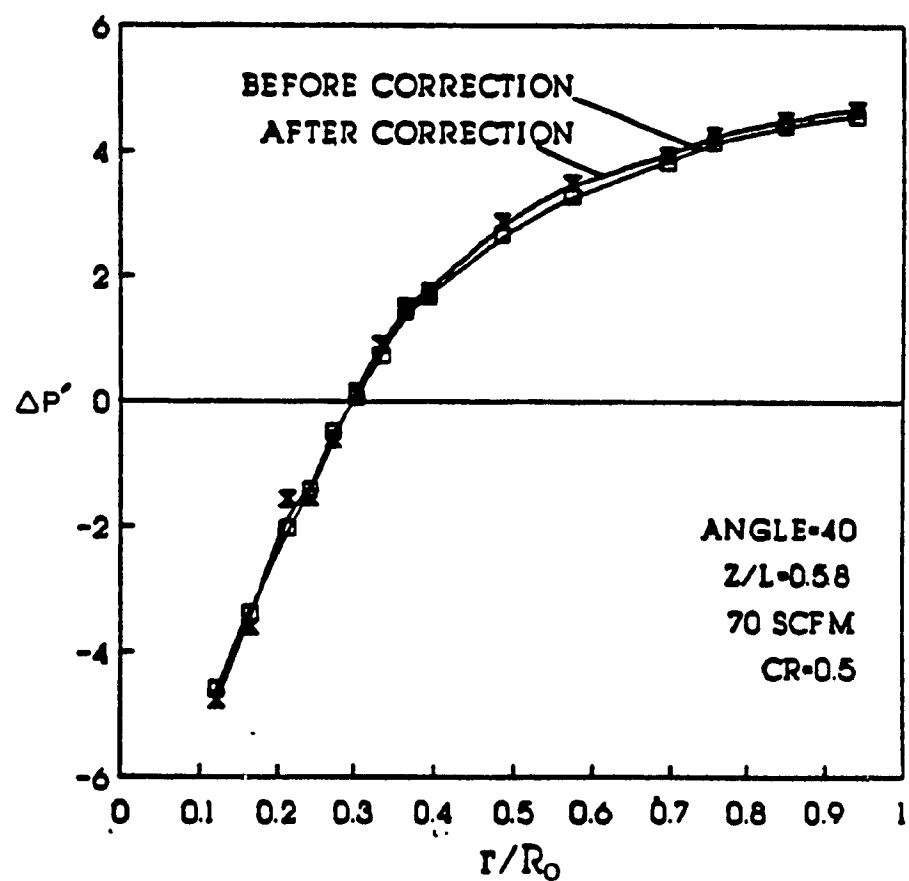


Figure 5.3.2 The comparison between the two set of radial pressure data.

measured below the center line of the apparatus, the error term will be negative. Hence the exact $P_4 - P_5$ values should be larger in magnitude than the recorded one. From the calibration chart (in Appendix II), as $P_4 - P_5$ increases so does the pitch angle ϕ . Hence the corrected V_r should be larger than the original value.

The above argument can be shown in Figure 5.3.1. It shows two radial velocity profiles, one is with correction and the other without correction. The difference is approximately 10%. However, the effect of correction for the tangential velocity, axial velocity and radial pressure is small (less than 5% of changes occur in those variables). The radial pressure profile is shown in Figure 5.3.2 and it indicates limited differences between the two sets of data. The computation process has been described in chapter 2, the numerical method usually converges after 6-8 iterations.

5.4 THE REDUCTION OF PRESSURE DROP BY THE CONICAL PLUG MECHANISM

Vatistas [107] has found out that the pressure drop of the chamber reaches a minimum by inserting a conical plug towards the exit hole. This method has been reused to determine the change of internal flow field due to the existence of the conical plug. The geometric configuration of the conical plug for the experiment is shown in Figure 5.4.1.

Figure 5.4.2 and 5.4.3 show the pressure drop variation due to the position of the conical plug relative to the exit. For $Cr = 0.5$, the minimum pressure drop occurs at $z/H = 0$ and the minimum pressure drop is

approximately 18% less than the one without a plug. For $Cr = 0.3$, the minimum pressure drop is at $z/H = 0.18$ and the reduction of the pressure drop is roughly 20% less than the one without a plug. If the plug is inside the vortex chamber (negative value of z/H), an increase of pressure drop was observed from the experiment. Hence, some pressure drop values can be obtained by two different positions of the conical plug.

The pressure drop reaches a minimum for a particular location of the plug. As the plug was being pulled further away from the exit, the pressure drop across the chamber asymptotically approaches to a value which corresponds to the one without a conical plug. This implies the plug has no influence to the pressure drop across the vortex chamber.

The flowfield inside the vortex chamber was measured at the minimum pressure drop. If Figure 4.1.5 is recalled, $\widetilde{\Delta P}$ (dimensionless pressure drop across the chamber) decreases as X_{CF} increases. Therefore the core size of the vortex with a conical plug at the exit should be expected to be larger than the one without a plug. For the present experiment, X_{CD} and X_{CF} are approximately the same. Figure 5.4.4 confirms the prediction, the normalized core size of the vortex with and without a plug are 0.363 and 0.333 for $Cr=0.5$ respectively. Also the magnitude of the tangential velocity component is higher (from $r/R_O = 0.2$ to 0.95) by using a plug.

The axial velocity in Figure 5.4.5 is higher in the case without the plug. The maximum magnitude of the reverse flow region is higher with the use of the plug. The reverse flow region is from $r/R_O = 0.4$ to 0.65 and $r/R_O = 0.45$ to 0.55 for the case of with and without a plug respectively. The velocity

component has a 10% decrease from $r/R_O = 0.2$ to 0.9 after the plug is being used.

Figure 5.4.6 demonstrates radial pressure distribution, the changes are about 10% - 15%. The radial static pressure is a little lower for the case with the plug.

Figure 5.4.7 illustrates the differences on the radial velocity component between with and without the plug. Most of the deviations occur from $r/R_O = 0.1$ to 0.55 but the changes are limited for $r/R_O > 0.55$.

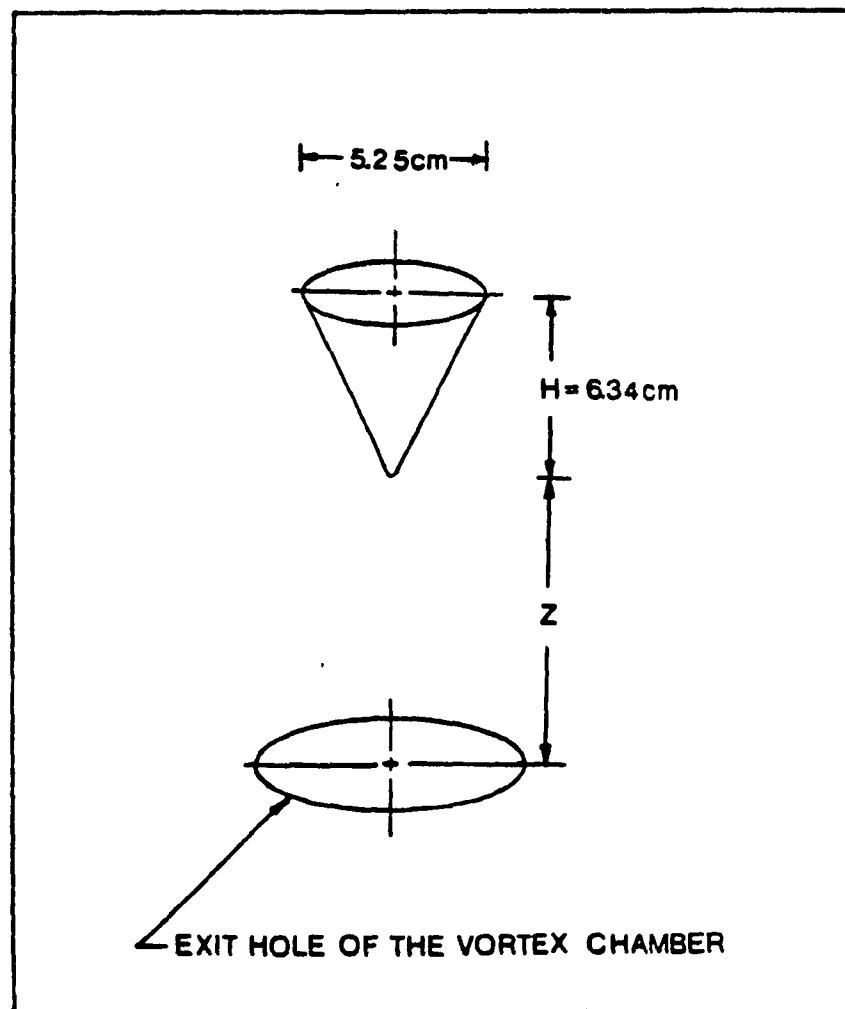


Figure 5.4.1 The Physical Dimensions of the Conical Plug

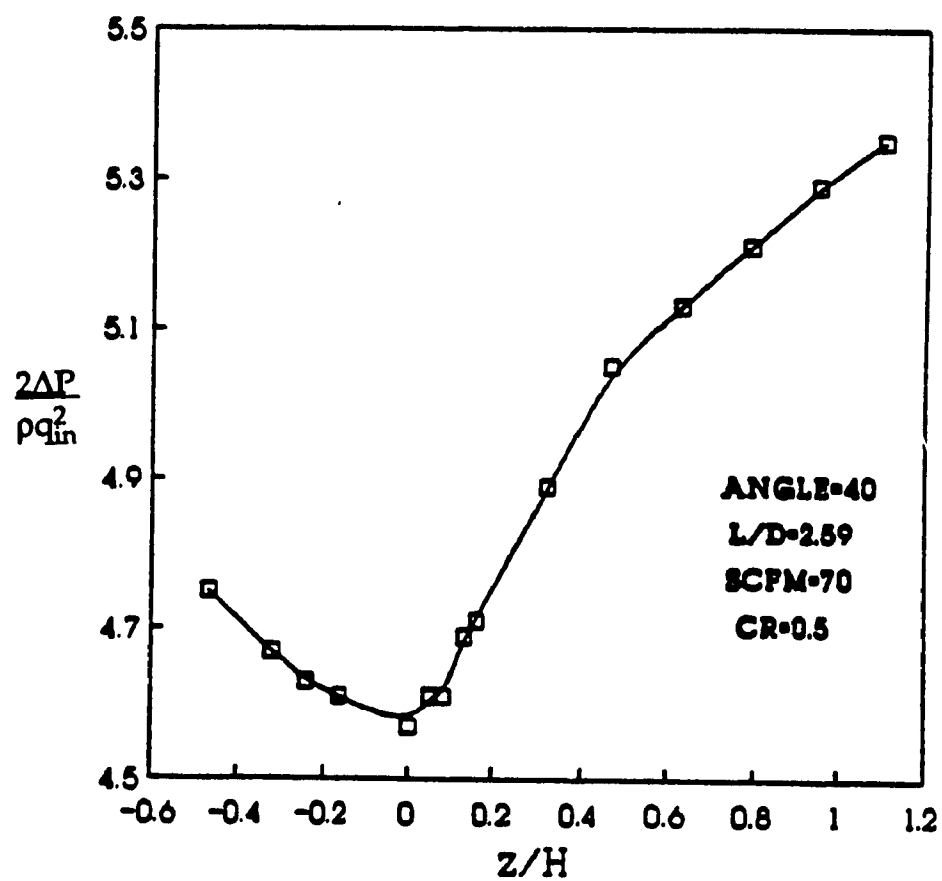


Figure 5.4.2 The pressure drop across the chamber ($2\Delta P/\rho q_{in}^2$) vs. the position of the plug (z/H) at $Cr=0.5$

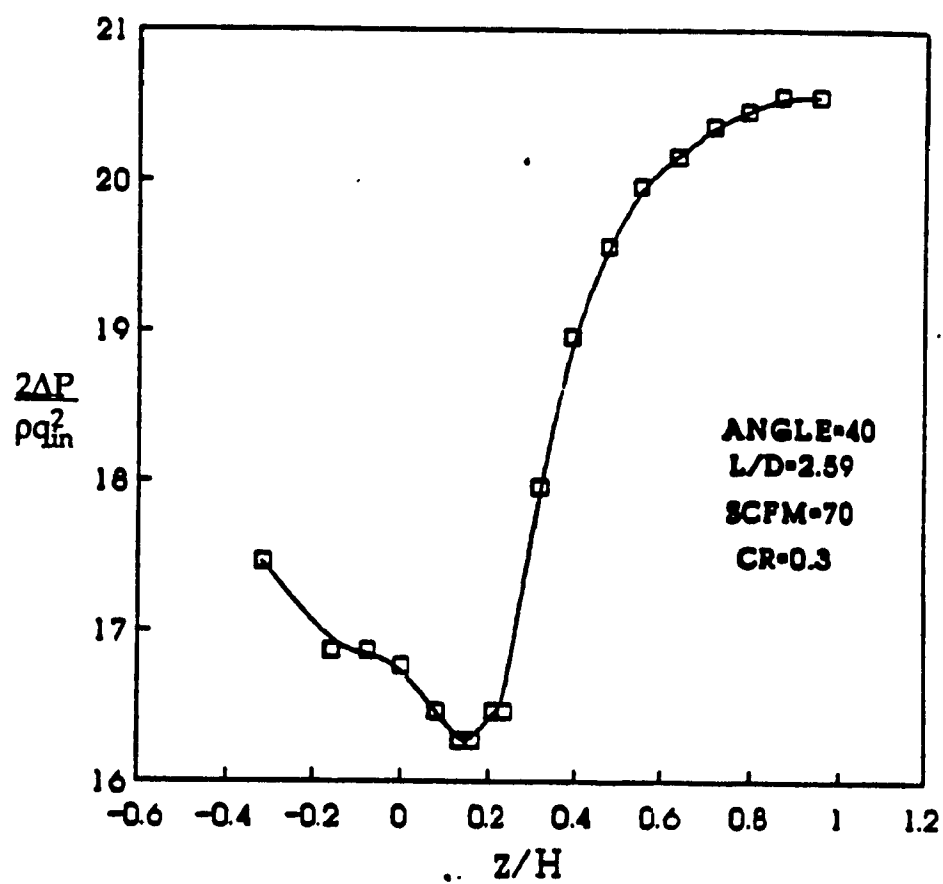


Figure 5.4.3 The pressure drop of a vortex chamber ($2\Delta P/\rho q_{in}^2$) vs. the position of the plug (z/H) at $Cr=0.3$

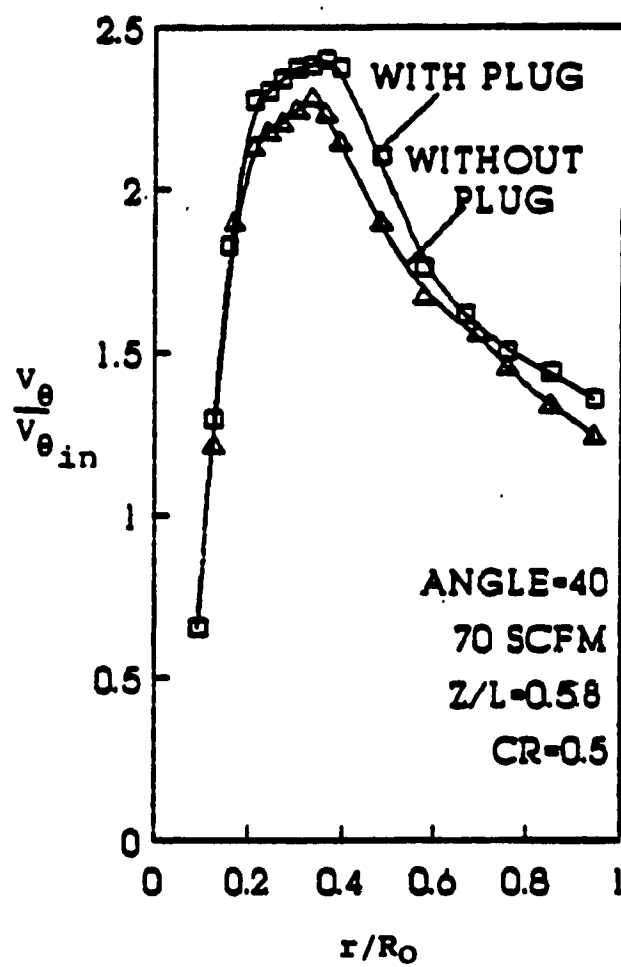


Figure 5.4.4 The comparison between the tangential velocity with and without plug ($V_{\theta}/V_{\theta in}$ vs. r/R_0)

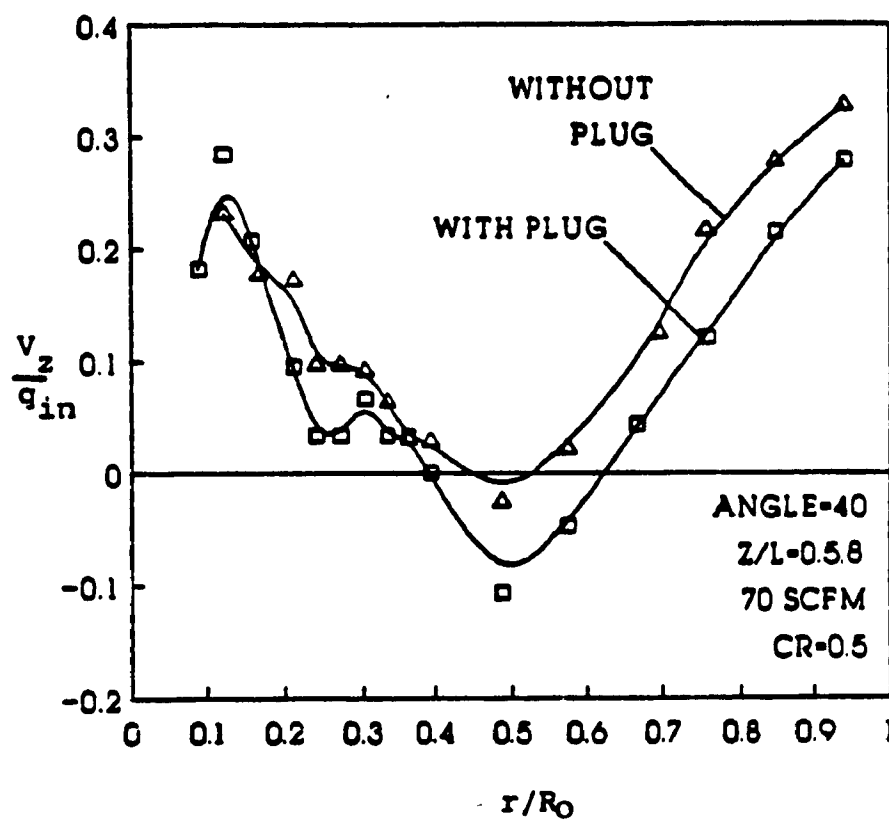


Figure 5.4.5 The comparison between the axial velocity with and without plug (V_z/q_{in} vs. r/R_O)

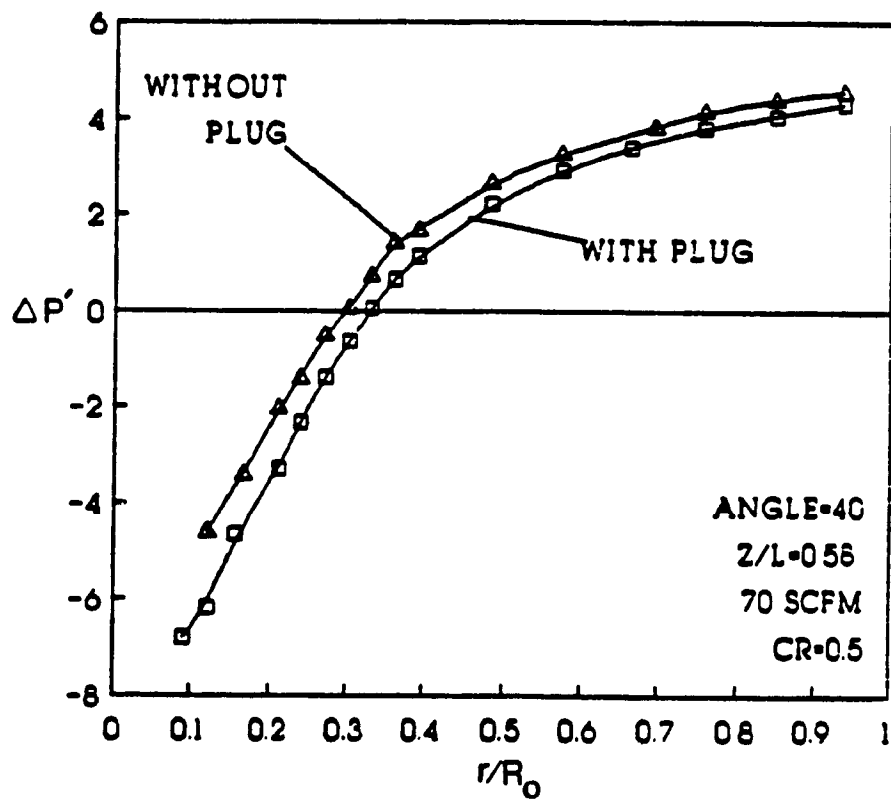


Figure 5.4.6 The comparison between the radial pressure with and without plug ($2(P - P_{amb})/\rho q_{in}^2$ vs. r/R_0)

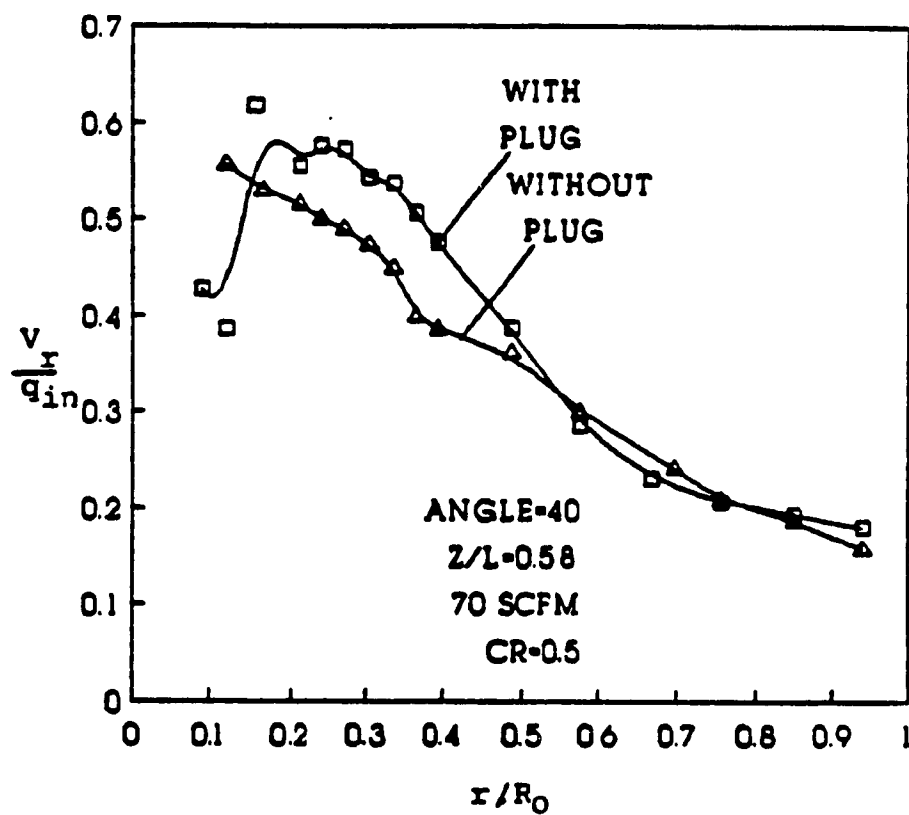


Figure 5.4.7 The comparison between the radial velocity with and without plug (V_r/q_{in} vs. r/R_0)

CHAPTER 6

CONCLUSION

Experimental and dimensional analysis on confined vortex flows were presented.

Flow visualizations using a hydraulic vortex chamber to study the behavior of the vortex core was reported. The results showed that the average core radius is approximately invariant in the axial direction for the case where vortex breakdown had taken place and a wake like core had been formed. Oscillations of the vortex core was evident in the visualization experiment. The amplitude of the oscillations was found to be small in comparison with the size of the vortex core.

Energy balance and continuity over the control volume along with the minimum pressure drop principle has provided formulae that relate the dominant the non-dimensional parameters such as the core size and pressure drop. The analysis showed that the pressure drop and exit core radius is a function of β which consists only by geometric parameters of the vortex chamber. For $\beta < 3$, the derived equations for the pressure drop agreed well with the present and past experimental results. The empirical formula obtained using the least squares method can accurately predict the pressure drop in a wider range of design conditions.

Dimensional analysis produced the functional relationships among the main dimensionless groups. For strongly swirling flows, the derived

relationships for tangential velocity and the radial pressure distribution were shown to correlate well with the presented problem. It was found that the obtained similarity relationships represented well all concentrated vortices regardless of the method their production. The vortex core was found to be situated at approximately the mid-static pressure value of its radial distribution. Furthermore, the present study harmonizes the present and the previous experimental studies.

The experimental studies comprised mapping of the flow characteristics such as the three velocity components and the static pressure as a function of the axial and radial location by using a five hole pitot probe. Different variation of the experimental set up were used in order to cover a wide range of β . A numerical method to filter the centrifugal effects of the pressure on the velocity components was outlined. The post-processed experimental results showed approximately 5% difference from the pre-processed data except the radial velocity component which showed a 10% deviation. The tangential velocity component and radial static pressure showed limited axial variation. However, the axial and radial velocity components displayed noticeable variations along the axial direction. Both components were found to be very sensitive to swirl parameter β . The inadequacy for any experimental method in defining the true value of the maximum tangential velocity was explained due to the presence of inertial waves in the vortex cores.

The pressure drop across the vortex chamber can achieve a minimum value with the incorporation of a conical plug at the exit of the chamber. The

difference in three velocity components and the static pressure, for vortex flowfields with and without a conical plug were experimentally investigated.

REFERENCES

1. Morton, B.R., "Geophysical Vortices", Progress in Aeronautical Science, Pergamon Press, Vol. 7, 1969, pp. 145-194.
2. Dosanjh, D.S., Gasparedk, E.P. and Eskinazis, S., "Decay of a Viscous Trailing Vortex", The Aeronautical Quarterly, May 1962, pp. 167.
3. Newman, B.G., "Flow in Viscous Vortex", Aeronautical Quarterly, Vol. 10, May 1959, pp. 149.
4. Orloff, K.L., "Trailing Vortex Wind-Tunnel Diagnostics with a laser Velocimeter", J. Aircraft, Vol. 11, No. 8, August 1974, pp. 447-482.
5. Boeing Report DG-32322 TN, "737 Engine Inlet Vortex Dissipator Development Program", Boeing Company, Seattle, Washington, December 1969.
6. Knauss, J. (Editor) "Swirling Flow Problems at Intakes", A.A. Balkema, Rotterdam, Netherlands, 1987.
7. Cassidy, J.J. and Falvey, H.T., "Observations of Unsteady Flow Arising After Vortex Breakdown", Journal of Fluid Mechanics, Vol. 41, 1970, pp. 727-736.
8. Falvey, H.T., "Draft Tube Surges. A Review of Present Knowledge and an Annotated Bibliography", US Bur. Reclam. Rep. REC-ERC-71-42, 1971.
9. Kubota, T. and Matsui, H., "Cativation Characteristics of Forced Vortex Core in the Flow of the Francis Turbine", Fuji Electr. Rev. Vol. 18, 1972, pp. 102-108.
10. Panton, R.L., "Incompressible Flow", John Wiley and Sons, N.Y., 1984.
11. Binnie, A.M. and Hookings, G.A., "Laboratory Experiments on Whirlpools", Proc. R. Soc. London Ser. A, Vol. 194, 1984, pp. 398-415.

12. Abramson, N.H. (Editor), "The Dynamic Behavior of Liquids in Moving Containers", NASA SP-106, 1966.
13. Peckham, D.H. and Atkinson, S.A., "Preliminary Results of Low Speed Wind Tunnel Tests on a Gothic Wing Aspect Ratio 1.0", Aeronautical Research Council, CP508, 1957.
14. Earnshaw, P.B. and Lawford, J.A., "Low Speed Wind Tunnel Experiments on a Series of Sharp-Edged Delta Wings", Aeronautical Research Council, R and M 3424, 1966.
15. Hummel, D. and Srinivasan, P.S., "Vortex Breakdown Effects on the Low Speed Aerodynamic Characteristic of Slender Delta Wings in Symmetrical Flow", Journal of the Royal Aeronautical Society, Vol. 71, 1967, pp. 319-332.
16. Leibovich, S., "Vortex Stability and Breakdown: Survey and Extension", AIAA Journal, Vol. 22, No. 9, September 1984, pp. 1192-1206.
17. Wilkins, E.M., "The Role of Electrical Phenomena Associated with Tornadoes", Journal of Geophysical Research, Vol. 69, No. 12, June 19, 1964, pp. 2435-2447.
18. Davies-Jones, R.P., "The Dependence of Core Radius on Swirl Ratio in a Tornado Simulator", Journal of the Atmospheric Sciences, Vol. 30, October 1973, pp. 1427-1430.
19. Sinclair, P.C., "The Lower Structure of Dust Devils", Journal of the Atmospheric Science, Vol. 30, November 1973, pp. 1599-1619.
20. Golden, J.H., "The Life Cycle of Florida Keys' Waterpouts", Journal of Applied Meteorology, Vol. 13, September 1974, pp. 676-689.
21. Zemansky, N.W., "Heat and Thermodynamics", McGraw Hill Inc., 5-th Edition, New York, 1968.

22. Samaras, D.G., "Theory of Ion Flow Dynamics", Dover Publications Inc., New York, 1971.
23. Lugt, H.J., "Vortex Flow in Nature and Technology", John Wiley and Sons Inc., N.Y., 1983.
24. Escudier, M.P., Bornstein, J. and Zehnder, N., "Observations and LDA Measurements of Confined Vortex Flow", Journal of Fluid Mechanics, Vol. 98, Part 1, 1980, pp. 49-63.
25. Chanaud, R.C., "Observations of Oscillatory Motion in Certain Swirling Flows", Journal of Fluid Mechanics, Vol. 21, 1965, pp. 111-127.
26. Sarpkaya, T., "Effect of Adverse Pressure Gradient on Vortex Breakdown", AIAA Journal, Vol. 12, Dec. 1974, pp. 602-607.
27. Faler, J.H. and Leibovich, S., "An Experimental Map of the Internal Structure of a Vortex Breakdown", Journal of Fluid Mechanics, Vol. 86, 1978, pp. 313-315.
28. Vatistas, G.H., Lin, S. and Kwok, C.K., "Theoretical and Experimental Studies on Vortex Chamber Flows", AIAA Journal, Vol. 24, No. 4, pp. 635-642, April, 1986.
29. Holman, J.P. and Moore, G.D., "An Experimental Study of Vortex Chamber Flow", Transactions of the ASME, Dec, 1961, pp. 632-636.
30. Escudier, M.P., Bornstein, J., Zehnder, J. and Maxworthy, J., "The Classification Confined Vortex Flow Regimes", Vortex Flows, presented at the Winter Annual Meeting of the American Society of Mechanical Engineers, Chicago, Illinois, Nov. 1980, pp15-24.
31. Bank, N. and Gauvin, W.H., "Measurements of Flow Characteristics in a Confined Vortex Flow", The Canadian Journal of Chemical Engineering, Vol. 55, 1977, pp. 397.

32. Reydon, R.F. and Gauvin, W.H., "Theoretical and Experimental Studies of Confined Vortex Flow", The Canadian Journal of Chemical Engineering, Feb, 1981, pp. 14-23.
33. Kerrebrock, J.L., and Meghreblian, R.V., "Vortex Containment for the Gaseous- Fission Rocket", Journal of Aerospace Science, Vol. 28, 1961, pp. 710.
34. Ragsdale, R.G., "NASA Research on the Hydrodynamics of the Gaseous Vortex Reactor", NASA TN D-288, September 1960.
35. Kerrebrock, J.L. and Meghreblian, R.V., "An Analysis of Vortex Tubes for Combined Gas-Phase Fission Heating and Separation of the Fissionable Material", Report CF-57-11-3, Oak Ridge National Laboratory, April 11, 1958.
36. Kerrebrock, J.L. and Keyes, J.J. "A Preliminary Experimental Study of Vortex Tubes for Gas Phase Fission Heating", ORNL 2660, February 20, 1959.
37. Kerrebrock, J.L. and Lafayatis, R.G., "Analytical Study of some Aspects of Vortex Tubes for Gas-Phase Fission Heating", Report CF-58-7-4, ORNL, July 21, 1958.
38. McLafferty, G.H., "Survey of Advanced Concepts in Nuclear Propulsion", ALAA Paper No. 67-783, October 1967.
39. McLafferty, G.H. and Bauer, H.E., "Studies of Specific Nuclear Light Bulb and Open-Cycle Vortex Stabilized Gaseous Nuclear Rocket", NASA CR-1030, April 19 6.
40. Black, D.L., Kyslinger, J.A. and Ravets, J.M., "The Collid Core Reactor Rocket Engine Concept", Trans. Am. Nucl. Soc, Vol. 17, 1983, pp. 6-7.

41. Lakshimikantha, H., "Investigation of Two Phase Vortex Flows with Applications to a Cavity Nuclear Rocket", Ph.D. Thesis, MIT, Cambridge 1973.
42. Kwok, C.K., Lee, P.M. and Lin, S., "An Analytical Investigation of a Vortex Flowmeter", ISA Transaction, Vol. 14, No. 2, 1975.
43. Struiksma, N., "The Cyclone Pump", Journal of Hydraulic Research, Vol. 23, No. 2, 1985, pp. 165-178.
44. Schneck, R.J., "The Vortex Ejector Pump", Master Thesis, Mechanical Engineering Department, Concordia University, Montreal, Canada, 1971.
45. Tanasawa, Y., and Nakamura, K., "On the Vortex Combustor as Applied to the Gas Turbine", Paper JSME-15, Presented at the Joint JSME/ASME Tokyo International Gas Turbine Conference and Products Show, 1971.
46. Tanasawa, Y., and Nakamura, K., "On the Vortex Combustor as Applied to the Gas Turbine", JSME-15, Paper presented at the Joint JSME/ASME Tokyo International Gas Turbine Conference and Products Show, Tokyo, Japan, Oct. 4-7, 1971.
47. Syred, N., Chigier, N.A. and Beer, J.M., "Flame Stabilization in Recirculation Zones of Jets with Swirl", 13-th International Symposium on Combustion, pp. 617-624, Combustion Institute, Pitts., PA., 1971.
48. Syred, N. and Beer, J.M., "Combustion in Swirling Flows: A Review", Combustion and Flame, Vol. 23, 1974, pp. 143-201.
49. Krepec, T. and Kwok, C.K., "Problems Encountered in the Development of a Double Cyclone Furnace", 16-th South-Eastern Seminar on Thermal Sciences, Miami, Florida, U.S.A., 1982.
50. Krepec, T. and Kwok, C.K., "Preliminary Investigations of a Double Vortex Combustion Chamber", Fall Meeting of Combustion Institute, Eastern Section, Pittsburgh, U.S.A., 1981.

51. Georgantas, A., Krepec, T. and Kwok, C.K., "Flow Pattern Investigations in a Model of Double Vortex Combustion Chamber", Presented in 1982 Spring Technical Meeting of Combustion Institute, Canadian Section, Banff, Alberta.
52. Georgantas, A., Krepec, T. and Kwok, C.K., "Investigation of Double Vortex Structure and its Ability to Retain Fuel Particles in a Cyclone Combustion Chamber", Presented in 1983 Fall Technical Meeting of the Combustion Institute, Eastern Section, Providence, Rhode Island.
53. Baluev, E.D. and Troyankin, Y.V., "Study of the Aerodynamic Structure of Gas Flow in a Cyclone", Thermal Engineering, Vol. 14, 1967, pp. 84-87.
54. Syred, N., Dahmen, K.R., Styles, A.C. and Najim, S.E., "A Review of Combustion Problems Associated with Low Calorific Value Fuels", Journal of the Institute of Fuel, Vol. 1, No. 405, Dec. 1977, pp. 195-207.
55. Kalishevskii, L.L. and Ganchev, B.G., "A Study of Combustion in a Horizontal Cyclone Furnace", Thermal Engineering, Vol. 12, 1965, pp. 96.
56. Troyankin, Y.U. and Baleuv, E.D., "The Aerodynamic Resistance and Efficiency of a Cyclone Chamber", Thermal Engineering, Vol. 16, 1968, pp. 29.
57. Ustimenko, B.P. and Buchman, M.A., "Turbulent Flow Structure in a Cyclone Chamber", Thermal Engineering, Vol. 15, 1968, pp. 64.
58. Styles, A.C., Syred, N. and Najim, S.E., "Turbulent Flow Structures and Recirculation Patterns Associated with Cyclone Combustors and Their Effect on Flame Stabilization", Proceedings of the Symposium on turbulent Shear Flows, April 1977, pp. 725.
59. Styles, A.C., Syred, N. and Najim, S.E., "A Study of Modulable Cyclone Combustors Using Gaseous Fuels", Journal of the Institute of Fuel, December 1979, pp. 159-168.

60. Najim, S.E., Styles, A.C. and Syred, N., "Stabilization of Low Calorific Value Gases in a Cyclone Combustor", *AIAA Journal of Energy*, Vol. 5, No. 1, January-February 1981, pp. 43-50.
61. Gupta, A.K., Lilley, D.G. and Syred, N., "Swirl Flows", Abacus Press, Tunbridge Wells, 1984.
62. Kelsall, D.F., "A Study of the Motion of Solid Particles in a Hydraulic Cyclone", *Trans. Instrn. Chem. Engrs.*, Vol. 30, 1952, pp. 87-108.
63. Kelsall, D.F., "A Further Study of the Hydraulic Cyclone", *Chemical Engineering Sciences*, Vol. 2, 1963, pp. 254-272.
64. Dietz, P.W., "Collection Efficiency of Cyclone Separators", *AIChE Journal*, Vol. 27, No. 6, November 1981, pp. 888-892.
65. Rietema, K., "Performance and Design of Hydrocyclones - I, II and III", *Chemical Engineering Science*, Vol. 15, No. 3 and 4, September 1961, pp. 298-315.
66. Ogawa, A., "Axial and Radial Diffusion of the Fine Solid Particles in the Turbulent Rotational Air Flow in the Returned Flow Type of the Vortex Chamber", *Journal of the College of Engineering of Nihon University, Series A*, Vol. 27, March 1986, pp. 23-42.
67. Ter Linden, A.J., "Cyclone Dust Collectors for Boilers", *Trans. ASME*, Vol. 75, 1953, pp. 433-440.
68. Dabir, B. and Petty, C.A., "A Comparative Study Using Laser Doppler Anemometry of Mean Velocity Profiles in Hydrocyclones Having Different Vortex Finder Geometries", Paper Presented at the Pacific Region Meeting of the Fine Particle Society, August 1-5, 1983, Honolulu, Hawaii.
69. Rietema, K. and Verver, C.G., "Cyclones in Industry", Elsevier Publishing Company, Princeton, N.J., 1961.

70. Ogawa, A., Seito, O. and Nagabayashi, H.S., "On the Spin-Up Time of the Turbulent Rotational Air Flows in the Special Forms of the Cyclone Dust Collectors", Bulletin of JSME, Vol. 29, No. 252, June 1986, pp. 1698-1703.
71. Ogawa, A., "Estimation of the Collection Efficiencies of the Three Types of the Cyclone Dust Collectors from the Standpoint of Flow Patterns in the Cylindrical Cyclone Dust Collectors", Bulletin of JSME, Vol. 27, No. 223, January 1984, pp. 64-69.
72. Li, P.M., Lin, S., and Vatistas, G.H., "Predicting Collection Efficiency of Separation Cyclones: A Momentum Analysis", The Canadian Journal of Chemical Engineering, Vol. 65, October 1987, pp. 730-735.
73. Stairmand, C.J., "The Design and Performance of Cyclone Separators", Trans. Inst. Chem. Eng., Vol. 29, 1951, pp. 356-358.
74. Lay, J.E., "An Experimental and Analytical Study of Vortex-Flow Temperature Separation by Superposition of Spiral and Axial Flows, Part 1 and 2", Trans. ASME, Journal of Heat Transfer, 1959, pp. 202-221.
75. Ranque, G. "Expériences sur la Détente Gigatoire avec Productions Simultanées d'un Echappement d'Air Chaud et d'un Echappement d'Air Froid", J. Phys. Radium, Vol. 4, 1933, pp. 1123-1155.
76. Hilsch, R. "Die Expansion von Gasen im Zentrifugalfeld als Kälteprozess", Z. Naturforsch., Vol. 1, 1946, pp. 208-214, Transl., 1974, in Rev. Sci. Instrum., Vol. 18, pp. 108-113.
77. Bruum, H.H., "Experimental Investigation of the Energy Separation in Vortex Tubes", J. Mech. Eng. Sci., Vol. 11, 1969, pp. 567-582.
78. Diessler, R.G. and Perlmutter, M., "An Analysis of the Energy Separation in Laminar and Turbulent Compressible Vortex Flows", Proc. Heat Transfer Fluid Mech. Inst., Stanford University Press, Stanford, California, 1958, pp. 40-53.

79. Diessler, R.G. and Perlmutter, M., "Analysis of the Flow and Energy Separation in a Turbulent Vortex", *Inst. J. Heat Mass Transfer*, Vol. 1, 1960, pp. 173-191.
80. Kurosaka, M., "Acoustic Streaming in Swirling Flow and Ranque-Hilsch (Vortex Tube) Effect", *J. Fluid Mech.*, Vol. 124, 1982, pp. 139-172.
81. Linderstrom-Lang, C.U., "Gas Separation in the Ranque-Hilsch Vortex Tube", *Int. J. Heat Mass Transfer*, Vol. 7, 1964, pp. 1195-1206.
82. Reynolds, A.J., "Energy Flows in a Vortex Tube", *ZAMP*, Vol. 12, 1961, pp. 343-357.
83. Stefanides, E.J., "Ranque Vortex Tube Cools Locomotive Drinking Water", *Des. News*, January 24, 1962, pp. 14-15.
84. Vonnegut, B., "Vortex Thermometer for Measuring True Temperature and True Air Speeds in Flight", *Rev. Sci. Instrum.*, Vol. 21, 1950, pp. 136-141.
85. Westley, R., "Optimum Design of a Vortex Tube for Achieving Large Temperature Drop Ratio", *Coll. Aeronaut., Cranfield*, Note No. 30, 1955.
86. Westley, R., "Vortex Tube Performance Data Sheets", *Coll. Aeronaut., Cranfield*, Note No., 67, 1956.
87. Stephan, K., Lin, S., Durst, M., Huang, F., and Seher, D., "An Investigation of Energy Separation in a Vortex Tube", *Int. J. Heat Mass Transfer*, Vol. 26, 1983, pp. 341-348.
88. Machine Design, "Laboratory Curiosity Tries Out for the Cooling Job", Vol. 33, pp. 14.
89. Chanaud, R.C., "Experiments Concerning the Vortex Whistle", *J. Acoustic Soc. Am.*, Vol. 35, 1950, pp. 953-960.
90. Vonnegut, B., "A Vortex Whistle", *J. Acoustic Soc. Am.*, Vol. 26, 1954, pp. 18-20.

91. Chanaud, R.C., "Observations of Oscillatory Motion in Certain Swirling Flows", J. Fluid Mech., Vol. 21, Part 1, 1965, pp. 111-127.
92. Brombach, H., "Vortex Devices in Hydraulic Engineering", Proc. Cranfield Fluidics Conference, 5th, Uppsala, 1972, pp. B1-1 to B1-12.
93. Brombach, H., "Vortex Flow Controllers in Sanitary Engineering", Trans. ASME, J. Dyn. Syst. Meas. Control. Vol. 106, 1984, pp. 129-133.
94. Brombach, H. and Neumayer, H., "Development of a Very Large Radial Vortex Valve", J. Fluid Control. Fluid Q., Vol. 9, 1977, pp. 59-74.
95. Fitt, P.W., "A Vortex Valve and Ejector Combination for Improved Turn Down Ratios", Proc. Cranfield Fluid. Conference, 6th, Cambridge, 1974, pp. F1-1 to F1-8.
96. Lawley, T.J. and Price, D.C., "Design of Vortex Fluid Amplifiers with Asymmetrical Flow Fields", Trans ASME, J. Dyn. Syst. Meas. Control. Vol. 94, pp. 82-84.
97. Owen, I. and Syred, N., "Upgrading Vortex Amplifier Performance by Matched Ejectors", J. Fluid Control, Fluidics Q., Vol. 14, 1982, pp. 29-37.
98. Wormley, D.N., "A Review of Vortex Diode and Triode Static and Dynamic Design Techniques", J. Fluid Control, Fluidics Q., Vol. 8, 1976, pp. 85-112.
99. Taplin, L.B. and McFall, R.H., "Vortex Amplifiers and Circuits", Bendix Technical Journal, Vol. 1, No. 4, Winter 1969.
100. Taplin, L.B., "Small Signal Analysis of Vortex Amplifiers", AGRAD Lecture Series on Fluid Control Components and Systems, September 1966.
101. Brombach, H., "Flood Protection by Vortex Valves", Trans. ASME, J. Dyn. Syst. Meas. Control, Vol. 103, 1981, pp. 338-341.

102. Lefebvre, A.H., "Gas Turbine Combustion", Hemisphere Publishing Company, Washington, 1983.
103. Beer, J.M. and Chigier, N.A., "Combustion Aerodynamics", Halsted Press Division, John Wiley and Sons Inc., New York, 1972.
104. Dombrowski, N., "Biochemical and Biological Engineering Science", Vol. 2, Ch. 16, Academic Press, London, 1986.
105. Moffat, R.J., "Describing the Uncertainties in Experimental Results", Experimental Thermal and Fluid Science, 1: pp. 3-17, 1988.
106. Doebelin, E.O., "Measurement System", McGraw-Hill Inc., New York, 1975.
107. Vatistas, G.H., "Theoretical and Experimental Studies on Confined Vortex Flows", Ph.D. Thesis, Concordia University, Montréal, Canada, September 1984.
108. Bach, G.G., "Lecture Notes on Numerical Analysis", Mechanical Engineering Department, McGill University, Montréal, Canada, September 1982.
109. Tager, S.A., "Calculating the Aerodynamic Resistance of Cyclone Combustion Chamber", Thermal Engineering, Vol. 18, No. 7, 1971, pp. 88-91.
110. Troyankin, Y.U. and Baluev, E.D., "The Aerodynamic Resistance and Efficiency of Cyclone Chamber", Thermal Engineering, Vol. 16, 1969, pp. 29.
111. Lewellen, W.S., "A Review of Confined Vortex Flows", NASA Contractor Report (NASA CR-1772), July, 1971.
112. Shakespeare, W.J. and Levy, E.K., "Pressure Drop in a Confined Vortex with High Flow Rate", Paper Presented at the Winter Annual Meeting of ASME, Chicago, Illinois, November, 1980.

113. Carmichael, R.D. and Smith, E.R., "Mathematical Tables and Formulas", Dover Publications, Inc., New York
114. Escudier, M.P., Bornstein, J. and Maxworthy, T., "The Dynamics of Confined Vortices", Proceedings of the Royal Society of London, Vol. A382, 1982, pp. 335-360.
115. Garg, A.K. and Leibovich, S., "Spectral Characteristics of Vortex Breakdown Flowfields", Physics of Fluids, Vol. 22, 1979, pp. 2053-2064.
116. Sedov, L.I., "Similarity and Dimensional Methods in Mechanics", Translated into English by Kisin, V.I., MIR Publishers Moscow, 1982.
117. Faler, J.H. and Leibovich, S., "Disrupted States of Vortex Flow and Vortex Breakdown", Physics of Fluids, Vol. 20, 1977, pp. 1385-1400.
118. Geogantas, A.I., Krepec, T., and Kwok, C.K., "Flow Pattern of Solid Particles in a Double Vortex Chamber", Trans. CSME, Vol. 11, No. 1, 1987, pp. 1-8.
119. Roschke, E.J., "Experimental Investigation of a Confined Jet-Driven Water Vortex", JPL Rep. pp. 32-982, NASA CR-78550.
120. Kendall, J.M. Jr., "Experimental Study of a Compressible Viscous Vortex", JPL Technical Reprt, No. 32-290, June 1962.
121. Prichard, W.G., "Solitary Waves in Rotating Fluids", J. of Fluid Mech., Vol. 24, Part 1, 1970, pp. 61.
122. Robertson, J.M., "Hydrodynamics in Theory and Application", Prentice-Hall Inc., Englewood Cliffs, N.J., 1965.
123. Golden, J.H., "The Life Cycle of Florida Keys' Waterspouts", Journal of Applied Meteorology, Vol. 13, Sept. 1974, pp. 676-689.
124. Massey, B.S., "Mechanics of Fluids", Van Nostrand Reinhold Company, 4th edition, 1979.

APPENDIX I

FORTRAN SOURCE CODE FOR THE DEDUCTION OF THE EXPERIMENTAL DATA

```

PROGRAM EXPT
REAL R(11),THETHA(11),ALPHAE(11),COEFF(11),COEFF2(11),
+   P1P2E(11),P1E(11),PWALL(10),PT(11),PS(11),VTOTAL(11),
+   VR(11),VZ(11),VTAN(11),KAMA(11),CP(11),A(10),B(11),C(10),
+   ERROR(11),POSIT,AR,A1(8),A2(8),A3(8),B1(8),B2(8),B3(8),C1(8),
+   C2(8),C3(8),D1(8),D2(8),D3(8),P4P5E(11),PIANCO(8),PIAN(8),
+   MASS,ANGLE,OLDERR(11),TOL,SCFM
INTEGER NL,NR,I,J,NI,NIMAX
C*****
C                                     L E G E N D                                     *
C                                                                                       *
C   R(I) = NONDIMENSIONAL RADIUS R                                                     *
C   THETHA(I) = MEASURED PITCH ANGLE (EXPERIMENTAL)                                   *
C   ALPHAE(I) = MEASURED YAW ANGLE (EXPERIMENTAL)                                     *
C   COEFF1(I) = VELOCITY PRESSURE COEFFICIENT                                           *
C   COEFF2(I) = TOTAL PRESSURE COEFFICIENT                                              *
C   PAP2E(I) = P1-P2 EXPERIMENTAL VALUE                                                *
C   P1E(I) = P1 EXPERIMENTAL VALUE                                                      *
C   PWALL(I) = MEASURED STATIC PRESSURE AT THE WALL                                  *
C   PT(I) = CALCULATED TOTAL PRESSURE                                                    *
C   PS(I) = CALCULATED STATIC PRESSURE                                                  *
C   VTOTAL(I) = TOTAL VELOCITY                                                         *
C   VR(I) = RADIAL VELOCITY                                                            *
C   VTAN(I) = TANGENTIAL VELOCITY                                                       *
C   KAMA(I) = SWIRLING STRENGTH (R*VTAN)                                              *
C   CP(I) = PRESSURE COEFFICIENT                                                        *
C   A(I) = COEFF. OF THE CUBIC TERM IN THE CUBIC SPLINE                              *
C   POLYMONIAL                                                                           *

```

```

C      B(I) = COEFF. OF THE SQUARE TERM IN THE CUBIC SPLINE      *
C      POLYMONIAL                                                  *
C      C(I) = COEFF. OF THE OREER 1 TERM IN THE CUBIC SPLINE      *
C      POLYMONIAL                                                  *
C      D(I) = THE CONSTANT TERM IN THE CUBIC SPLINE              *
C      POLYMONIAL                                                  *
C      ERROR(I) = ERROR CONTRIBUTE TO P4-P5 ( IN INCHES OF H2O)  *
C      OLDERR(I) = ERROR CALCULATED FROM THE PREVIOUS            *
C      ITERATION                                                  *
C      POSIT = NON DIMENSIONAL AXIAL POSITON (X/L)                *
C      AR = ASPECT RATIO (L/D)                                     *
C      CR = CONTRACTION RATIO                                     *
C      P4P5E(I) = P4-P5 EXPERIMENTAL VALUE                       *
C      PLANCO(I) = PITCH ANGLE COEFF. (CALIBRATED VALUE)         *
C      PLAN(I) = PITCH ANGLE (CALIBRATION VALUE)                 *
C      MASS = MASS FLOW RATE                                      *
C      NI = NUMBER OF ITERATION                                   *
C      NIMAX = MAXIMUM NUMBER OF ITERATION ALLOWED               *
C      TOL = PRESET TOLERANCE FOR THE NUMERICAL ITERATION        *
C      SCFM = THE EXPERIMENTAL FLOW RATE (IN SCFM)               *
C      NL = NUMBER OF AXIAL STATIONS                             *
C      NR = NO. OF POINTS TAKEN IN 1 AXIAL STATION (MAX 11)      *
C      ANGLE = SWIRLING ANGLE                                     *
C                                                                    *
C*****
      NIMAX=10
      READ 1, ANGLE,CR,AR,NL,SCFM
1      FORMAT(F4.1,F3.1,F5.2,I2,F4.1)
C*****
C      INPUT THE VALUE OF THE COEFF.'S FOR THE CUBIC SPLINE      *
C      POLYNOMIAL, WHERE                                          *
C      Y1 = PITCH ANGLE                                           X1 = (P4-P5)/(P1-P2)      *
C      Y2 = (PT-PS)/(P1-P2)                                       X2 = PITCH ANGLE      *
C      Y3 = (P1-PT)/(P1-P2)                                       X3 = PITCH ANGLE      *
C*****

```

```

      DO 55 I = 1, 8
          READ 56, A1(I),B1(I),C1(I),D1(I)
          READ 56, A2(I),B2(I),C2(I),D2(I)
56      READ 56 (4(E11.4),F5.2,F5.1)
55      CONTINUE
C*****
C      INPUT THE LOCAL VALUE AT EACH AXIAL STATION      *
C*****
      DO 11, J = 1, NL
          READ 21, NR,POSIT,PWALL(I)
21      FORMAT(I2,F6.4,F7.2)
          DO 111 I = 1, NR
              READ 22, R(I),ALPHA E(I),P1P2E(I),P1E(I),P4P5E(I)
22      FORMAT(F6.4,F4.1,F4.2,F5.2,F5.2)
111      CONTINUE
C*****
C      START THE ITERATION PROCESS      *
C*****
      NI = 0
C*****
C      FIND OUT THE PITCH ANGLE      *
C*****
99      NI=NI+1
          CALL CALIB (NR,P1P2E,P4P5E,ERROR,A1,A2,A3,B1,B2,B3,C1,C2,
                   C3,D1,D2,D3,PIANCO,PIAN,THETHAE,COEFF1,
                   COEFF2)
C*****
C      CALCULATE THE PRESSURES AND VELOCITIES      *
C*****
          CALL VEL (NR,R,ALPHA E,THETHAE,COEFF1,COEFF2,P1P2E,P1E,
                   PWALL(J),PT,PS,VTOTAL,VR,VZ,VTAN,KAMA,CP)
C*****
C      CREATE THE CUBIC SPLINE POLYNOMIAL FOR THE LOCAL      *
C      AXIAL STATION, WHERE Y = CP , X = R      *
C*****
          CALL SPLINE (NR,R,CP,A,B,C)

```

```

C*****
C   CALCULATE THE ERROR CONTRIBUTE BY TJE CENTRIFUGAL   *
C   FLOWFILED                                           *
C*****
      CALL CORREC (NR,R,A,B,C,CP,ERROR,OLDERR,TOL)
      IF ( NI.EQ. 1 ) GO TO 100
      IF ( NI.GT. NIMAX ) GO TO 100
      IF ( ABS(TOL).GT. 1E-4 ) GO TO 99
C*****
C   CALCULATE THE MASS FLOW AT THAT STATION             *
C*****
100      CALL FLOW (NR,R,VZ,MASS)
C*****
C   PRINT OUT THE REQUIRED RESULTS                       *
C*****
      PRINT 23, AR, POSIT, ANGLE, CR, NI, TOL, SCFM
      PRINT 24
      DO 112 I = 1, NR
          PRINT 25, R(I), PT(I), PS(I), VTOTAL(I), VR(I), VZ(I), VTAN(I),
+              KAMA(I), CP(I)
112      CONTINUE
      PRINT 26
      DO 113 I = 1, NR-1
          PRINT 27, R(I),R(I+1), A(I), B(I), C(I), CP(I)
113      CONTINUE
      PRINT 333, MASS
      PRINT 28
      DO 114 I = 1, NR
          PRINT 29, R(I), ERROR(I)
114      CONTINUE

      IF ( NI.EQ. 1 ) GO TO 99

11      CONITNUE

      STOP

```

```

END
SUBROUTINE CALIB (NR,P1P2E,P4P5E,ERROR,A1,A2,A3,B1,B2,B3,
                  C1,C2,C3,D1,D2,D3,PIANCO,PIAN,THETAЕ,
                  COEFF1,COEFF2)
REAL P1P2E(11),P4P5E(11),ERROR(11),A1(8),A2(8),A3(8),B1(8),B2(8),
      B3(8),C1(8),C2(8),C3(8),D1(8),D2(8),D3(8),PIANCO(8),PIAN(8),
      THETAЕ(11),COEFF1(11),COEFF2(11)
C*****
C  CALCULATE PITCH ANGLE COEFF. INCLUDING THE ERROR      *
C*****
      DO 67 I = 1, NR
          PITCOE(I) = (P4P5E(I) + ERROR(I))/P1P2E(I)
67      CONTINUE
C*****
C  CHECK THE RANGE OF (P4-P5)/(P1-P2)                      *
C*****
      DO 68 I = 1, NR
          IF ( PITCOE(I) .GT. 1.29 .OR. PITCOE(I) .LT. -1.5 ) THEN
              PITCOE(I) = P4P5E(I)/P1P2E(I)
          END IF
68      CONTINUE
C*****
C  CALCULATE THE PITCH ANGLE FROM THE CALIBRATION          *
C  CUBIC SPLINE POLYNOMIAL                                  *
C*****
          CALL PITCH (NR, PITCOE, PIANCO, A1, B1, C2, D1, THETAЕ)
C*****
C  CALCULATE (PT-PS)/(P1-P2) AND (P1-PT)/(PT-PS)          *
C*****
          CALL VELPR (NR, THETAЕ, PIAN, A2, B2, C2, D2, A3, B3, C3, D3,
+                  COEFF1, COEFF2)

      RETURN
END

```

```

SUBROUTINE PITCH (NR,PITCOE,PIANCO,A1,B1,C1,D1,THETA)
REAL PITCOE(11),PIANCO(8),A1(8),B1(8),C1(8),D1(8),THETA(11)
C*****
C   FIND THE RABGE OF (P4-P5)/(P1-P2)
C*****

DO 69 I = 1, NR
IF ( PITCOE(I) .GE. -0.15 ) THEN
  IF ( PITCOE(I) .GE. 0.64 ) THEN
    IF ( PITCOE(I) .GE. 0.98 ) THEN
      K = 8
    ELSE
      K = 7
    ELSE
      IF ( PITCOE(I) .GE. 0.21 ) THEN
        K = 6
      ELSE
        K = 5
      END IF
    END IF
  ELSE
    IF ( PITCOE(I) .GE. -0.89 ) THEN
      IF ( PITCOE(I) .GE. -0.56 ) THEN
        K = 4
      ELSE
        K = 3
      END IF
    ELSE
      IF ( PITCOE(I) .GE. -1.2 ) THEN
        K = 2
      ELSE
        K = 1
      END IF
    END IF
  END IF
END IF
END IF
C*****

```

```

C      CALCULATE THE VALUE OF PITCH ANGLE      *
C*****
      DIFF = PITCOE(I) - PLANCO(K)
      THETAHAE(I) = ((A1(K)*DIFF+B1(K))*DIFF+C1(K))*DIFF+D1(K)
69    CONTINUE
      RETURN
      END

      SUBROUTINE VELPR (NR,THETAHAE,PLAN,A2,B2,C2,D2,A3,B3,C3,D3,
+                      COEFF1,COEFF2)
      REAL THETAHAE(11),PLAN(8),A2(8),B2(8),C2(8),D2(8),A3(8),B3(8),C3(8),
          D3(8),COEFF1(11),COEFF2(11)
C*****
C      FIND THE RABGE OF PITCH ANGLE      *
C*****
      DO 77 I = 1, NR
      IF ( THETAHAE(I) .GE. 0.0) THEN
        IF ( THETAHAE(I) .GE. 20.0 ) THEN
          IF ( THETAHAE(I) .GE. 30.0 ) THEN
            K = 8
          ELSE
            K = 7
          ELSE
            IF ( THETAHAE(I) .GE. 10.0 ) THEN
              K = 6
            ELSE
              K = 5
            END IF
          END IF
        ELSE
          IF ( THETAHAE(I) .GE. -20.0) THEN
            IF ( THETAHAE(I) .GE. -10.0 ) THEN
              K = 4
            ELSE
              K = 3
            END IF
          ELSE
            K = 3
          END IF
        END IF
      END IF
      K = 3
    END IF
  
```



```

ELSE
  IF ( THETA E(I) .GE. -30.0 ) THEN
    K = 2
  ELSE
    K = 1
  END IF
END IF
END IF

C*****
C  CALCULATE THE VALUE OF THE 2 COEFF.'S
C*****
  DIFF = THETA E(I) - PLAN(K)
  COEFF1(I) = ((A2(K)*DIFF+B2(K))*DIFF+C2(K))*DIFF+D2(K)
  COEFF2(I) = ((A3(K)*DIFF+B3(K))*DIFF+C3(K))*DIFF+D3(K)
77  CONTINUE
  RETURN
END

SUBROUTINE VEL (NR,R,ALPHA E,THETA E,COEFF1,COEFF2,P1P2E,
+              P1E,PWALL,PT,PS,VTOTAL,VR,VZ,VTAN,
+              KAMA,CP)
  REAL ALPHA E(11),THETA E(11),COEFF1(11),COEFF2(11),P1P2E(11),
+      P1E(11),PWALL(11),PT(11),PS(11),VTOTAL(11),VR(11),VZ(11),
+      VTAN(11),KAMA(11),CP(11)
C
  RHO = 1.2925
  PI = ACOS(-1.0)
C
  DO 44 I = 1, NR
C*****
C  CONVERT DEGREES INTO RADIANS
C*****
    ALPHA E(I) = ALPHA E(I)*PI/180.0
    THETA E(I) = THETA E(I)*PI/180.0
C*****
C  CONVERT PRESSURE INTO SI UNITS

```

```

C*****
      P1P2(I) = P1P2E(I)*249.174
      P1(I) = P1E(I) *249.174
      PTPS(I) = COEFF1(I)*P1P2(I)
      P1PT(I) = COEFF2(I)*PTPS
      PT(I) = P1(I) - P1PT
      PS(I) = PT(I) - PTPS
      VTOTAL(I) = SQRT(2*PTPS/RHO)
      VR(I) = VTOTAL(I)*SIN(THETA(I))
      VZ(I) = VTOTAL(I)*COS(THETA(I))*COS(ALPHA(I))
      VTAN(I) = VTOTAL(I)*COS(THETA(I))*SIN(ALPHA(I))
      KAMA(I) = 0.014407443*(PWALL-PS)
44  CONTINUE
      RETURN
      END

      SUBROUTINE FLOW (NR,R,VZ,MASS)
      REAL R(11),VZ(11),MASS
C
      MASS = 2*VZ(1)*R(1)*R(1)
      DO 55 I = 1, NR
          MASS = MASS + (VZ(I)+VZ(I+1))*(R(I+1)*R(I+1)-R(I)*R(I))
55  CONTINUE
      MASS = MASS + VZ(NR)*(1.0-R(NR)*R(NR))
      MASS = MASS*0.009905656
      RETURN
      END

      SUBROUTINE SPLINE (NR,R,Y,A,B,C)
      REAL R(11),Y(11),H(10),S(9,9),T(9),A(10),B(11),C(10)
C
      DO 33 I = 1, NR-1
          H(I) = R(I+1)-R(I)
33  CONTINUE
C*****
C  ASSEMBLE THE MATRIX [S][B]=[T]

```

```

C*****
      CALL ASEEM (Y,H,S,T,NR)
C*****
C      SOLVE A, B, C
C*****
      CALL SOLVE (S,T,Y,H,A,B,C,NR)
      RETURN
      END

      SUBROUTINE ASSEM (Y,H,S,T,NR)
      REAL Y(11),H(10),S(9,9),T(9)
C*****
C      IMPOSE THE BOUNDARY CONDITIONS
C*****
      S(1,1) = 3*H(1)/4.0 + 2*H(2)
      T(1) = 3*(Y(3)-Y(2))/H(2) - 9*(Y(2)-Y(1))/2/H(1)
C*****
C      INPUT THE ELEMENTS OF THE MATRIX IN TERMS OF H(I)
C*****
      DO 100 I = 2, NR-2
        S(I-1,I) = H(I)
        S(I,I-1) = H(I)
        S(I,I) = 2*(H(I)+H(I+1))
        T(I) = 3*((Y(I+2)-Y(I+1))/H(I+1) - (Y(I+1)-Y(I))/H(I))
100    CONTINUE
      RETURN
      END

      SUBROUTINE SOLVE (S,T,Y,H,A,B,C,NR)
      REAL S(9,9),T(9),A(10),B(11),C(10),P(9),Q(9),R(9),H(10),Y(11)
C*****
C      SOLVE THE TRIDIAGONAL MATRIX
C*****
      P(1) = S(1,1)
      Q(1) = S(1,2)
      R(1) = T(1)

```

```

DO 200 K = 2, NR -2
  P(K) = S(K,K-1)*Q(K-1) - S(K,K)*P(K-1)
  R(K) = S(K,K-1)*R(K-1) - T(K)*P(K-1)
  IF ( K .NE. NR-2 ) THEN
    Q(K) = -S(K,K-1)*P(K-1)
  ELSE
    Q(K) = 0.0
  END IF
200  CONTINUE
  B(NR-1) = R(NR-2)/P(NR-2)
  DO 300 K = NR-3, 1, -1
    B(K-1) = (R(K)-Q(K)*B(K+1))/P(K)
300  CONTINUE
  B(1) = 3*(Y(2)-Y(1))/2/H(1)/H(1) - B(2)/2
  B(NR) = 0.0
  DO 400 I = 1, NR-1
    A(I) = (B(I+1)-B(I))/3/H(I)
    C(I) = (Y(I+1)-Y(I))/H(I) - H(I)*(B(I+1)+2*B(I))/3
400  CONTINUE
  RETURN
END

SUBROUTINE CORREC (NR,R,A,B,C,D,ERROR,OLDERR,TOL)
  REAL R(11),A(11),B(11),C(11),D(11),ERROR(11),OLDERR(11),TOL
C*****
C  CONVERSION FACTOR FOR THE ERROR TERM (IN INCHES)  *
C*****
  COEFF = 0.014407443*249.174
  DO 204 I =1, NR
    OLDERR(I) = ERROR(I)
204  CONTINUE
  DO 202 I = 1, NR
C*****
C  CALCULATE CP VALUES AT ONE END  *
C*****
    IF ( I.EQ. 1) THEN

```

```

      F1 = D(I)
      F2 = ((A(I)*0.02+B(I))*0.02+C(I))*0.02+D(I)
      GO TO 203
    END IF

C*****
C    CALCULATE THE CP VALUES AT THE SECOND PT WITH      *
C    R=0.0455 AS THE FIRST POINT                          *
C*****

      IF ( I.EQ. 2 .AND. R(1) .LT. 0.05 ) THEN
        F1 = ((A(I-1)*0.0254+B(I-1))*0.0254+C(I-1))*0.0254+D(I-1)
        F2 = ((A(I)*0.02+B(I))*0.02+C(I))*0.02+D(I)
        GO TO 203
      END IF

C*****
C    CALCULATE CP VALUES AT THE OTHER END                *
C*****

      IF ( I.EQ. NR ) THEN
        F1 = ((A(I-1)*0.0709+B(I-1))*0.0709+C(I-1))*0.0709+D(I-1)
        F2 = ((A(I-1)*0.0909+B(I-1))*0.0909+C(I-1))*0.0909+D(I-1)
        GO TO 203
      END IF

C*****
C    CALCULATE CP VALUES AT THE OTHER POINTS            *
C*****

      F1 = ((A(I-1)*0.0709+B(I-1))*0.0709+C(I-1))*0.0709+D(I-1)
      F2 = ((A(I)*0.02+B(I))*0.02+C(I))*0.02+D(I)
203    ERROR(I) = (F1-F2)/COEFF
202    CONTINUE
      TOL = 0.0
      DO 205 I = 1, NR
        TOL = TOL + ERROR(I)-OLDERR(I)
205    CONTINUE
      RETURN
    END

```

APPENDIX II

CALIBRATION DATA FOR THE FIVE HOLE PITOT PROBE

The calibration data for the five hole pitot probe is provided by the manufacturer in terms of graphical means. From Fig. (A.II.1) to (A.II.3), the three graphs can be considered as all the calibration data required for the probe.

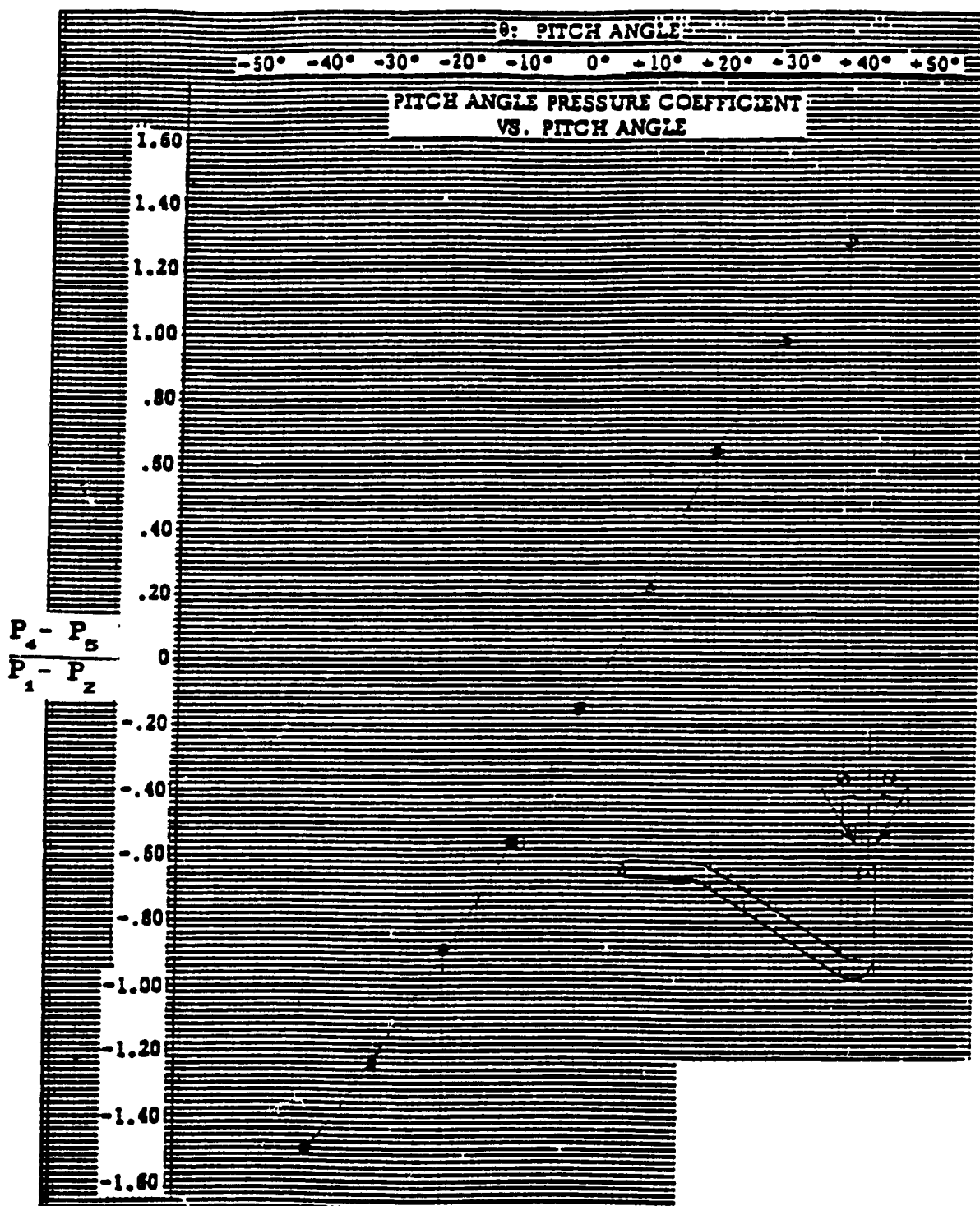


Figure A.II.1 The calibration chart of $\frac{P_4 - P_5}{P_1 - P_2}$ (Pressure Coefficient) vs.
Pitch Angle

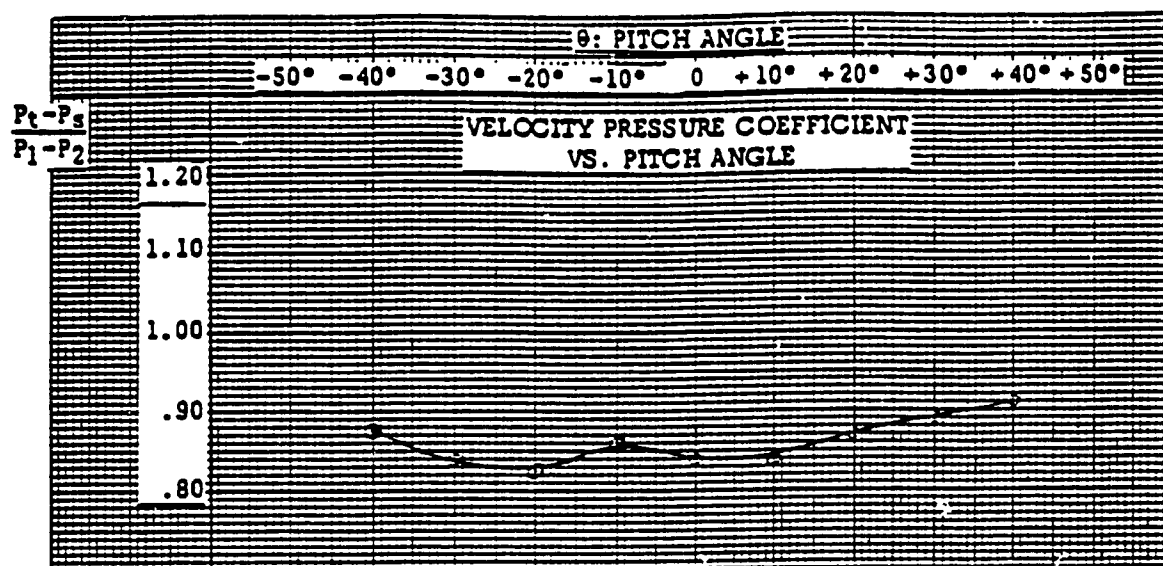


Figure A.II.2 $\frac{P_t - P_s}{P_1 - P_2}$ (Velocity Pressure Coefficient) vs. Pitch Angle

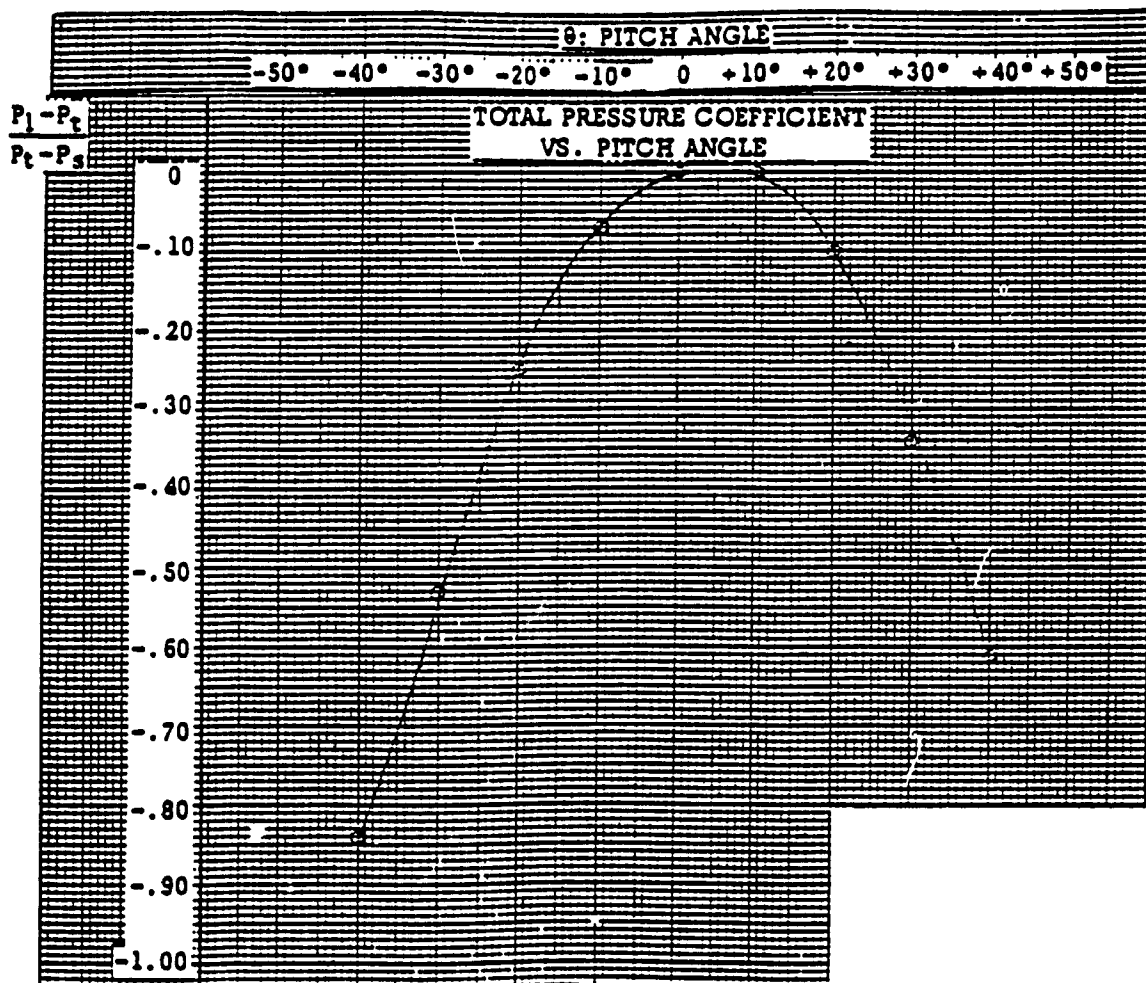


Figure A.11.3 $\frac{P_1 - P_t}{P_t - P_s}$ (Total Pressure Coefficient) vs
Pitch Angle